# Penning trap mass measurements to test three-body forces in atomic nuclei

by

Aaron T. Gallant

B.Sc., Saint Mary's University, 2008

A THESIS SUBMITTED IN PARTIAL FULFILLMENT
OF THE REQUIREMENTS FOR THE DEGREE OF

**Doctor of Philosophy**

in

THE FACULTY OF GRADUATE AND POSTDOCTORAL STUDIES
(Physics)

The University of British Columbia
(Vancouver)

November 2015

# Abstract

Recent theoretical studies have shown that three-nucleon forces are important for understanding neutron-rich nuclei, and for the formation of nuclear shell structure. In particular, theory can not reproduce the $N = 28$ magic number in $^{48}$Ca using two-body interactions. This magic number is only reproduced with the inclusion of three-nucleon forces. Further along the calcium isotopic chain, the three-nucleon interaction predicts new magic numbers at $N = 32$ and 34, while calculations with phenomenological interactions predict a magic number at $N = 32$, but disagree on the magicity of $N = 34$. An other theoretical tool that has been under significant pressure since the advent of precision mass measurements is the isobaric multiplet mass equation, in which the binding energies of states in an isobaric multiplet should vary quadratically with the $z$-projection of the isospin. This is a consequence of the isospin dependent component of the nuclear Hamiltonian and Coulomb interactions. We test the predictions of phenomenological and three-nucleon interactions through mass measurements of $^{20,21}$Mg, $^{51,52}$Ca, and $^{51}$K with the TITAN Penning trap mass spectrometer. The measured mass excesses were ME($^{20}$Mg) = 17477.7(18) keV, ME($^{21}$Mg) = 10903.85(74) keV, ME($^{51}$Ca) = 36339(23) keV, ME($^{52}$Ca) = 34245(61) keV, and ME($^{51}$K) = 22516(13) keV. With the calcium and potassium mass measurements, we show that the calculations with three-nucleon forces are able to correctly predict the two-neutron separation energies. In the $A = 20$ and 21 isobaric multiplets, neither the phenomenological nor the three-nucleon based interactions are able to reproduce the measured behaviour.

# Preface

The experimental work presented here was performed at the Tri-University Meson Facility (TRIUMF), Vancouver, BC, using TRIUMF's Ion Trap for Atomic and Nuclear science (TITAN) Penning trap mass spectrometer.

The main part of this thesis, the mass measurements of $^{50,51}$Ca, $^{51}$K and $^{20,21}$Mg, are published in the works

- A. T. Gallant, M. Brodeur, C. Andreoiu, *et al.*. *Breakdown of the Isobaric Multiplet Mass Equation for the A = 20 and 21 Multiplets*. Phys. Rev. Lett., 113, 082501 (2014).
- A. T. Gallant, J. C. Bale, T. Brunner *et al.*. *New precision mass measurements of neutron-rich calcium and potassium isotopes and three-nucleon forces*, Phys. Rev. Lett., 109, 032506 (2012).

For both publications I lead and organized the experimental team during the experiment with the help of A. A. Kwiatkowski and A. Chaudhuri. The data collection was performed with the help of C. Andreoiu, A. Bader, J. C. Bale, M. Brodeur, T. Brunner, A. Chaudhuri, U. Chowdhury, P. Delheij, E. Mané, S. Ettenauer, A. Grossheim, R. Klawitter, A. A. Kwiatkowski, K. G. Leach, A. Lennarz, T. D. Macdonald, D. Robertson, H. Savajols, B. E. Schultz, M. C. Simon, V. V. Simon, and M. R. Pearson. For both experiments the use of the TRIUMF Resonant Laser Ionization Source (TRILIS), and the later addition of the Ion Guide Laser Ion Source (IG-LIS) were crucial in producing the Ca and Mg beams. TRILIS and IG-LIS were run by J. Lassen, H. Heggen, S. Raeder, and A. Teigelhöfer. I was responsible for analyzing the data and preparing the manuscripts. The theoretical calculations presented in these papers were done by B. A. Brown and A. Magilligan, and by J. D. Holt, J. Menéndez, J. Simonis, A. Schwenk.

# Table of Contents

# List of Tables

# List of Figures

# Glossary

AME03 Atomic Mass Evaluation 2003

AME11 Atomic Mass Evaluation 2011

AME12 Atomic Mass Evaluation 2012

$\chi$EFT Chiral Effective Field Theory

CCSD Coupled-Cluster Singles-Doubles

EBIT Electron Beam Ion Trap

FT-ICR Fourier-Transform Ion Cyclotron Resonance

GXPF1A *G*-matrix, experimentally fit interaction

HCI Highly Charged Ions

IG-LIS Ion Guide Laser Ion Source

IMME Isobaric Multiplet Mass Equation

ISAC Isotope Separator Accelerator

ISOL Isotope Separation on-line

KB3G mass-dependent Kuo-Brown interaction

LS Lorentz Steerer

MCP Micro-Channel Plate

MPET Measurement Penning Trap

MBPT Many-Body Perturbation Theory

NN nucleon-nucleon

PI-ICR Phase-Imaging Ion Cyclotron Resonance

PTMS Penning Trap Mass Spectrometry

QCD Quantum Chromodynamics

RILIS Resonance Ionization Laser Ion Source

RFQ Radio-Frequency Quadrupole

SCI Singly Charged Ions

TOF-ICR Time-of-Flight Ion Cyclotron Resonance

TITAN TRIUMF's Ion Trap for Atomic and Nuclear science

TRILIS TRIUMF's Resonance Ionization Laser Ion Source

USD Universial *sd*

# Chapter 1

# Introduction

Atomic masses are fundamental quantites that provides important insight into the inner workings of the nuclear interaction through the binding energy, or the difference between the sum of the mass of the constituents and the mass of the whole. Not only is the atomic mass crucial in understanding nuclear physics, it is also required for studying astrophysics, determining the origin of nuclei heavier than iron in the universe, and in weak-interaction studies. Figure 1.1 summarizes our current knowledge of the limits of existence of atomic nuclei. The nuclides in black are stable against decay, having infinite half-lives, while the nuclides in yellow are unstable against decay, decaying by emitting either $\beta$-particles (electrons or positrons), $\alpha$-particles or by spontaneous fission. Currently there are 288 known stable nuclides, and approximately 3000 known unstable nuclides, while there are predicted to be $\approx 7000$ bound nuclei with proton number less than 120 [1]. The path along the stable nuclides in figure 1.1 is known as the "valley of stability". Moving away from stability by adding either protons or neutrons, one eventually reaches the proton or neutron driplines. The driplines are defined to be the point where the separation energy, the energy required to remove a nucleon from the nucleus, changes from positive to negative. As seen in figure 1.1, the predicted two-neutron driplines, for most of the nuclear chart, lie far beyond the current limits of experimental knowledge.

Since the discovery of the nucleus, many seemingly contradictory models have been successfully used to describe nuclear structure. The earliest models considered the nucleus to be a "liquid drop", in which protons and neutrons only interact with their nearest neighbours. As figure 1.2 shows, this can be seen in the nearly constant binding energy per nucleon for the stable nuclides. While this model was able to describe several features of nuclei, such as general binding energies and fission energies of heavy nuclei, it was unable to describe the high binding energies of light nuclei, and the stability of nuclei with specific numbers of protons and neutrons. A slight improvement on this model is the cluster model, in which clusters of

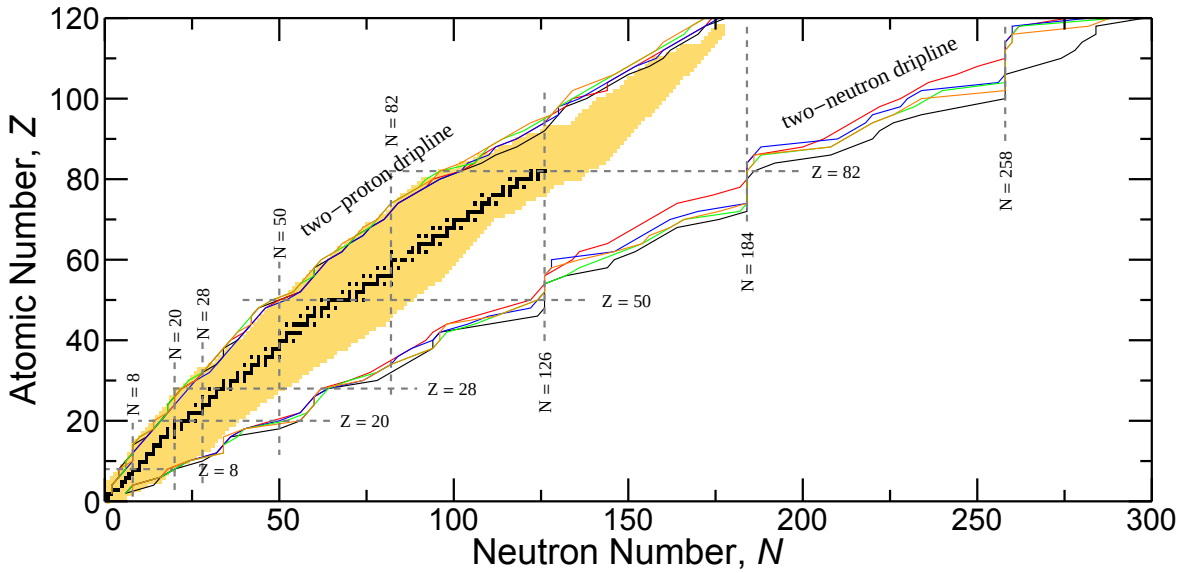


**Figure 1.1:** Sergè chart showing the location of known stable nuclides (black) and unstable nuclides (yellow). Also shown are theoretical calculations [1] giving the predicted location of the two-proton and two-neutron driplines. The dashed lines are the "magic numbers" (section 1.1).

nucleons inside the nucleus would generally bind as $\alpha$-particles; however, again, this cluster model does not describe the entirety of known nuclear properties. Many of these problems were resolved with the introduction of the *nuclear shell model*, in which individual nucleons move in a mean field and is analogous to the shell model in atomic physics.

A pressing question in nuclear physics is how the behaviour of the nuclear interaction changes as one moves away from the stable nuclei. In particular, it is important to investigate, both experimentally and theoretically, how *nuclear structure*, or the properties of individual nuclei, varies towards the driplines. In this thesis precision mass measurements were performed, and the results are compared to shell model calculations.

## 1.1 The shell model

The atomic nucleus is a complex many-body quantum system, and its understanding has been an active field of research for more than a century. Atomic nuclei are composed of two nearly identical constituent nucleons: protons and neutrons. Their relative mass difference is only $\approx 0.14\%$ [2], both are Fermions, and have spins and parities of $J^\pi = 1/2^+$. The largest difference between them is their charge—the proton being positively charged $q = +1e$, and the neutron being neutral, where $e$ is the charge of the electron. The aim of nuclear physics is to understand the interactions between quarks and gluons to form neutrons and protons, and

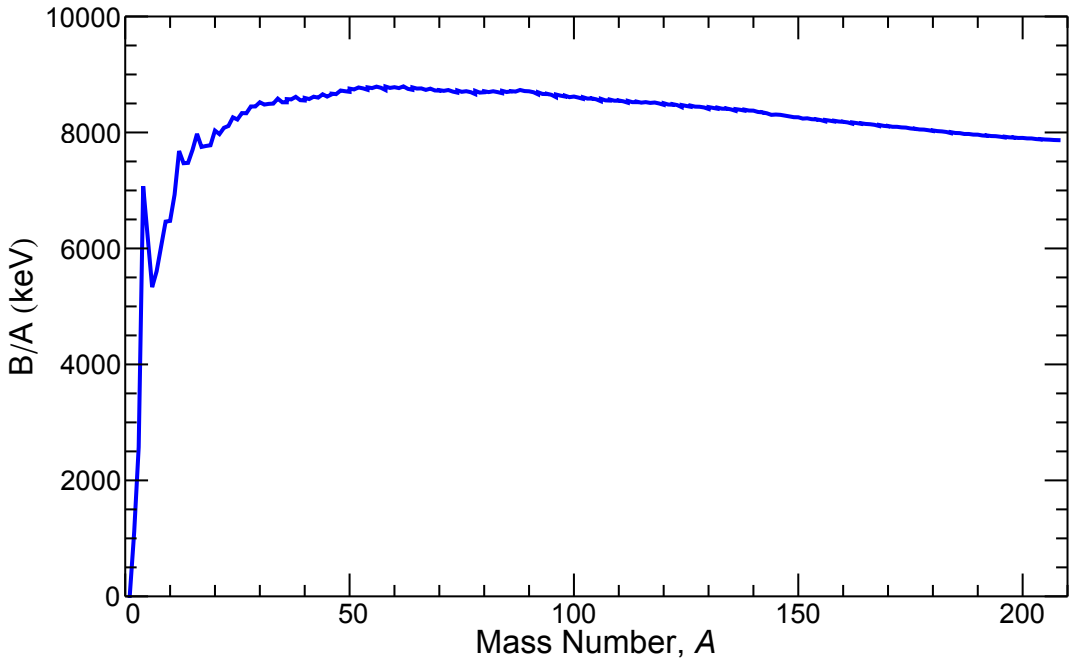


**Figure 1.2:** Nuclear binding energy per nucleon for the stable nuclides.

from there to describe the interaction between ensembles of nucleons, ultimately connecting these to the fundamental interactions in the Standard Model of particle physics. The nuclear problem occupies an interesting space, as, except in the lightest nuclei, there are too many particles to calculate exact results from first principles, but, even for the heaviest nuclei, there are not enough particles for a purely statistical approach [3]. The nuclear shell model is used to describe the region of nuclei that lie between these two extremes, as a mean central potential is formed through the mutual interaction between the nucleons, but only the valence nucleons, the nucleons near the Fermi surface, play an active role in determining nuclear structure and properties: structure such as shape (is the nucleus spherical, prolate or oblate), and properties such as the spins, parities, and half-lives of the ground and excited states.

One early approach to solving the nuclear problem was the independent particle model [4], in which nucleons move in a mean attractive potential well with no interactions with other nucleons. The Hamiltonian is formed by a spin-independent central potential plus a spin-orbit potential and an orbit-orbit term,

$$H(r) = -V_0 + T + \frac{1}{2}m\omega^2 r^2 - V_{\mathrm{SO}}\vec{\ell}\cdot\vec{s} - V_{\mathrm{B}}\vec{\ell}^2, \tag{1.1}$$

where $V_0$ is the central depth of the potential (typically $\approx -51$ MeV), $T$ is the kinetic energy of the nucleon, $V_{\mathrm{SO}}$ is the spin-orbit potential which can depend on $r$ or derivatives of the central

potential, and $V_{\mathrm{B}}$ is the orbit-orbit potential. A harmonic oscillator (HO) basis is often used in nuclear theory, as it greatly simplifies the mathematics involved; however, quite often large sets of basis states are needed to accurately describe nuclear wavefunctions. The spin-orbit potential is similar to the spin-orbit coupling of electrons in the atomic potential, but in nuclei the coupling is much stronger and has an opposite sign to the atomic case. Further, while the spin-orbit potential in atomic systems arise from the magnetic field generated by the movement of the electron, the spin-orbit term in atomic nuclei is a property of the strong force and is not of a magnetic origin.

The energy levels of a three-dimensional harmonic oscillator in spherical coordinates are $E = \hbar\omega(N+3/2) = \hbar\omega(2n+\ell+3/2)$, where $N = 2n+\ell$ is the major quantum number, $n$ is the radial quantum number, and $\ell$ is the angular momentum quantum number. For even-$N$, only even $\ell$-values are allowed, and for odd-$N$, only odd-$\ell$ values are allowed. As a result each major shell alternates the parity of the angular momentum wavefunction. The orbit-orbit term breaks the degeneracy of the harmonic oscillator; however the states can still be grouped by their major oscillator number. The shift in energy is given by $V_B\ell(\ell+1)$. The spin-orbit term further breaks the degeneracy in the energy levels, splitting each state depending on the total angular momentum. The energy splitting is given by the expectation value of $\vec{\ell}\cdot\vec{s}$, which can be found using the total angular momentum

$$j^2 = (\vec{\ell}+\vec{s})^2 = \ell^2 + s^2 + 2\vec{\ell}\cdot\vec{s}. \tag{1.2}$$

This leads to a spin-orbit energy shift of

$$E(\mathrm{SO}) = -\frac{V_{\mathrm{so}}}{2}\left(j(j+1) - \ell(\ell+1) - s(s+1)\right). \tag{1.3}$$

States with higher $j$ are lowered in energy, while states with lower $j$ are raised in energy.

**Figure 1.3:** (Continued on following page) Single particle energies in the shell model. The left column shows the harmonic oscillator levels, the second column shows the effect of the orbit-orbit $V_B\ell(\ell+1)$ term, the third column shows the effect of the spin-orbit $V_{\mathrm{so}}\vec{\ell}\cdot\vec{s}$ term, and the last column shows the energy levels for a Woods-Saxon potential suitable for $^{208}$Pb, calculated with the program wspot [5]. Only bound states are shown. The states are labelled $n\ell_j$, where $n$ is the radial quantum number, $\ell$, the angular momentum quantum number, is labelled $s,p,d,f,g,h,i$ for $\ell = 0,1,2,3,4,5,6$, and $j$ is the total angular momentum $\vec{l}+\vec{s}$. The numbers in brackets denotes the maximum occupation for a given orbit. The magic numbers are also labelled.

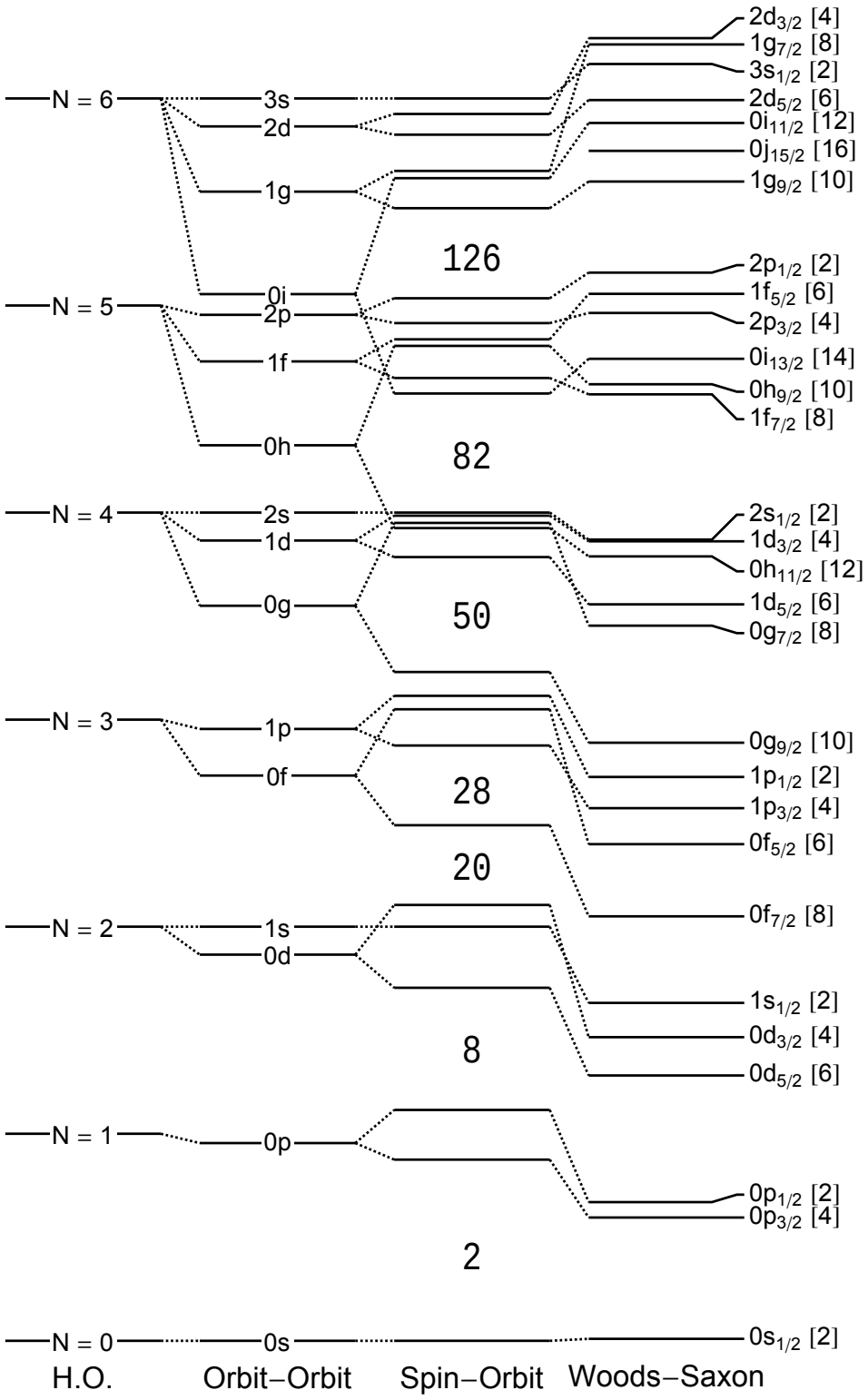


**Figure 1.3:** (Continued from previous page.)

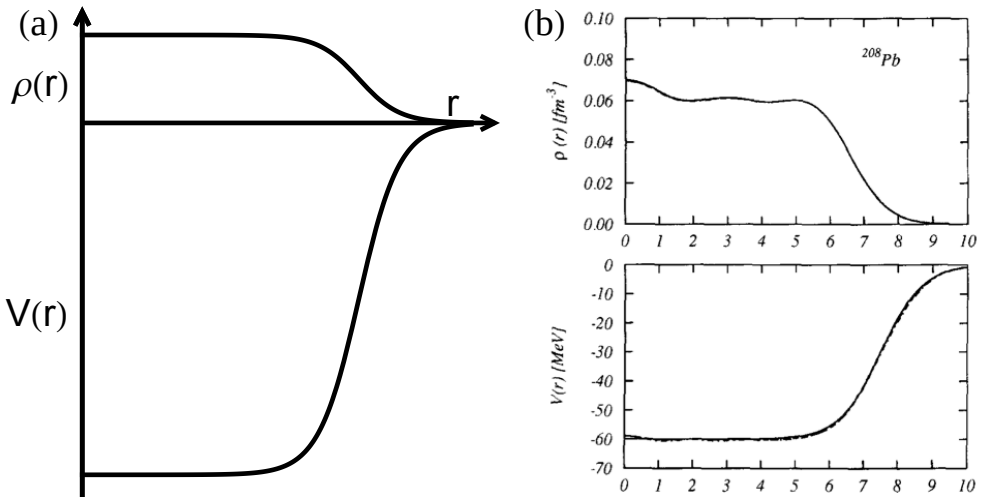


**Figure 1.4:** (a) Schematic plot of the Woods-Saxon potential, and density, for $^{208}$Pb. (b) Top: Experimentally extracted density profile for $^{208}$Pb. Bottom: Central Woods-Saxon potential during the calculation. Figure (b) reproduced with permission from [6].

Instead of a harmonic oscillator potential, there are several other central potentials that can be used. A commonly used potential is the Woods-Saxon potential [7] with the form

$$V(r) = \frac{-V_0}{1 + exp((r-R)/a)} \tag{1.4}$$

where $R$ is the mean radius of the nucleus, and $a$ is the mean skin thickness, typically chosen to be $R = 1.25A^{1/3}$ fm and $a = 0.524$ fm. A Woods-Saxon form is quite natural, as it is a close approximation to the same form that the nuclear density takes. As seen in figure 1.4, this is confirmed by the measurement of the charge density in $^{208}$Pb through the use of elastic electron scattering [6].

The ordering of the states depends on the values chosen for $V_{so}$ and $V_B$, as well as on the form of the central potential, evidenced by the re-arrangement of states between the HO and Woods-Saxon calculations. An interesting side-effect of the spin-orbit force is that states from different major oscillators mix with each other. For example, in figure 1.3 the $N = 4$, $0g_{9/2}$ state becomes part of the group of states made up from the $N = 3$, p and f states. Including these states in large-scale shell model calculations can be important in reproducing experiments [8, 9, 10].

As seen in figure 1.3, the spin-orbit term gives rise to the so-called nuclear "magic numbers" [11, 12]. The nuclear magic numbers are conceptually similar to the atomic closed shell numbers, in which elements having large first ionization potentials are non-reactive. These

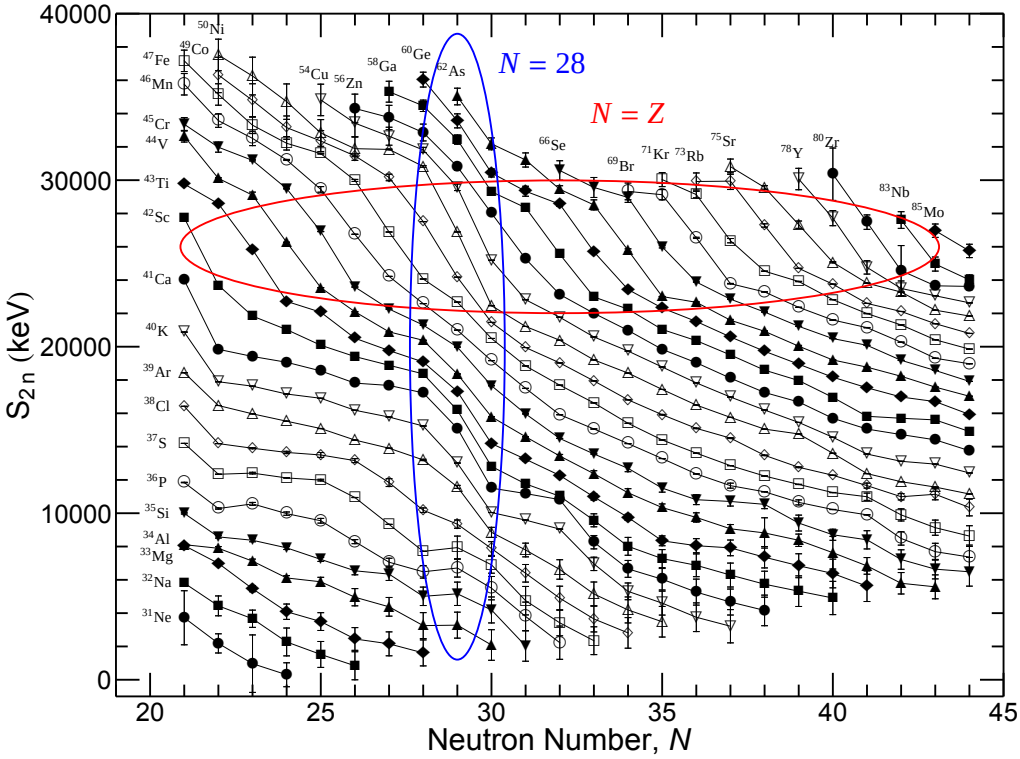


**Figure 1.5:** Two neutron separation energies near $N = 28$. The region in red shows the Wigner energy along $N = Z$, while the blue region shows the magic number at $N = 28$. Data from [14].

elements are called the noble gases. Because of these similarities, this model of the nucleus is called the shell model. Experiments had found that certain nuclei with neutron $N$ or proton $Z$ numbers of $N, Z = 2, 8, 20, 28, 50, 82$ and $N = 126$ were significantly more tightly bound than their neighbours. For example, nuclei with $N = 50$ or 82 exhibit higher natural chemical abundances than could be explained by the existing models [13]. At $Z = 50$, the chemical element tin shows the most number of stable isotopes with a total of 11. Further, there are 6 stable nuclei with $N = 50$ and 7 with $N = 82$. Oxygen-16, a "doubly" magic nucleus with 8 protons and 8 neutrons, requires 15.6 MeV of energy to remove one neutron, while $^{17}$O, with one additional neutron, requires only 4.1 MeV of energy to remove one neutron.

The enhanced binding near the magic numbers can be seen in systematic studies of the binding energy $BE$

$$BE(N,Z) = Zm_Hc^2 + Nm_nc^2 - M(N,Z)c^2 \tag{1.5}$$

where $m_H$ and $m_n$ are the masses of hydrogen and the neutron, respectively, $M(N,Z)$ is the atomic mass of a nuclide, and $c$ is the speed of light. The observed behaviour of the nuclear binding energy changes at the magic numbers, hence differences—or derivatives—of the

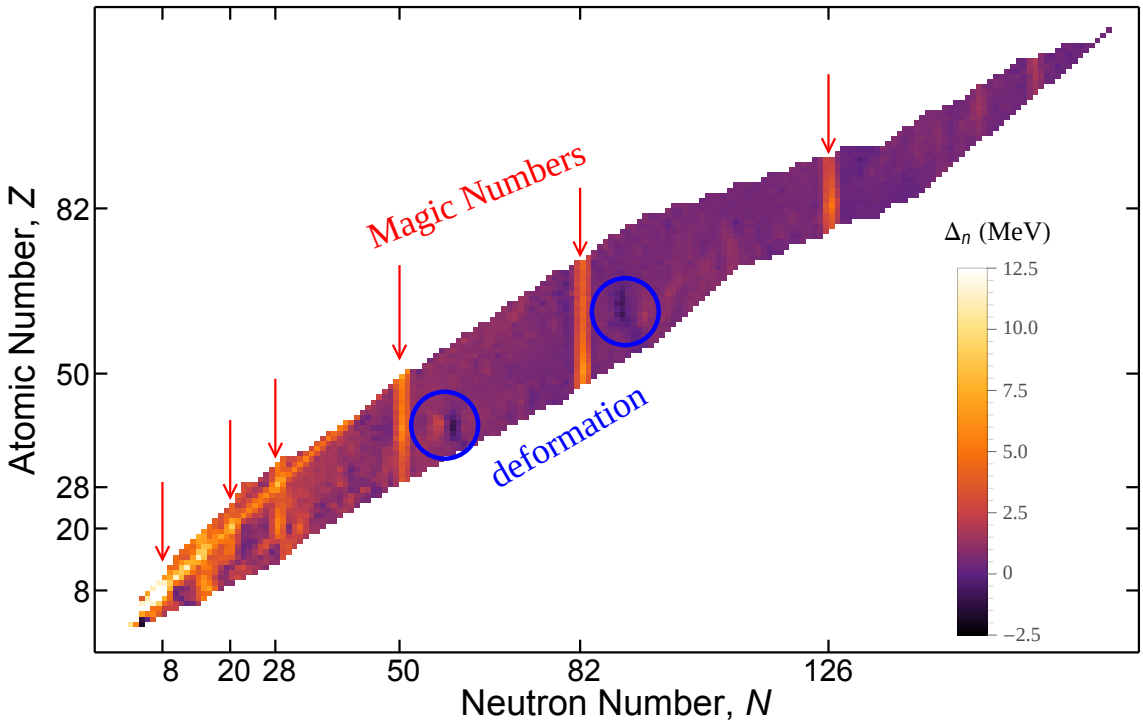


**Figure 1.6:** $\Delta_n$ surface. The neutron magic numbers are clearly seen as bright vertical bands. Areas of deformation can be seen near $(N,Z) = (60,40)$ and $(90,62)$. Data from [14].

binding energy highlights these areas. Two commonly used differences are the two-neutron separation energy $S_{2n}$

$$S_{2n}(N,Z) = BE(N,Z) - BE(N-2,Z), \tag{1.6}$$

which is the energy required to remove two neutrons from a nucleus, and the empirical neutron shell gap $\Delta_n$ [15]

$$\Delta_n = S_{2n}(N,Z) - S_{2n}(N+2,Z), \tag{1.7}$$

which is similar to a second derivative of the binding energies. In fact, regions of interesting underlying nuclear structure, can be seen at the $S_{2n}$ or $\Delta_n$ surfaces shown in figures 1.5 and 1.6, respectively. In the $\Delta_n$ surface, some of the clearly seen features include:

- the conventional neutron magic numbers, which appear as bright vertical bands due to sudden changes the the amount of binding when crossing a magic number,
- the $N = Z$ line, where increased binding occurs due to the Wigner energy [16],
- the disappearance of the $N = 20$ and 28 magic numbers near the proton numbers $Z = 12$

and 16 (near the nuclides $^{32}$Mg and $^{40}$Mg as seen by the disapperance of the bright vertical bands,

- regions of deformation near $(N,Z) = (60,40)$ and $(90,62)$, as evidenced by a negative (black) $\Delta_n$,
- and the appearance of 'new' magic numbers at $N = 16$ and $N = 32$ near $Z = 8$ and $Z = 20$ as evidenced by the appearance of bright bands,

The independent particle model of the nucleus has been confirmed by many experiments. The results of electron induced knock-out reactions of protons from $^{206,208}$Pb confirms the expected ordering, spacing, and occupancy of the orbitals [17, 18]. In the $(d,p)$ transfer reaction on $^{132}$Sn [19] the single-particle nature of the states in $^{133}$Sn were confirmed. Both $^{208}$Pb and $^{132}$Sn are doubly magic nuclei, thus, nuclei near doubly magic nuclei obey the independent particle model. However, as already seen in the $\Delta_{\mathrm{n}}$ surface, there are regions with large neutron-to-proton ratios where the standard magic numbers seem to vanish. Thus, a major frontier of nuclear theory is to accurately describe the change in the nuclear interaction as one moves away from stability.

## 1.2 Precision potentials and the need for three-body forces

The general quantum many-body problem for the nuclear Hamiltonian can only be exactly solved in the lightest nuclear systems ($A < 20$), using what are called *ab initio* (Latin for "from the beginning") calculations. The general nuclear Hamiltonian can be written as

$$\hat{H} = T + V = T + \sum_{i<j} V_{ij}^{\mathrm{2N}} + \sum_{i<j<k} V_{ijk}^{\mathrm{3N}} + \dots \tag{1.8}$$

where the potential is expanded in terms of the two-body $V^{\mathrm{2N}}$, three-body $V^{\mathrm{3N}}$, and higher order terms. Many of the widely used nuclear potentials in *ab initio* calculations only include the 2N interaction because it is expected that higher orders will have a small contribution in the calculation [20]. The first nucleon-nucleon (NN) potential was the Yukawa model [21], in which the force between nucleons is mediated by pion exchange,

$$V(r) \propto \frac{e^{-m_\pi r}}{r} \tag{1.9}$$

where $m_\pi$ is the mass of the pion. Intuitively, this internucleon force can be thought of as the residual interaction between colour-neutral nucleons, similar to Van der Waal forces between

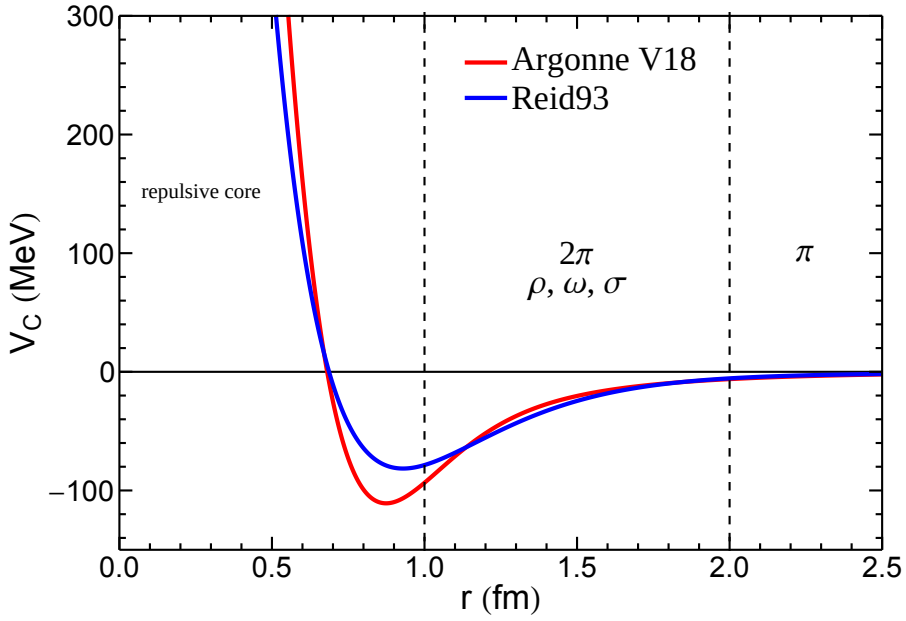


**Figure 1.7:** Examples of the nuclear potential between two nucleons in the $^1S_0$ channel. Note the resemblance to Van der Waals forces. The dashed lines show the regions dominated by one and two pion exchange.

charge-neutral atoms [20]. As seen in figure 1.7 three distinct regions of the NN interaction can be identified: a strongly repulsive core at short ranges, an attractive well at mid-ranges, and a weak long-range attraction. Most models of this type include a central term, spin-spin, spin-orbit, and tensor interactions, with each of these terms included once without isospin dependence and once with isospin dependence. (Isospin is discussed further in section 2.5). The models are constructed using the most general potential that obeys the symmetries of the nucleus: rotation, translation, isospin, etc. [22]. The exact form of the potentials depends both on the method in which the potential operators were derived, and on the choice of the coupling strength for those operators. While the derived potentials may differ in their functional form, they share in common that mesons are the force carriers. The most important meson in the nuclear potential is the pion $\pi$ ($m_{\pi^\pm} \approx 138\,\mathrm{MeV}/c^2$), with small contributions coming from heavier mesons, such as the $\rho$ ($m_\rho \approx 760\,\mathrm{MeV}/c^2$), $\eta$ ($m_\eta \approx 549\,\mathrm{MeV}/c^2$), etc. Examples of often used potentials are Argonne V18 [23], Reid93 [24] and Urbana14 [25].

Up until the 1990's, only the so-called NN potentials were considered, constructed to fit the large body of *nn* and *np* elastic scattering data. However, systematic shifts in the binding energies for multi-nucleon systems could not be accounted for without the inclusion of NNN or 3N interactions. *Ab initio* calculations in light nuclei have demonstrated the need to include 3N-forces in nuclear structure calculations [26]. Figure 1.8 shows the results of the binding

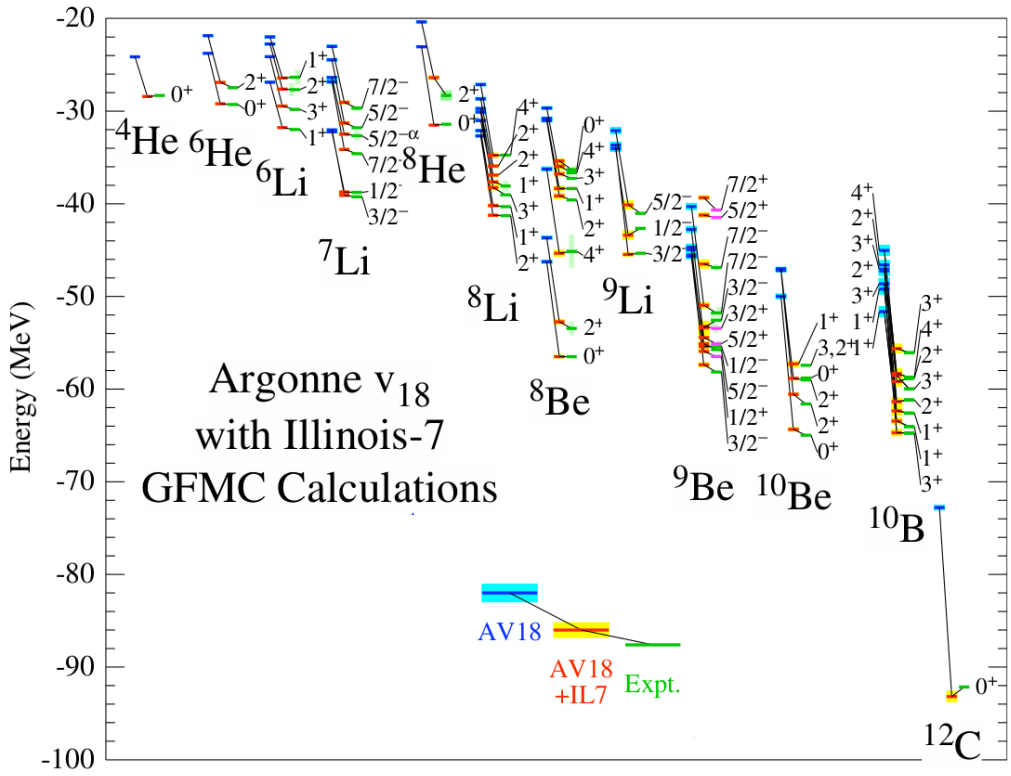


**Figure 1.8:** Binding energies calculated in Green's Function Monte Carlo (GFMC) using the NN potential AV18 (blue) and the 3N potential Illinois-7 (red), as compared to the experimental values (green). Figure reproduced with permission from [26].

and excitation energies of several light nuclei, calculated both using the NN potential Argonne V18 [23], and supplemented with the 3N interaction Illinois-7 [27]. Argonne V18 is the latest NN potential developed at Argonne National Laboratory, and its name is derived from the 18 operator terms used in the model. The 3N Illinois potentials are divided into separate interactions, each with slightly different choices for the potential coefficients [27]. The Illinois-2 and -7 interactions have been widely used in the nuclear community. When studying figure 1.8, we notice that the NN AV18 results (blue), while shifted in energy from the experimental values (green), largely follow the correct level ordering and spacing. However, this is not true in the ordering of the states in $^{10}$B, where the calculated ground state is a $J^\pi = 1^+$, while the measured ground state is $J^\pi = 3^+$. The calculations including the 3N Illinois-7 (red+yellow), show agreement between theory and experiment. The systematic shift in the binding energies is largely accounted for, and the ordering of the states in $^{10}$B is reproduced.

While the addition of a 3N Hamiltonian to the precision NN potentials greatly increases the agreement between theory and experiment, there is no natural way to include their effects in

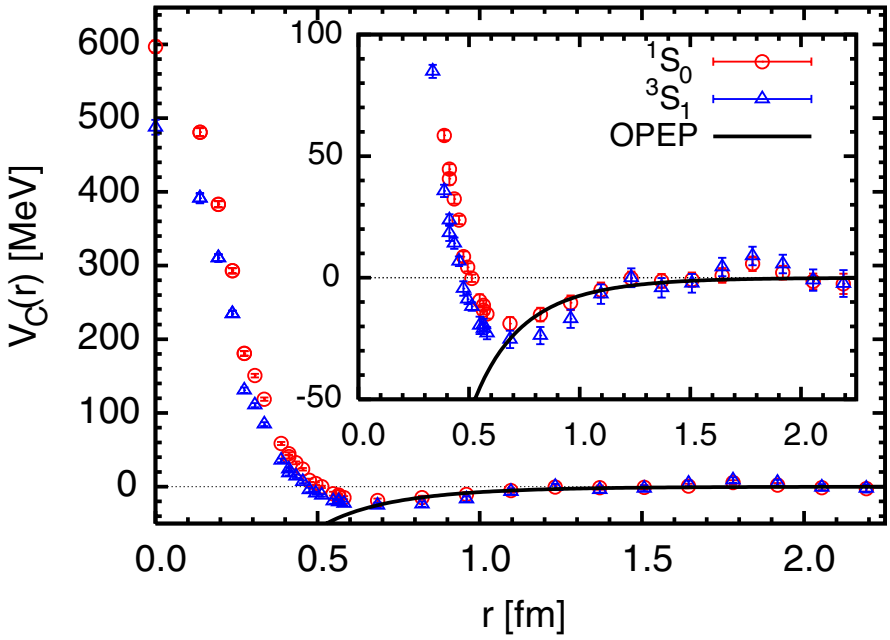


**Figure 1.9:** NN-potential in the singlet and triplet channels, calculated in lattice QCD. The long-range behaviour is similar to the one-pion exchange potential (OPEP) and the hard core is reproduced. Figure reproduced with permission from [30].

these models. Specifically, the inter-nucleon force must derive from Quantum Chromodynamics (QCD), but the precision NN potentials have no strong theoretical foundation in QCD. Currently, modern nuclear interactions are based on Chiral Effective Field Theory ($\chi$EFT). $\chi$EFT attempts to model the interactions between pions and nucleon fields (nucleons, $\Delta$-resonances, etc.) by expanding the scattering amplitudes in small powers of the ratio of the pion mass to the breakdown scale of the theory [28]. In this way, 2N, 3N, and higher order interactions arise naturally in the theory, and there is a clear connection to the underlying QCD. Modern interactions based on $\chi$EFT are discussed further in section 2.1.

While *ab initio* calculations are powerful in predicting the structure of light nuclei, they cannot be directly applied to heavier nuclei due to large increases in the required model space. For example, in the calculation of the ground state of $^{12}$C, as shown in figure 1.8, the solution to the Hamiltonian requires solving a system of 270 336 complex second-order coupled equations in 33 coordinates [29]. Such calculations become intractable for heavier systems. Instead, effective interactions are constructed to reduce the model space. How such effective interactions are constructed, and the role of 3N forces is discussed in chapter 2.

A question that often arises is how well do these potentials connect with the underlying QCD? While these potentials do not intrinsically start from QCD, they do, however, reproduce

the inter-nucleon potential [22]. One direction is to determine the NN potential directly from QCD by calculating the NN potential in lattice QCD. Pioneering work by Ishii *et al.* [30, 31, 32], has shown that the picture of an attractive potential with a hard-core at short distances is correct. Figure 1.9 shows the lattice QCD result for the central part of the interaction in the $^1S_0$ and $^3S_1$ channels. The calculations are compared at long range with the one-pion exchange potential, showing that the expected long-range behaviour is reproduced. Further work [31] shows the hardness, or repulsiveness, of the core depends on the quark mass used in the calculations – as more realistic quark masses are used, the harder the core becomes. As a consequence of the harder core, the medium range attraction is slightly enhanced. The difference between the precision potentials at short range may be related to differences in the underlying quark mass, even though the quark mass is not a direct input.

## 1.3 Mass measurement techniques

As the atomic mass is an important component in determining nuclear structure, several different measurement techniques have been developed, broadly falling into two categories [33, 15]: indirect and direct methods. A common indirect method is a mass measurement through nuclear reactions of the form $A(b,c)D$, where the beam particle $b$ reacts with the target particle $A$, producing a beam-like ejectile $c$ and a target-like recoil $D$. Determining the mass of any of these particles requires knowing at least three of the masses, the kinematics of the incoming channel and the energy of one of the particles in the outgoing channel. Traditionally, reactions can give accurate and precise mass values. Some of the highest precision mass values are from $(n,\gamma)$, $(p,\gamma)$, $(n,p)$, and $(n,\alpha)$ reactions. For example, the separation energy of the deuteron is known to 0.4 eV from the $^1$H$(n,\gamma)^2$H reaction [34]. Neutron-capture reactions require stable, or very long-lived, targets, limiting the possible cases to nuclides close to stability. Slightly more exotic nuclei can be investigated with such reactions by transferring several nucleons from the beam to the target. The reaction mechanism is, however, much more complex, and when combined with low statistics from the small reaction cross-sections, can potentially lead to incorrect results.

Another indirect method determines masses by measuring $Q$-values. The $Q$-value is the total amount of energy available in a decay or reaction, and is related to the difference between the masses of mother and daughter as

$$Q = \sum K_{\text{Final}} - \sum K_{\text{Initial}} = (\sum M_{\text{Initial}} - \sum M_{\text{Final}})c^2 \tag{1.10}$$

where $K$ and $M$ are the kinetic energy and atomic masses of the particles before and after the

decay, respectively. Two common modes for nuclei to decay are $\alpha$- and $\beta$-decay. $Q$-values from $\alpha$-decays provide accurate and precise values owing to the simplicity of the decay—there are only two particles in the out-going channel—and the total energy of the decay can be measured by implanting the parent in a suitable detector. $Q$-values from $\beta$-decays tend to be prone to under-estimating systematic errors because the energy of the decay is shared between three particles: the daughter nucleus, the $\beta$-particle and the neutrino. The $Q$-value is determined by measuring the $\beta$-energy endpoint. However, the response function of the detector has to be well understood, otherwise the extracted end-point energy will be dominated by systematic errors [15]. Further complicating matters, is the fact that in nuclei far from the stable nuclides, the decay $Q$-values are large, which opens up a significant number of decay channels. If these are not properly accounted for, the extracted mass value can be systematically shifted.

While both reactions and $\beta$-endpoint measurements can provide accurate mass values, they can give incorrect results arising from complex systematics in the measurement device and co-produced contamination. An example of an incorrectly determined mass was $^{46}$V, where a direct Penning trap mass measurement differed by more than $3\sigma$ from a $(p,\gamma)$ reaction [35]. The mass value of $^{46}$V was subsequently confirmed by another direct Penning trap system measurement [36, 37]. In $\beta$-endpoint measurements, it is generally seen that mass values from $\beta$-decay measurements underestimate the binding. For example, the $Q$-value for the decay of $^{85}$Nb was found to be 900 keV larger in a Penning trap measurement [38] than in the $\beta$-endpoint measurement [39]. Many of the known mass values used in $r$-process calculations (section 1.4.2) critically depend on the results of $\beta$-endpoint measurements; thus, independent verification of these masses is required.

To overcome the limitations of these indirect methods, several direct mass measurement techniques have been developed. The data collected in direct measurements are often simpler to interpret than the data from indirect methods, allowing for precise and accurate mass measurements of nuclides not only with short half-lives ($t_{1/2} < 100$ ms), but also those produced at very low rates. The main methods [33, 15] rely on measuring either the time-of-flight (TOF) [40] or the cyclotron frequency of an ion [41, 42] (section 3.3.4). Traditionally, time-of-flight techniques have used magnetic spectroscopy systems, such as SPEG at Ganil [43], where the time-of-flight is measured between two microchannel plate detectors. Time-of-flight techniques have generally been relegated to facilities where fast ($E_{\mathrm{kin}} \approx$ several MeV/nucleon to GeV/nucleon) production beams are used. One such device is the Experimental Storage Ring [44] at the GSI facility in Darmstat, Germany. By measuring the revolution frequency of an ion stored in the ring [40], it is possible to determine the mass when the flight path, and

hence the total length is known. Resolving powers of up to $m/\delta m \approx 10^6$ can be reached with storages times of $\approx 1$ s, and resolving powers of $\approx 10^5$ can be reached after 50 $\mu$s [45]. A recent development is the Multi-Reflection Time-of-Flight device, which captures low-energy beams ($E_{\mathrm{kin}} \approx 2\,\mathrm{keV}$) between a pair of electrostatic mirrors. In this way, the flight path of the ion can be increased to several kilometres, allowing for resolving powers of $\approx 10^5$ for flight times of several tens of milliseconds [46, 47, 48].

For the highest precision, the tool of choice is a Penning trap. High-precision measurements are achievable due to the unique storage environment: Single charged particles are held for long times in high vacuum, with well defined trapping potentials. Relative atomic mass precisions of below $10^{-8}$ have been reached for unstable nuclei with half-lives below 100 ms [41], and $10^{-11}$ for stable nuclei [42]. Examples of the performance of Penning traps are:

- some of the most stringent tests of CPT symmetry, comparing the antiproton and proton charge-to-mass ratios to 90 ppt [49]
- the most precise atomic mass values for stable nuclei, 11 ppt for $^{16}$O, and 94 ppt for the mass of the electron [50]
- and precise $Q$-value measurements of superallowed $\beta$-emitters [51] to determine the quark mixing matrix element $V_{ud}$ of the Cabibbo-Kobayashi-Maskawa (CKM) matrix.

TRIUMF's Ion Trap for Atomic and Nuclear science (TITAN) [52] is one such Penning trap system. Due to the ion production source and the ion injection method into the trap, TITAN is capable of performing precise and accurate measurements on short-lived isotopes that cannot be measured by other Penning traps. The work described here was carried out using the TITAN system, and is described in detail in section 3.3.

## 1.4 The importance of Penning-trap mass measurements

Atomic mass measurements play an important role in many aspects of nuclear physics, relevant for questions from the smallest scale — is the quark mixing matrix unitary within the Standard Model of particle physics? — to the largest scales — how are elements heavier than iron made in hot astrophysical environments? The atomic mass is important in studying new and emerging phenomena in nuclei, e.g. nuclear halos [53], in studying the evolution of "magic numbers" [54, 55], and in studying the onset of deformation [56, 57]. Precise and accurate mass values provide stringent tests of nuclear theory [58, 59].

The binding energy (Eq. 1.5), which is derived from the atomic mass, is important because it reflects the sum of all the interactions at play in the nucleus, making it sensitive to interactions

that may only be observed far from stability. The following describes examples of regions where mass measurements are important for nuclear physics.

### 1.4.1 Cabibbo-Kobayashi-Maskawa unitarity

The Cabibbo-Kobayashi-Maskawa (CKM) matrix is a unitary transformation matrix relating the quark mass eigenstates to the flavour eigenstates:

$$\begin{pmatrix} d_w \\ s_w \\ b_w \end{pmatrix} = \begin{pmatrix} V_{ud} & V_{us} & V_{ub} \\ V_{cd} & V_{cs} & V_{cb} \\ V_{td} & V_{ts} & V_{tb} \end{pmatrix} \begin{pmatrix} d_s \\ s_s \\ b_s \end{pmatrix} \tag{1.11}$$

where $u$, $c$, $t$, $d$, $s$, $b$ are the up, charm, top, down, strange, and bottom quarks, and the subscript $s$ and $w$ denote the strong and weak eigenstates. Because the CKM matrix is defined to be unitary in the Standard Model, the sum of the squares of any row or column should be 1, with any deviation from this indicating that extra quark generations or other physics beyond the Standard Model may be required. Currently, the most stringent unitary test is done using the first row of the matrix

$$|V_{ud}|^2 + |V_{us}|^2 + |V_{ub}|^2 = 1. \tag{1.12}$$

The element $|V_{ud}|^2$ accounts for nearly 95% of the first row's size. $V_{ud}$ is special among the CKM elements as it can be accessed by nuclear physics through superallowed $0^+ \rightarrow 0^+$ Fermi $\beta$-decays, due to the simplistic nuclear structure. Occurring between isobaric analogue states (states that are related by isospin-lowering and isosping-raising operators), superallowed $\beta$-decays used for tests of the CKM matrix are almost independent of nuclear structure. The nuclear matrix element of the decay differs from a Clebsch-Gordan coefficient at the few percent level, largely due to charge-dependent effects in the nuclear interaction. The other elements of the CKM matrix lie in the domain of particle physics, and are typically measured at collider facilities [60]. Electron capture and $\beta$-decay in nuclear systems transforms a proton $(u,u,d)$ into a neutron $(u,d,d)$, or vice-versa for $\beta^+$-decay. From this one can access $|V_{ud}|$. Assuming the conserved vector current hypothesis [61], the $\beta$-decay $ft$-value can be written as

$$ft = \frac{K}{G_V |M_F|^2} \tag{1.13}$$

where $K$ is a constant, $G_V$ is the vector coupling constant, and $M_F$ is the matrix element connecting the initial and final states. The $ft$-value is called the "comparative half-life" of the decay, accounting for the available phase space $f$ and the half-life $t$ of the decay. The vector

coupling constant can be written as $G_V = V_{ud} G_\mu$, where $G_\mu$ is the coupling constant for the purely leptonic decay of the muon. The experimental $ft$-value depends on the three experimental values:

1. the half-life of the superallowed decay,
2. the branching ratio to the $0^+$ state,
3. and the $Q$-value of the decay to the $0^+$ state.

Because the $ft$-value depends on the $Q$-value to the fifth power $Q^5$ [51], precise and accurate mass values are required.

### 1.4.2 Nuclear astrophysics

Extremely neutron rich nuclei can be produced in hot astrophysical environments, such as core-collapse supernovae [62] or neutron star mergers [63], which are considered as sites for the so-called rapid-neutron capture process (r-process). Because the involved nuclei are extremely neutron rich and difficult to produce in the laboratory, there is a distinct lack of experimental knowledge on all required quantities: half-lives, $\beta$-delayed neutron decay probabilities, separation energies, etc. This information is needed to develop a complete understanding of the process and the resulting chemical element abundances. Besides the nuclear physics properties, astrophysical sites need to be investigated and understood. Without experimental values for the required nuclear properties, nuclear astrophysicists rely on nuclear models. Figure 1.10 shows the range of calculated elemental abundances for four different mass models. These models are able to accurately predict masses where data exists, but they greatly diverge from each other where the mass values are not known. This results in a wide range in the predicted chemical abundances. Through precise and accurate mass measurements, more reliable and realistic descriptions of nucleosynthesis are possible. Therefore, sensitivity studies have been performed to determine the nuclei where masses have the largest influence on the final abundances [64].

### 1.4.3 Nuclear halos

In 1985, a remarkable observation was made in a radioactive beam experiment at the Lawrence Berkeley National Laboratory: The matter radius of $^{11}$Li was found to be much larger than that of adjacent nuclei [66]. Subsequent theoretical and experimental studies led to a coining of the name “halo nucleus”. Nuclear halos are characterized by a long tail in the matter distribution, related to the weak binding of the halo nucleons. Departing from the normal $r \propto A^{1/3}$ scaling

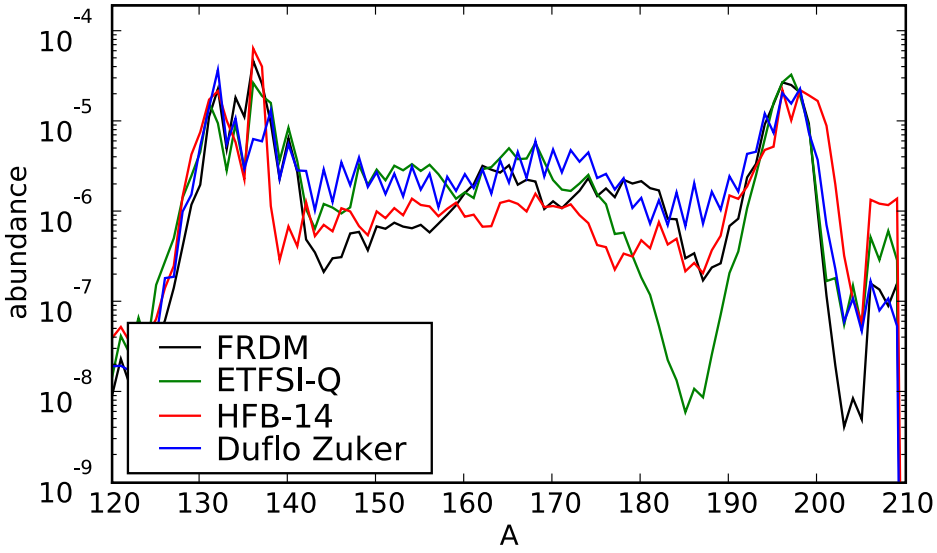


**Figure 1.10:** Model dependence of *r*-process abundances for three different mass models. Figure reproduced with permission from [65].

in nuclei near stability, $^{11}$Li is comparable in size to $^{208}$Pb, even though they are $\approx 200$ mass units apart.

In $^{11}$Li two neutrons are loosely bound to a $^{9}$Li core, displaying a two-neutron separation energy of only $S_{2n} = 369\,\text{keV}$ [67]. From the extended matter distribution several key features can be extracted: the halo nucleons are in low angular momentum states, otherwise the centrifugal barrier would suppress the wave function. Moreover, the separation energy of the halo nucleons needs to be small, otherwise the potential well would suppress the wave function at long distances [68]. The extended matter distribution also manifests itself in a much larger reaction interaction cross-section than would normally be expected [68]. There are several types of halo nuclei, classified by the number of nucleons that comprise the halo [68]: the one neutron halos $^{11}$Be and $^{19}$C, the two-neutron halos $^{11}$Li and $^{6}$He, amongst others, and the four-neutron halos $^{8}$He and $^{14}$Be. Several proton halo nuclei are considered, such as the one-proton halo $^{26}$P and the two-proton halo $^{17}$Ne, however there are fewer proton halo nuclei than neutron halo nuclei [68]. Since halo nuclei are so weakly bound, the separation energy, and hence, the mass, is an important component in determining their structure, and a key ingredient for testing theoretical predictions.

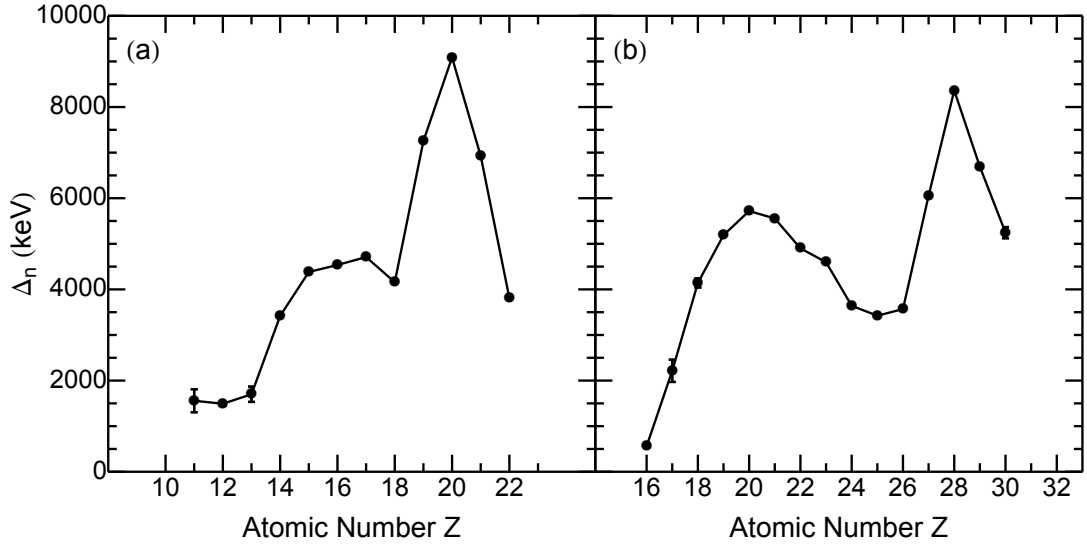


**Figure 1.11:** Disappearance of (a) $N = 20$ and (b) $N = 28$ magic numbers, seen through the semi-empirical shell gap $\Delta_n$. Data from [69].

### 1.4.4 Shell structure evolution

Most nuclear models have only been constrained with data near the stable nuclides, and only recently have data from nuclei with extreme proton to neutron ratios become available. Isospin is an approximate symmetry of nucleons, and the nuclear interaction can be parametrized in terms of isospin (isospin is discussed further in section 2.5). The important point for the present discussion, is that the nuclear interaction is different in the $T = 0$ (proton-neutron) channel than in the $T = 1$ channel (proton-proton or neutron-neutron) [70]. Near the stable nuclides the $T = 0$ channel dominates because of the nearly equal number of protons and neutrons, but moving far from these stable regions the $T = 1$ channel becomes increasingly more important, a change that may affect the location of the standard magic numbers [70]. As an example, figure 1.11 shows the empirical shell gap $\Delta_n$ 1.7 along the $N = 20$ and 28 isotones. In progressively neutron-rich nuclei the shell gap drops below 2 MeV, an indication that the neutron number is no longer magic, as typical shell gaps are found to be around 4 MeV.

In these regions of reduced shell gap strength, the ground state may be an "intruder" state [71]. An intuitive understanding of intruder states can be found through the following

example. Consider a Hamiltonian with $n$ degenerate states, all coupled with the same strength:

$$\hat{H} = -\begin{pmatrix} \varepsilon & \Delta & \Delta & \\ \Delta & \varepsilon & \Delta & \dots \\ \Delta & \Delta & \varepsilon & \\ & \vdots & & \ddots \end{pmatrix}$$

where $\varepsilon$ is the energy of the degenerate states, and $\Delta$ is the interaction strength between them. One state, the correlated state, shifts down by $-(n-1)\Delta$, while the other states shift up by $\Delta$. If the coupling between the states is large, this correlated state can drop below any lower energy states, thus becoming an "intruder" state. In atomic nuclei, an intruder state occurs when nucleons populate a state that would normally be higher in energy and, through a large gain in correlation energy due to particle-hole excitations, causes the state to drop below the "normal", or expected, state [71]. Regions of inversion have been experimentally found to lie where the magic numbers begin to vanish. There may still be a large shell gap in the single-particle energies, which is an indication of a shell closure, but the large gain in correlation energy causes a re-ordering of the states [72]. A prime example is $^{32}$Mg, which is the start of the "island-of-inversion" (figure 1.11 (a)) [73, 74]. The expected ground state would be $J^{\pi} = 0^{+}$, made up of protons in the $0d_{5/2}$ and neutrons in the $0d_{3/2}$ states. Instead, the ground state is a deformed $0^{+}$ state, formed by neutrons predominantly in the $1p_{3/2}$ and $0f_{7/2}$ orbitals [75]. This is also confirmed by the observation that the ground state of $^{33}$Mg is largely a neutron in the $1p_{3/2}$ on top of a $^{32}$Mg core [76].

A similar region of inversion occurs along the $N = 28$ magic number. Large deformation is seen in the ground-state of $^{42}$Si [77, 78], and there are indications that this deformation might continue into $^{40}$Mg [79, 80]. Early theoretical investigations show that the ground-state structure of the $N = 28$ isotones rapidly changes from a spherical configuration in $^{48}$Ca through a vibrational configuration in $^{46}$Ar, to oblate (flattened spheroid shape) in $^{42}$Si, and prolate (elongated spheriod shape) in $^{40}$Mg [54]. More data is needed to clarify the structure evolution in this region, and mass measurements will play a vital role in these investigations.

Magic numbers cannot only disappear, they can also appear unexpectedly [81]. One example that has received much attention is the appearance of a new magic number at $N = 16$ [82, 83, 84] in the oxygen isotopic chain. By now $^{24}$O is fully considered to be a doubly magic nucleus: systematic trends in the mass surface point to an increase in binding at $^{24}$O, the ground state of $^{24}$O is $s$-wave, as predicted by the shell model, and a large excitation energy for the first $2^{+}$ state. Other proposed new magic numbers are at $N = 32, 34$ near $Z = 20$

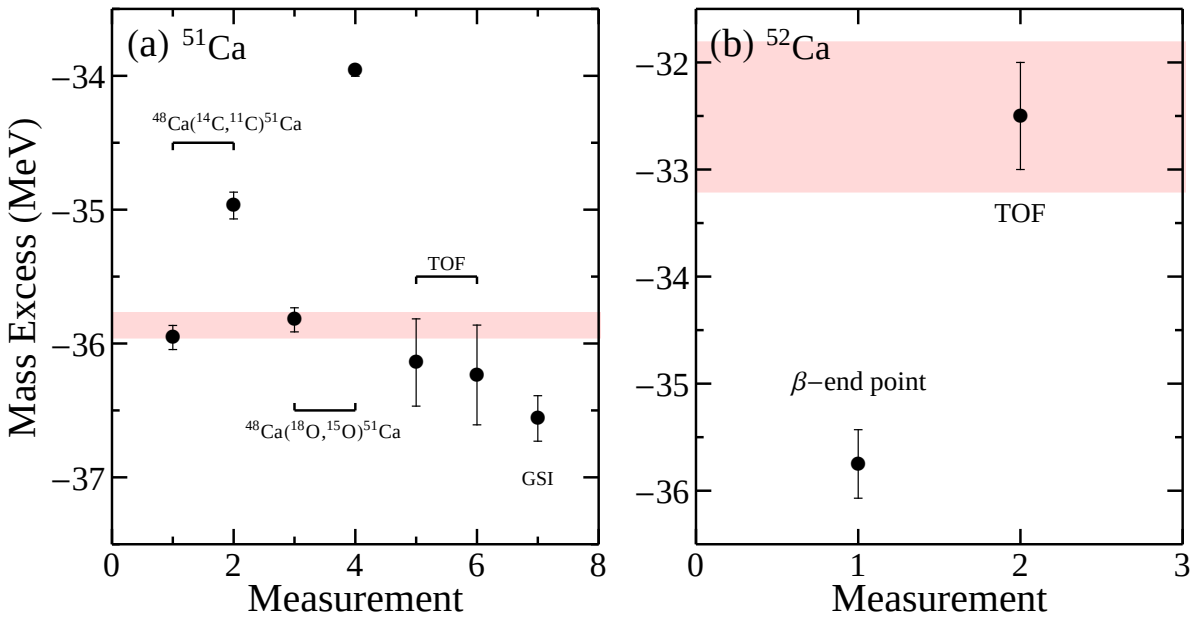


**Figure 1.12:** Historical mass excesses for (a) $^{51}$Ca, and (b) $^{52}$Ca. The red band is the value adopted in AME03 [85]. Individual measurements are discussed further in sections 4.1.1 and 4.1.2.

[81].

## 1.5 Penning-trap mass measurements to test 3N forces

As we have seen, the atomic mass is an important component in many aspects of nuclear physics, and provides a significant tool in testing nuclear models. Three-nucleon forces were shown to be crucial in reproducing the global binding energies of light nuclei in *ab initio* calculations, however, their role in medium mass nuclei is unknown. In this thesis we will test the role of 3N forces in medium mass nuclei through precision mass measurements. Specifically, we will test established phenomenological interactions that only include two-body effects, and new interactions, derived from chiral effective field theory ($\chi$EFT), a low-energy perturbation expansion of QCD, that provides a framework for including 3N effects. How such models are constructed is discussed in chapter 2.

First, the masses of the neutron-rich nuclei $^{51,52}$Ca were measured to test the possibility of new shell closures near $N = 32$ and 34. The measurements are compared to predictions from well established interactions based on 2N forces, and modern interactions that include the effect of 3N forces. Further, the measurements that exist in this region are in strong disagreement, as can be seen in figure 1.12. A precision mass measurement was needed to clarify the mass values

of these nuclides. Second, the masses of $^{20,21}$Mg were measured to test the role of 3N forces in the isobaric multiplet mass equation (section 2.5). These two measurements probe different aspects of the 3N force. As the calcium isotopes are at a proton magic number ($Z = 20$), the protons do not strongly interact with the active neutrons, providing insight into the 3N neutron-neutron interaction. On the other hand, the proton-rich Mg measurements probe the 3N interaction when both protons and neutrons are active in the calculation.

# Chapter 2

# Nuclear theory

NN potentials currently lead to unsatisfactory results in comparison with experiment, but this can be overcome through the use of interactions based on chiral effective field theory ($\chi$EFT) which gives a systematic approach to including the effect of 3N forces. This chapter will introduce how $\chi$EFT based interactions are used in modern nuclear physics calculations, how these calculations compare to existing interactions based on phenomenology, and how mass measurements can be used to tests these theories.

## 2.1 Chiral effective field theory

Chiral symmetry is only a true symmetry in the limit of massless quarks [61]. Since the masses of the $u$ and $d$ quarks are light compared to the mass of a nucleon, the chiral symmetry can be treated as an approximate symmetry. As in any EFT, the degrees of freedom must be determined, and in the nucleus, the relevant degrees of freedom are the protons, neutrons and exchange pions. Generally, the chiral effective Lagrangian used for nuclear theory only condsiders the $u$ and $d$ quarks, and from the spontaneous symmetry breaking of the chiral symmetry, three pseudo-Goldstone bosons [61] act as the force carriers. In modern $\chi$EFT interactions only the pion is considered, which is a natural choice due to the large mass gap of $\approx 600$ MeV/$c^2$ to the $\rho$-meson. The breakdown energy $\Lambda$ of the EFT is chosen be between the pion mass and the nucleon mass, and, in practice, $\Lambda$ is taken between 500-700 MeV. The interaction can then be expanded in powers of $Q/\Lambda$, where $Q$ is the "soft scale" of the EFT and is typically close to the mass of the pion [86]. This chiral expansion of QCD in the nucleonic sector solves many of the problems with the precision NN interactions: $\chi$EFT allows for an expansion of the nuclear interaction order by order, allowing for theoretical uncertainties to be assigned, $\chi$EFT naturally explains the observed hierarchy of the NN, 3N, etc. forces in a consistent framework.

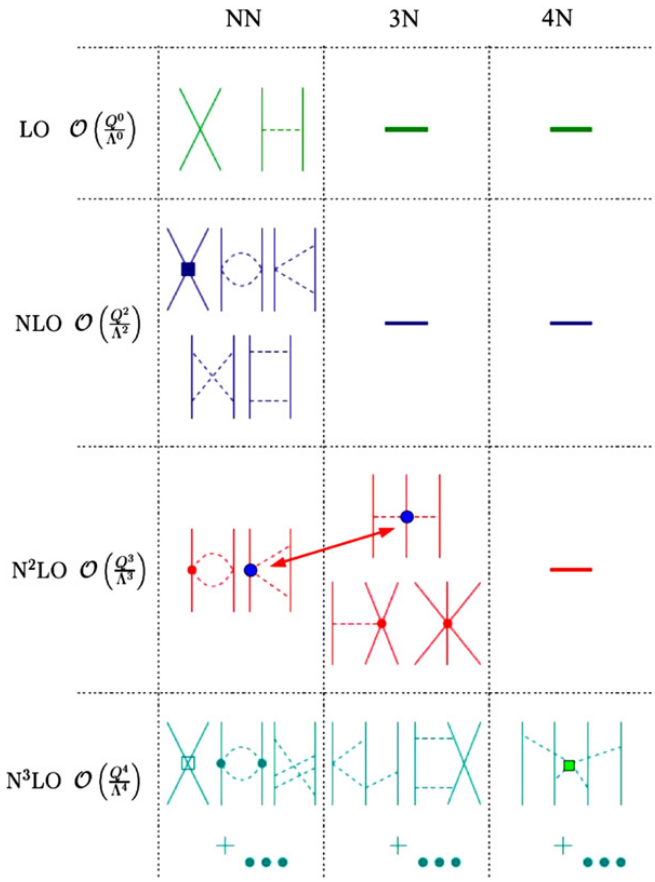


**Figure 2.1:** Order by order $\chi$EFT diagrams for NN, 3N and 4N forces. Orders are: leading order (LO), next-to-leading order (NLO), next-to-next-to-leading order (N$^2$LO), etc. Figure reproduced with permission from [87].

Lastly, $\chi$EFT has a clear connection to QCD. Figure 2.1 shows the leading terms in the $\chi$EFT interaction.

An essential ingredient to any effective field theory are contact interactions that capture the physics of the neglected degrees of freedom. These contact interactions are captured in contact terms that can be either calculated from existing theories or fit to experimental data. For the nuclear interactions we are concerned with, the two-body terms are generally fit to the $\pi$-$N$ and $N$-$N$ scattering data, while the 3N terms are fit to reproduce observables in light many-body systems, such as $^3$H and $^4$He. Herein lies the power of the $\chi$EFT formulation: the coupling constants are fit once to experiment, and the resulting interactions should then be applicable to the whole nuclear chart.

A problem with using the bare chiral potential is the strong coupling between low- and high-momentum states. The coupling of high and low momentum components in these bare

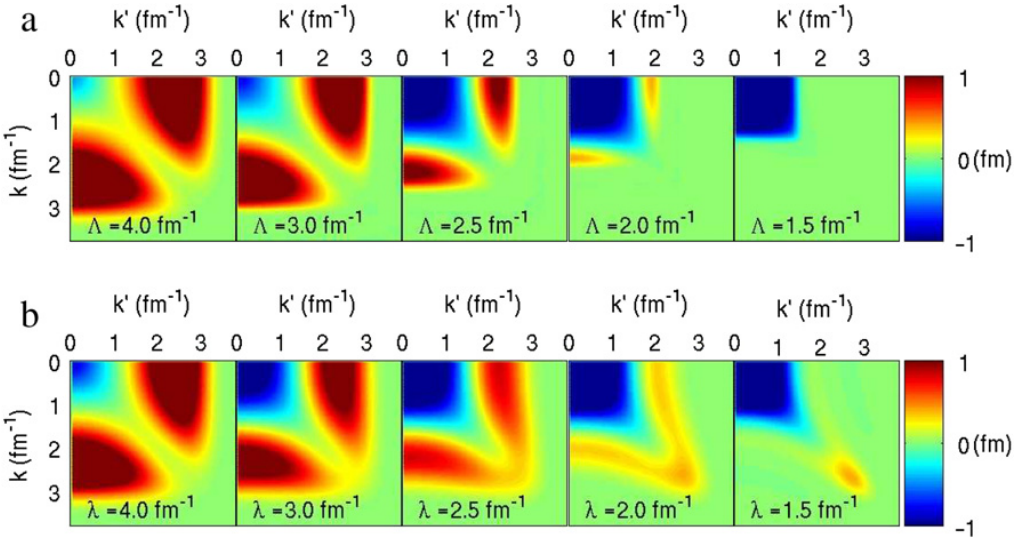


**Figure 2.2:** Renormalization group (RG) evolved $\chi$EFT potentials at N$^3$LO with $\Lambda =$ 500 and 600 MeV in the $^1$S$_0$ channel. (a) $V_{\mathrm{low}\,k}$ (b) SRG. Figure reproduced with permission from [87].

interactions requires extended model spaces to achieve converged results for nuclear physics calculations, presenting a large computational challenge. The hard core also causes uncorrelated two-body wave functions to diverge because the wave functions has a non-zero value at distances less than the hard core radius. The high-momentum components can be removed by evolving the interaction to low momentum through renormalization group techniques, one such technique being the $V_{\mathrm{low}\,k}$ approach. An interesting side-effect of these procedures is that at low momentum, all potentials have the same form – there is a universal potential at low momentum – as can be seen in figure 2.2. This happens because the renormalization procedure integrates out the high-momentum components. A side effect of this renormalization is that the high-momentum components are "shuffled" to higher-body forces (*e.g.* high-momentum NN terms are moved into the effective 3N and higher terms). The short range potential differs between the various interactions, however the long-range, low-momentum parts are the same, leading to comparable low momentum interactions.

Several other techniques to soften the potential have been introduced in recent years. One class, called the Similarity Renormalization Group (SRG) [88], uses a continuous sequence of unitary transformations to drive the Hamiltonian to a band diagonal form (figure 2.2 (b)). This results in an evolved form that differs from the global $V_{\mathrm{low}\,k}$ form, although the low momentum parts of the two are quite similar. SRG evolved potentials have the advantage that high-energy phase shifts are preserved, unlike in $V_{\mathrm{low}\,k}$ potentials. Extensions to the SRG, called the In-

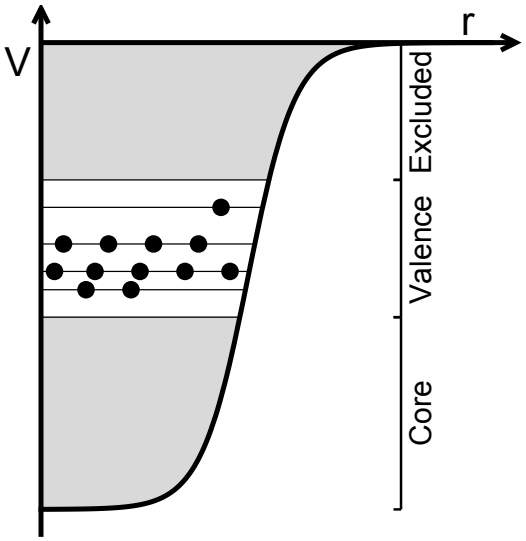


**Figure 2.3:** Schematic valence space for an effective interaction. Valence nucleons can only interact with themselves. The core and higher lying states are inert and excluded from the calculation.

Medium SRG[89, 90] and multireference IM-SRG [91], have also been developed. Instead of evolving the interaction in free space as done in SRG, IM-SRG evolves the potential in the medium of the many-body system being studied. This allows for the evolution of arbitrary order operators using only the machinery required for the two-body case. All of these techniques successfully reproduce experiment in a wide range of nuclear systems [88, 89, 90, 91].

## 2.2 Effective interactions

For all but the lightest systems, full *ab initio* calculations are not possible due to the exponential increase in the required model space. Theory then turns to effective interactions, where effective Hamiltonians are built in a valence space on top of a core nucleus, shown schematically in figure 2.3. This is done to reduce the model space of the calculation. To show this, we now sketch the steps required to build an effective interaction [92]. First, we set up the Schrödinger equation

$$H\Psi_\lambda = E_\lambda \Psi_\lambda, \tag{2.1}$$

where the Hamiltonian can be written as

$$H = T + V = (T + U) + (V - U) = H_0 + H_1 \tag{2.2}$$

where $V$ is the internucleon interaction and $U$ is a convenient potential, typically chosen to be

the harmonic oscillator,

$$U = \sum_{i=1}^{A} \frac{1}{2} m\omega^2 r_i^2. \tag{2.3}$$

The wavefunction $\Psi_\lambda$ is then expanded in the basis states $\phi_0$ of $H_0$. To reduce the dimensionality of the problem, the basis states are written in terms of the closed core $|c\rangle$. The core is usually a doubly magic nucleus, such as $^{16}$O or $^{40}$Ca, in which nucleon excitations from the core into the valence space are prohibited. Next, two projection operators are defined, $P$ and $Q = 1 - P$, where $P$ acts to project from the complete space into the valence space, while $Q$ acts to project into the excluded space. The eigenvalue problem now reduces to

$$PH_{eff}P\Psi_\lambda = E_\lambda P\Psi_\lambda, \tag{2.4}$$

and if we calculate the binding energies relative to the closed core,

$$PH'_{eff}P\Psi_\lambda = (E_\lambda - E_c)P\Psi_\lambda, \tag{2.5}$$

where $H_{eff}$ is the effective Hamiltonian in the valence space of interest, and $H'_{eff}$ is the shell model effective Hamiltonian. The effective Hamiltonian can then be decomposed into two parts

$$H'_{eff} = H'_0 + v_{eff} \tag{2.6}$$

where $H'_0$ is the one-body Hamiltonian, measuring the binding energy of single particles with respect to the core, and $v_{eff}$ is the effective interaction between all nucleons in the valence space. In general, there are up to n-body interactions in the valence space, where n is the number of nucleons in the valence space, but typically only the two-body matrix elements were considered. Using the two-body approximation, the general effective Hamiltonian is

$$H_{eff} = \sum \varepsilon_\alpha a^\dagger_\alpha a_\alpha + \frac{1}{4} \sum \langle \alpha\beta | V | \delta\gamma \rangle \, a^\dagger_\alpha a^\dagger_\beta a_\delta a_\gamma \tag{2.7}$$

where $\varepsilon_\alpha$ is the single particle energy, Greek indices label states in the valence space, and $V$ is the effective interaction between two valence nucleons. The single particle energies can be taken empirically to be the difference in binding energy between the state $\alpha$ in a closed-shell + 1 nucleon nucleus and the corresponding closed shell nucleus. Alternatively, the single particle energies can be calculated self-consistently by calculating the one-body attached states in the nuclei of interest. Three issues need to be solved to use the above formalism: the valence space has to be chosen to contain the degrees of freedom for the specific physical quantity of interest,

the effective interaction $v_{eff}$ needs to be determined from the original Hamiltonian $H$, and a numerical framework must be developed to diagonalize the resultant matrix.

First, valence spaces were historically chosen to be the major oscillator shells of the harmonic oscillator (see figure 1.3):

- the $p$-shell consisting of the $0p_{3/2,1/2}$ orbits,
- the $sd$-shell consisting of the $0d_{5/2,3/2}$ and $1s_{1/2}$ orbits,
- the $pf$-shell consisting of the $0f_{7/2,5/2}$ and $1p_{3/2,1/2}$ orbits.

Several widely used interactions are the the following: the Universial $sd$ (USD) interactions USDA and USDB [93], which describe nuclei in the $sd$-shell, and the mass-dependent Kuo-Brown interaction (KB3G) [94] and the $G$-matrix, experimentally fit interaction (GXPF1A) [95], which describe nuclei in the $pf$-shell.

Second, the effective interaction Hamiltonian needs to be determined. One method to produce effective interactions, is to perform a perturbation calculation of an existing NN potential, including effects of the nuclear medium to the matrix elements [92]. Once the set of interaction matrix elements is produced, minor adjustments are generally performed to known experimental values, resulting in a interaction that not only reproduces experiment where data is available, but also offers some predictive power. Falling under this approach is the KB3G interaction, the latest version of the Kuo-Brown interaction, which was one of the first attempts at a realistic interaction. Kuo and Brown started from a precision NN potential of the time, employed a $G$-matrix renormalization [96], and calculated the matrix elements to second order. The KB interaction showed spectacular agreement to the energy levels in $^{18}$O and $^{18}$F [97]. The KB3G interaction is the modern incarnation of the original KB interaction, having had the matrix elements and single particle gaps adjusted to provide better agreement with experiment. Other approaches consist of fitting the matrix elements to all of the existing data available. Falling under this approach are the USD [98] and GXPF1 interactions. The USD interaction was first formulated in the 1980's, and had 63 matrix elements fit to experimental data. Even this modest number of elements to be fitted required two years of computer time, which would only take an afternoon on a modern PC [99]. The GXPF1 interaction was also fit to experimental data, with 195 two-body elements and four single particle energies fit to 699 energy data.

Lastly, codes need to be developed to diagonalize the large matrices generated in the valence space. Many such codes exist, such as ANTOINE [100], NATHAN [100], and OXBASH [101]. Each code employs different coupling schemes to generate the basis states, and thus, the selection of code depends on the specific nucleus being calculated. For example,

the number of elements in the Hamiltonian to be diagonalized for $^{56}$Ni in the full $fp$-shell is 1 087 455 228 in the shell model code ANTOINE, and 15 443 684 in the code NATHAN. Such large matrices are diagonalized using the Lanczos algorithm [102] until convergence is reached.

In order to provide better agreement with experiment, new two-body interaction terms have been explored. One possibility is the tensor force, which acts between $S = 1$ coupled protons and neutrons [103]. When the proton and neutron have total angular momentums of $j_> = l + 1/2$ and $j'_< = l' - 1/2$, the tensor force is attractive. Alternatively, when the proton and neutron are both in $j_>$ or $j_<$ states the tensor force is repulsive. The tensor interaction reproduces the observed magic and sub-magic shell closures, while being completely two-body in nature.

Others argue that rather than introducing new NN terms or fitting the matrix elements to a large body of experimental data, one should include 3N terms [104]. It may be that these new two-body terms or adjustments mimic three-body interactions. As shown earlier, 3N forces were required to provide good agreement between theory and experiment in light systems, thus it may be that 3N forces are also required in these effective interactions.

## 2.3 Modern $\chi$EFT based calculations

A commonality between all of the above interactions is they largely start from effective interactions derived from precision NN potentials and are then phenomenologically adjust the two-body matrix elements to reproduce experimental observables in the valence space of interest. This approach has lead to several iterations of existing models. For example, the USD interaction was originally developed in the 1980's [98], but in 2006 two updated USD interactions, USDA and USDB [93], were developed to account for both the increase in experimental knowledge in the *sd*-shell, and the increases in theoretical tools to develop the effective interaction. Both interactions start from the two-body matrix elements derived from a renormalized *G*-matrix effective interaction. On one hand, the USDA was constrained to remain close to the starting effective interaction, giving a reasonable fit to the data but still remaining close to the initial derived effective interaction; on the other hand, this constraint was removed for the USDB, resulting in an interaction that is the best fit to the data. Similar changes have been made to interactions in the $pf$-shell, such as the KB family: KB [105], KB3 [106], and KB3G [94]; and the GXPF family: GXPF1 [107] and GXPF1A [95]. Modern effective interactions now start with the $\chi$EFT internucleon interactions, and derive the effective interaction without resorting to phenomenology, *i. e.*, the fitting of matrix elements to data in the region applicable to the model. Since these $\chi$EFT based interactions tend to have their coupling constants

determined in light nuclear systems, a truly predictive nuclear interaction is obtained.

There are several approaches for solving the many-body Schrödinger equation in the valence space. One approach is to adapt *ab initio* type calculations for use in medium mass nuclei. For example, calculations with the importance truncated no-core shell model have reproduced the binding energies of $^{16,24}$O and $^{40,48}$Ca [108], providing important benchmarks for methods based on coupled-cluster theory [108]. In principle, these methods are exact, but they are truncated to make the calculation computationally tractable. Coupled-cluster theory uses a similarity transformed Hamiltonian $H = e^T \hat{H} e^{-T}$, where $T$ is the cluster operator. $T$ acts to create $n$-particle $n$-hole states with respect to a reference state as,

$$T = T_1 + T_2 + T_3 + T_4 + \ldots + T_A \tag{2.8}$$

where the $T_i$'s are the $i$-particle $i$-hole cluster operators. This formulation is exact, provided that $T$ is allowed to create $A$-body excitations. In practice, $T$ is truncated to only include one- and two-body excitations, an approximation termed the Coupled-Cluster Singles-Doubles (CCSD). The inclusion of 3N forces poses a problem for CC-based calculations, as the computational cost increases by orders of magnitude. To overcome this, the 3N force is reduced to an effective two-body force by integrating the chiral 3N force over the Fermi sea in symmetric nuclear matter [109]. Other methods involve constructing an effective interaction from the bare $\chi$EFT potentials and then solving the Schrödinger equation using many-body perturbation theory [8]. These effective interactions can then be used with existing shell model codes.

Another approach uses Many-Body Perturbation Theory (MBPT) in a traditional shell model framework. The effective interaction is built by evolving the $\chi$EFT interaction with $\Lambda = 500\,\mathrm{MeV}$ to low momentum, and is called $V_{\mathrm{low}\,k}$. The NN interaction is included at the next-to–next-to–next-to leading order (N$^3$LO) level, while the 3N interaction is included at the N$^2$LO level (see figure 2.1). Three-body effects are included by including the normal ordered one- and two-body 3N interaction, corresponding to interactions between valence nucleons and core nucleons. The residual 3N interaction between the valence nucleons is not included, as CC calculations have shown that these interactions are small compared to the normal ordered 3N interaction [110]. These effective 3N interactions provide important repulsion between the valence nucleons, increasing the spin-orbit splitting of the single particle energies [111].

The CC and shell model methods have had great success in reproducing experiment. Moreover, these two different approaches provide quite similar results, provided both calculations start with consistent single-particle energies. Figure 2.4 compares CC and MBPT ground state calculations in the calcium chain, where each calculation is based on the same NN potential.

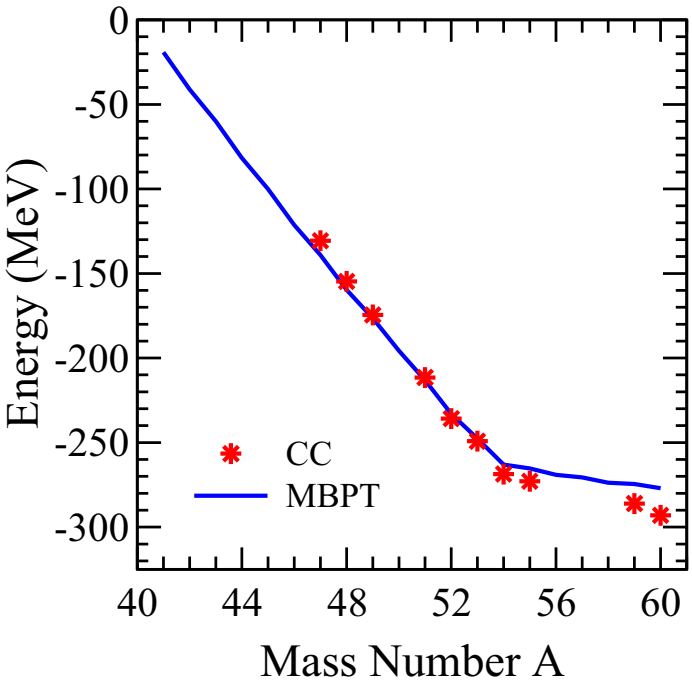


**Figure 2.4:** Comparison in calcium ground state energies calculated in coupled-cluster (CC) and valence space many-body perturbation theory (MBPT). Figure reproduced with permission from [111].

The calculated ground state energies are quite close to each other, only deviating in the heavy calciums. This is due to differences in the filling of the orbitals in these nuclides [111]. Another example is the long standing problem of the oxygen drip-line anomaly. The neutron drip-line in the C, N and O isotopic chains ends at $N = 16$, while, with the addition of one proton, the drip-line in the F isotopic chain extends to at least $^{30}$F. This is unexpected, as naively one would expect $^{28}$O to be bound, as it is doubly magic when considering the conventional magic numbers. With $\chi$EFT it was shown that the 3N part of the interaction provides the necessary repulsive force, leading to the observed drip-line. As seen in figure 2.5, the NN only interaction [10] over binds in the $n$-rich nuclei, leading to a bound $^{28}$O. By introducing the 3N-interaction, a repulsive force arises, pushing the drip-line back to $N = 16$. The phenomenological effective interaction USDB [93] is in excellent agreement with the experimental data from the Atomic Mass Evaluation 2012 (AME12) [69], and it correctly predicts the drip-line to be at $N = 16$. The Coupled-Cluster approach [109] also predicts the correct position of the drip-line, although the heaviest nuclei are severely under-bound.

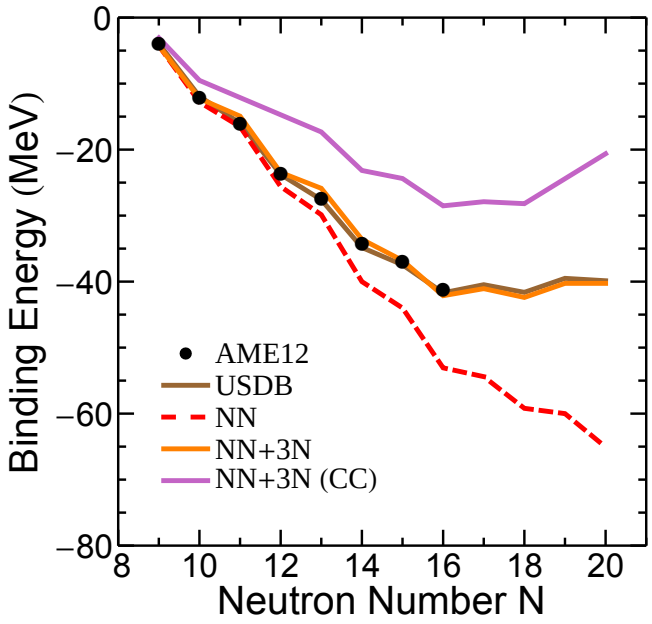


**Figure 2.5:** Oxygen binding energies relative to $^{16}$O calculated with USDB, NN + 3N shell model and CC interactions. NN and 3N + NN calculations from [10], and CC calculations from [109]. Experimental data is taken from AME12 [69].

## 2.4 Testing $\chi$EFT forces: The $N = 32, 34$ sub-shell closures

Much experimental and theoretical efforts have been spent trying to understand the properties near $N = 32$ and 34. It has been predicted that new magic numbers may appear here, thus leading to two new doubly magic nuclei: $^{52,54}$Ca.

There are several signatures of magicity that can be studied. One simple measure is the excitation energy of the first excited $2^+$ state. A high energy first excited $2^+$ state indicates a magic nucleus because of the cost in energy associated with constructing this state in magic nuclei. Moreover, this cost is especially high in doubly-magic nuclei. Due to the pairing mechanism in doubly-magic nuclei all pairs of nucleons are coupled to $J^\pi = 0^+$ states from which it is impossible to construct $J^\pi = 2^+$ states. The only way to construct these states is to break the nucleon pair, costing $\approx 1$ MeV in energy, and promoting one of these nucleons across the shell gap. The energy associated both with breaking the nucleon pair, and promoting a nucleon across the shell gap leads to large energies for the first $2^+$ state.

A second measure of magicity is the reduced transition probability B(E2), a quantity that measures the transition probability between the ground state and first excited $2^+$ state. The

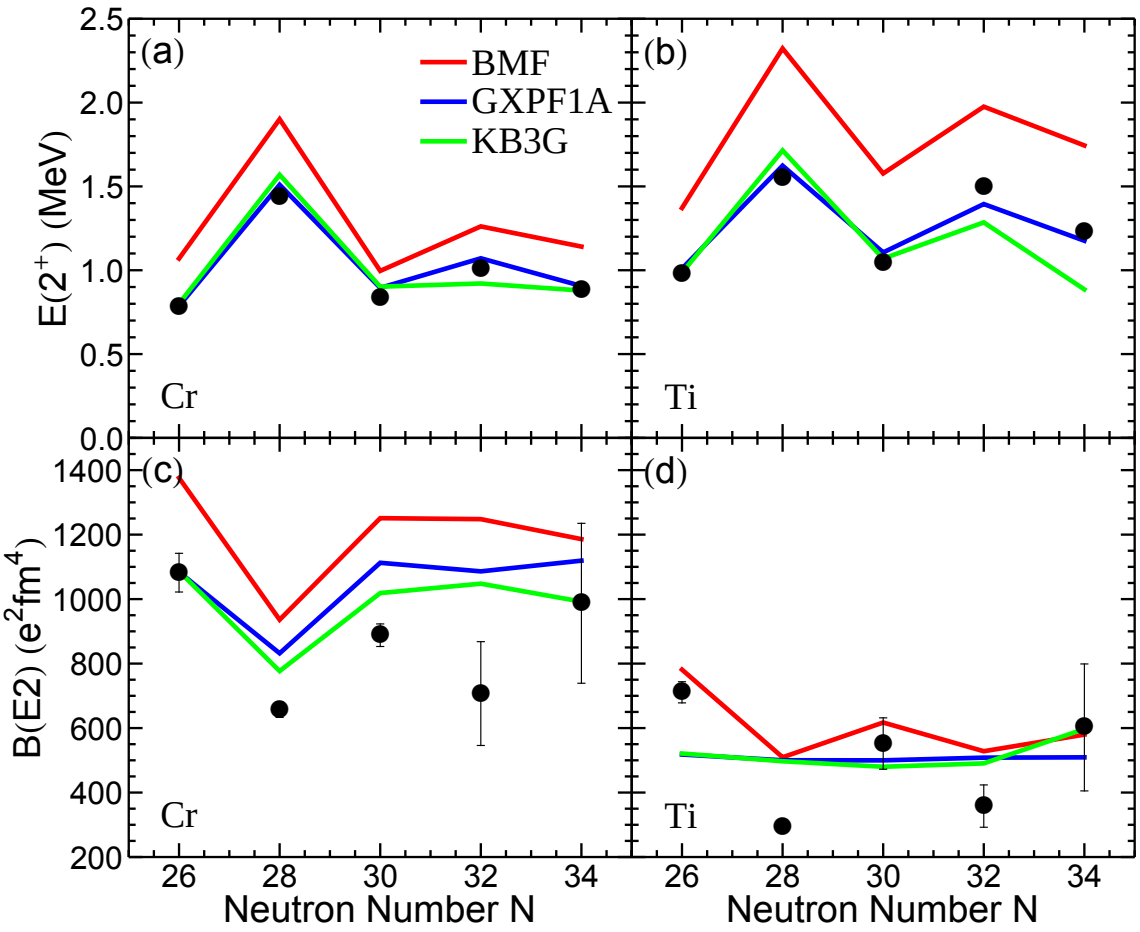


**Figure 2.6:** E($2^+$) and B(E2) values for Cr and Ti isotopic chains near $N = 32, 34$. E($2^+$) for the even Cr (a) and Ti (b) isotopes, and B(E2) values for Cr (c) and Ti (d) isotopes. Beyond-mean-field (BMF) calculations from [112]. Cr data are from [113] and [114], Ti data are from [115] and [114].

B(E2) is proportional to the electric quadrupole moment,

$$\mathrm{B(E2)} \propto \left|\left\langle 2^+ \middle| \hat{Q} \middle| 0^+ \right\rangle\right|^2, \tag{2.9}$$

where $\hat{Q}$ is the electric quadrupole operator. A small B(E2) is interpreted as being a near spherical nucleus, while a large B(E2) corresponds to a deformed nucleus. Thus, large B(E2) values should be found in collective nuclei that are mid-shell, while small B(E2) values will be found at magic nuclei [116].

We can now study the existing spectroscopic information in the nuclei around $^{52}$Ca. In figure 2.6 we show the experimental E($2^+$) and B(E2) values, along with theoretical calculations using GXPF1A, KBG3, and a beyond-mean field approach [112]. The GXPF1A and KB3G

predictions were calculated in the full $pf$-space on top of a $^{40}$Ca core, using the shell model code ANTOINE [117, 100, 99]. In figure 2.6 (a) and (b), there is a clear increase in the E(2+) energy at both $N = 28$ and 32, as compared to the surrounding nuclei. The $N = 32$ gap is reduced in the Cr isotopes as compared to the Ti chain, as evidenced by the decrease in the E(2+). There is evidence that $N = 34$ is magic in $^{56}$Ti, however, in $^{58}$Cr the value returns to the non-magic value. There is a corresponding decrease in the experimental B(E2) values at $N = 28$ and 32 in both chain, but no such dip is seen at $N = 34$. From this we can conclude that $N = 32$ is a good magic number, while $N = 34$ may be magic in Ti.

The beyond-mean-field approach reproduces the trend in the E($2^+$) energies, however, the values are systematically too high. The GXPF1 and KB3G calculations do a much better job in predicting the absolute values of the excitation energies, the GXPF1 calculation reproduces the increase at $N = 32$, while the KB3G calculation does not. For the B(E2) values, the GXPF1A and KB3G both give very similar results. In the Cr chain, the experimental B(E2)'s are quite well reproduced, however, the drop at $N = 32$ is not. In the Ti chain, none of the staggering in the B(E2)'s is reproduced. This lack of staggering is due to the choice of the effective charge of the proton and neutron [70]. The effective charge is not the bare charge of the nucleon since the effect of the core nucleons has been absorbed by the valence nucleons during the process of defining the effective interaction. If the effective charge is changed, a staggering becomes apparent, however, it still does not completely reproduce experiment.

All three theoretical models are mostly able to reproduce the measured results in the Cr and Ti chains. As seen from both data and theory, it is evident that there is a sub-shell closure at $N = 32$, given the above introduced signatures, and a weak sub-shell at $N = 34$ may exist in Ti. A true test would be to examine the trends in the calcium chain. Verification of these predictions thus far have not been possible due to the difficulty in performing experiments in this region, resulting in an absence of data.

In figure 2.7 we plot the E($2^+$) values for the Ca isotopic chain. Again, all theories agree quite well with experiment, however, they start to deviate from each other at $N = 34$. In figure 2.7 (b) we also show the results based on $\chi$EFT interactions [120, 119]. The NN-only interaction fails at reproducing the data, even to the point of missing the $N = 28$ shell closure in $^{48}$Ca. The calculations including 3N-forces achieve much better agreement with experiment, not only reproducing the $N = 28$ magic number, but also in predicting the excitation value at $N = 34$. The E($2^+$) was recently measured at the RIKEN facility [118], confirming that a sub-shell exists at $N = 34$.

Another method to determine if $N = 32$ and 34 are closed shells, or sub-shells, is through mass measurements, specifically, by examining the $S_{2n}$ values. Figure 2.8 presents the mea-

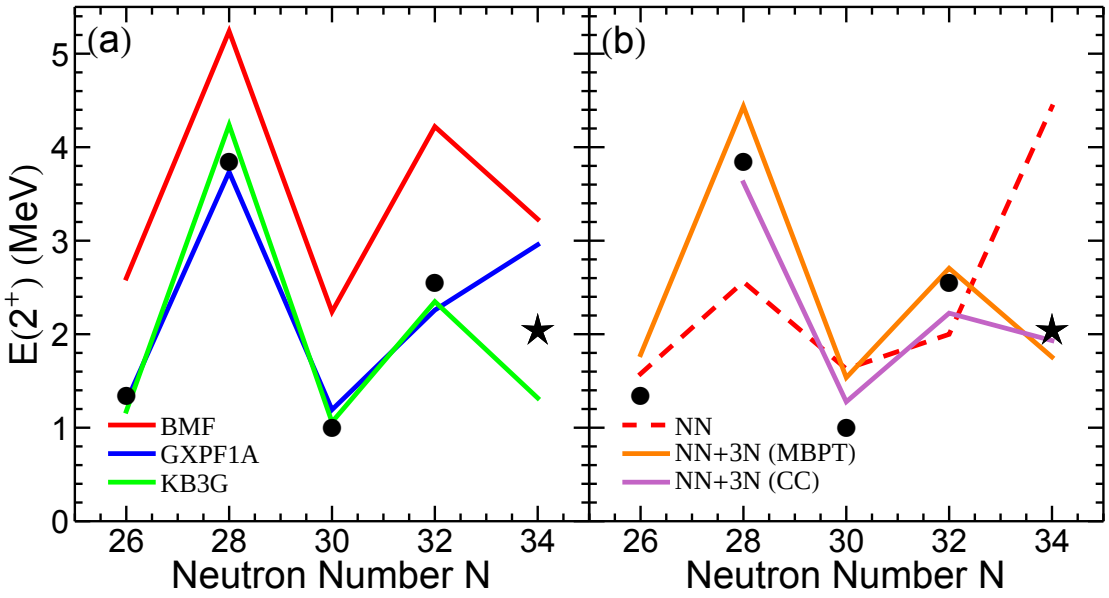


**Figure 2.7:** E($2^+$) values in the Ca isotopic chain. Both the GXPF1A and KB3G calculations agree where data is known, but they disagree in their predictions at $N = 34$. The star (★) is the recently measured value by Steppenbeck *et al.* [118], and is considered to be a confirmation of a sub-shell closure at $N = 34$, the other experimental data are from [114]. the BMF calculations from [112], the NN and NN + 3N calculations are from [119], and the CC calculations are from [120].

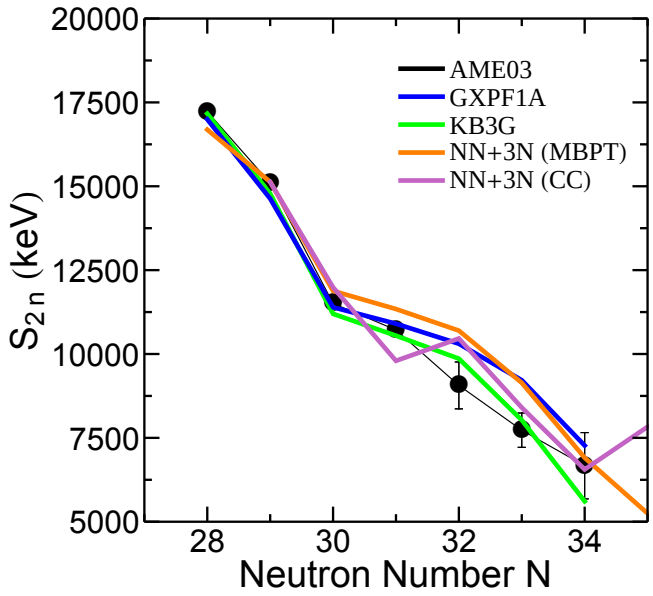


**Figure 2.8:** Experimental $S_{2n}$'s, taken from AME11 [121], for the calcium isotopes, as compared to theory. Values for MBPT and CC calculations are taken from [59].

sured values from the Atomic Mass Evaluation 2011 (AME11) [121]. The GXPF1A and MBPT [119] results agree quite well with the data to $N = 31$. The CC [120] result also agrees quite well with the GXPF1A and MBPT calculations, however, there is a large dip in the $S_{2n}$ value at $N = 31$. The KB3G calculation agrees with the both data and the other calculations until $N = 30$, where the KB3G values become systematically lower than the other calculations.

## 2.5 Testing $\chi$EFT forces: The isobaric multiplet mass equation

The proton and neutron are both spin-1/2 particles and are nearly degenerate in mass. There is, however, a striking difference between the two particles, which is their charge. Due to these similarities, it is possible to consider the proton and neutron as members of a doublet in the abstract isospin $T$ space, where the proton has a $z$-projection of $T_z = -1/2$ and the neutron has a $z$-projection of $T_z = 1/2$. This concept was originally proposed by Heisenberg [122]. Isospin is a good quantum number, thus for any nucleus the $z$-projection of the isospin of the ground-state is given by

$$T_z = \frac{N-Z}{2}. \tag{2.10}$$

For a given collection of protons and neutrons, there can be isospin configurations between

$$\left|\frac{N-Z}{2}\right| \leq T \leq \frac{N+Z}{2}. \tag{2.11}$$

Thus, states with the same isospin in different isobaric nuclides form an isospin multiplet.

If the nuclear force is isospin independent, then the binding energy of states in an isospin multiplet should be degenerate. Furthermore, the excited states of such nuclei should be similar. As an example, figure 2.9 shows the $A = 9$ multiplets. Note the similarity of energy levels in $^{9}$Be and $^{9}$B, and between $^{9}$Li and $^{9}$C. A special case of this are the $T = 1/2$ and 1 "mirror nuclei" (see [124, 125, 126] for examples), where two nuclides have the same mass number but the number of protons and neutron are swapped. These nuclides sit on either side of the $N = Z$ line. Because the ground states of these nuclei have the same $T$, but opposite $T_z$, they should have very similar structure in their excited states, as can be seen in figure 2.10 in the ground state rotational band in $^{50}$Fe and $^{50}$Cr. The similarity of the two spectra demonstrates that isospin is a symmetry of the nuclear interaction; however, the small differences point to an isospin non-conserving interaction.

Isospin is an approximate symmetry, manifesting itself in the mass difference between the

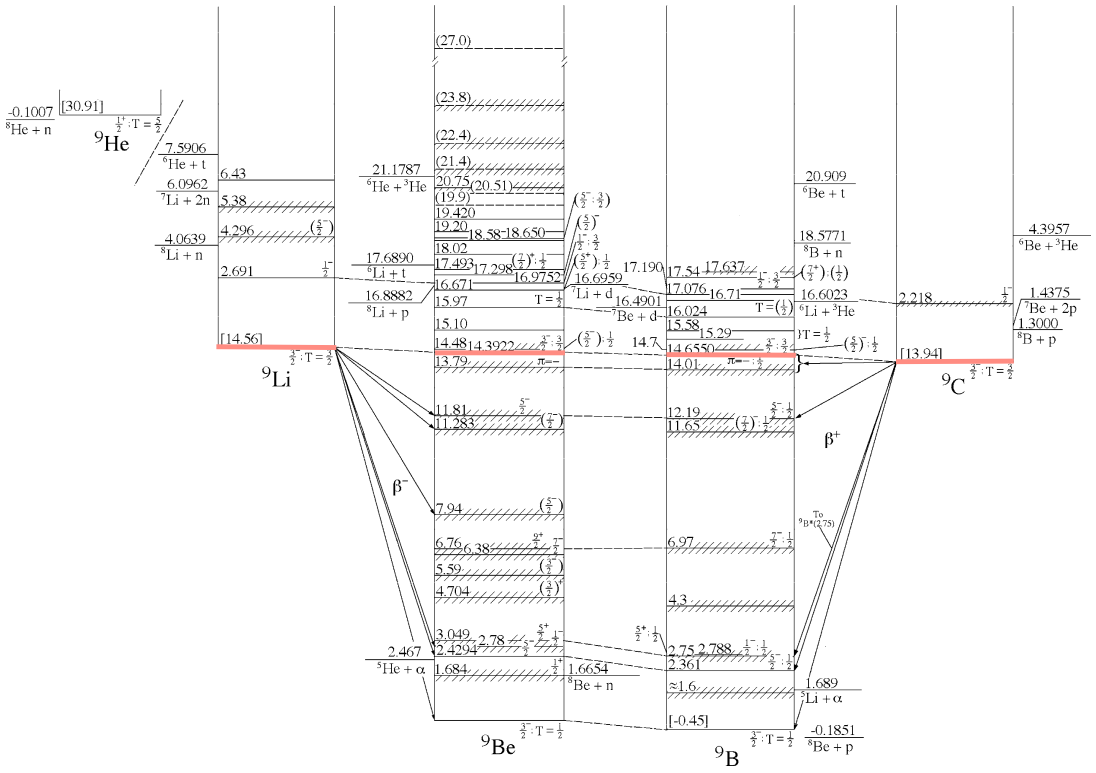


**Figure 2.9:** Measured energy levels for the $A = 9$ systems. The ground-state energy levels have been shifted so that the isobaric multiplets lie at approximately the same energy. Isobaric multiplets are connected with dashed lines. The $J = 5/2^+$, $T = 3/2$ ground-state multiplet has been highlighted in red. Figure reproduced with permission from [123].

proton and neutron. The isospin symmetry is also broken by the isospin-dependent part of the nuclear Hamiltonian and the Coulomb interaction. These interactions break the symmetry and lift the degeneracy of the isospin multiplet, but the largest contribution comes from the Coulomb interaction. The Coulomb interaction in isospin space is

$$V_{\text{coul}} = \sum_{i<j} \frac{Q_i Q_j}{|r_i - r_j|} = e^2 \sum_{i<j} \left(\frac{1}{2} - t_z(i)\right)\left(\frac{1}{2} - t_z(j)\right) \frac{1}{|\vec{r}_i - \vec{r}_j|}, \tag{2.12}$$

where $Q$ is the charge operator, $e$ is the electron charge, and $t_z$ is the isospin operator. This can then be expanded as a sum of isoscalar, isovector, and isotensor operators

$$V_{\text{coul}}^{(0)} = e^2 \sum_{i<j} \left(\frac{1}{4} + \frac{1}{3}\vec{t}(i)\cdot\vec{t}(j)\right) \frac{1}{|\vec{r}_i - \vec{r}_j|},$$

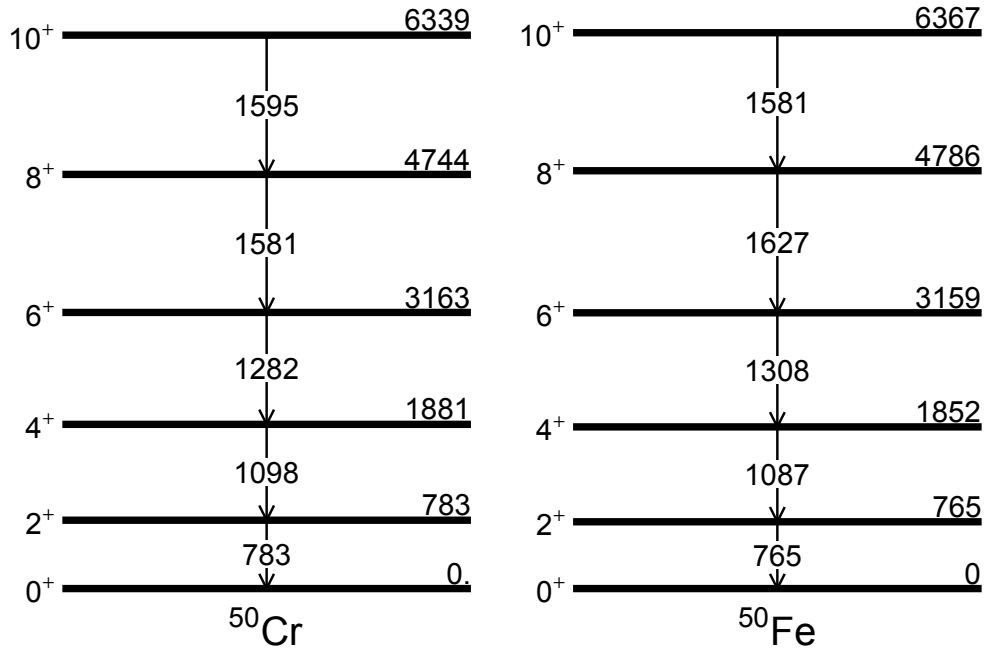


**Figure 2.10:** The level structure of the ground-state rotational bands in the $T = 1$ nuclei $^{50}$Fe and $^{50}$Cr. The arrows indicate a transition between the connected states, with the transition energy listed in keV. The left labels are the $J^{\pi}$ of the state, the right label are the excitation energy in keV of the state. Data from [124].

$$V_{\text{coul}}^{(1)} = -\frac{e^2}{2}\sum_{i<j}\left(t_z(i)+t_z(j)\right)\frac{1}{\left|\vec{r}_i-\vec{r}_j\right|},$$

and

$$V_{\text{coul}}^{(2)} = e^2\sum_{i<j}\left(t_z(i)t_z(j)-\frac{1}{3}\vec{t}(i)\cdot\vec{t}(j)\right)\frac{1}{\left|\vec{r}_i-\vec{r}_j\right|},$$

where $\vec{t}$ is the isospin operator. The operator $V_{\text{coul}}^{(0)}$ does not depend on the operator $T_z$, while $V_{\text{coul}}^{(1)}$ and $V_{\text{coul}}^{(2)}$ depends on the operators $T_z$ and $T_z^2$, respectively.

If we treat the Coulomb interaction as a perturbation, the first-order energy shift is given by the expectation value of the Coulomb interaction

$$E_{\text{coul}} = \langle\alpha, T, T_z|\, V_{\text{coul}}\,|\alpha, T, T_z\rangle \tag{2.13}$$

where $\alpha$ represents all of the good quantum numbers that do not depend on the isospin. Applying the Wigner-Eckart theorem [127], it is possible to extract the isospin dependence of the

Coulomb energy shift,

$$E_{\text{coul}} = \langle \alpha, T, T_z | \sum_{q=0,1,2} V_{\text{coul}}^{(q)} | \alpha, T, T_z \rangle \tag{2.14}$$

$$= \sum_q (-1)^{T-T_z} \begin{pmatrix} T & q & T \\ -T_z & 0 & T_z \end{pmatrix} \langle \alpha, T, T_z | | V_{\text{coul}}^{(q)} | | \alpha, T, T_z \rangle \tag{2.15}$$

$$= E_{\text{coul}}^{(0)}(\alpha, T) + E_{\text{coul}}^{(1)}(\alpha, T) T_z + E_{\text{coul}}^{(2)}(\alpha, T)(3T_z^2 - T(T+1)). \tag{2.16}$$

where the Coulomb energy shifts are

$$E_{\text{coul}}^{(0)} = \frac{1}{\sqrt{2T+1}} \langle \alpha, T | | V_{\text{coul}}^{(0)} | | \alpha, T \rangle$$

$$E_{\text{coul}}^{(1)} = \frac{1}{\sqrt{T(2T+1)(T+1)}} \langle \alpha, T | | V_{\text{coul}}^{(1)} | | \alpha, T \rangle$$

$$E_{\text{coul}}^{(2)} = \frac{1}{\sqrt{T(2T+3)(2T+1)(T+1)(2T-1)}} \langle \alpha, T | | V_{\text{coul}}^{(2)} | | \alpha, T \rangle$$

The double-bar elements are reduced matrix elements, indicating that they are independent of $T_z$. The $T_z$ dependence can be factored out, leading to a quadratic relationship [128]

$$ME(A, T_z) = a(\alpha, T) + b(\alpha, T) T_z + c(\alpha, T) T_z^2. \tag{2.17}$$

This equation is called the Isobaric Multiplet Mass Equation (IMME), first introduced by E. Wigner. The $a$ term is the mass excess of the $T_z = 0$ for integer $T$ multiplet. In the cases of half-integer $T$, the $a$ term is related to the difference $E_{\text{coul}}^{(0)} - T(T+1)E_{\text{coul}}^{(2)}$. The $b$ term depends on the expectation value of $V_{\text{coul}}^{(1)}$ and gives the largest contribution to the IMME. The $c$ term depends on the expectation value of $V_{\text{coul}}^{(2)}$ and describes the interaction between states that differ by two units of isospin.

An intuitive understanding of the $b$ and $c$ terms can be gained by considering the energy of a uniformly charged sphere with radius $R = r_0 A^{1/3}$

$$E_{\text{coul}} = \frac{3e^2}{5R} Z(Z-1) \tag{2.18}$$

$$= \frac{3e^2}{5r_0 A^{1/3}} \left( \frac{A}{4}(A-2) + (1-A) T_z + T_z^2 \right) \tag{2.19}$$

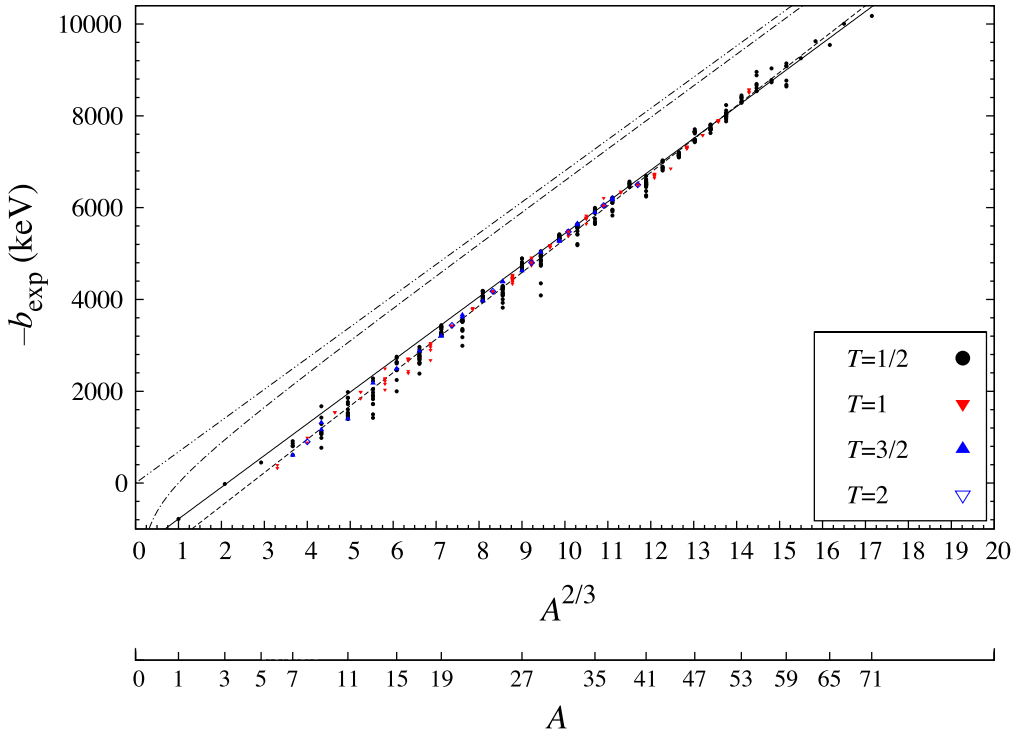


**Figure 2.11:** $b$-coefficients of the IMME (eq. 2.17) as a function of $A^{2/3}$ for the $T = 1/2, 1, 3/2, 2$ multiplets. The solid line is a weighted fit with $b = -690.98(\pm 89)A^{2/3} + 1473.02(\pm 93)$ (keV), the dashed line is an unweighted fit with $b = -726.64A^{2/3} + 1952.7$ (keV), the dash-dotted line is $b = -\frac{3e^2(A-1)}{5r_0A^{1/3}}$, and the double-dot-dashed line is $b = -\frac{3e^2}{5r_0}A^{2/3}$. Figure reproduced with permission from [129].

where we have used $Z = A/2 - T_z$. The $b$ and $c$ coefficients are then

$$b = -\frac{3e^3}{5r_0}\frac{(A-1)}{A^{1/3}}, c = \frac{3e^2}{5r_0}\frac{1}{A^{1/3}}. \tag{2.20}$$

From these simple estimates, the $b$ term is by far the leading contribution to the IMME, as generally $A >> T_z$ or $T_z^2$. The general scaling of $b$ by $A^{2/3}$ and $c$ by $A^{-1/3}$ can be seen in the trend of the fitted $b$ and $c$ terms [129]; however this simple picture of the Coulomb energy shift does not reproduce all of the observed features. Figure 2.11 shows the behavior of the $b$-coefficients with respect to $A^{2/3}$. The simple $b$ term derived in equation 2.20 reproduces the overall slope seen in the experimentally determined $b$ values, however, there seems to be an overall offset of $\approx$ 1500 keV.

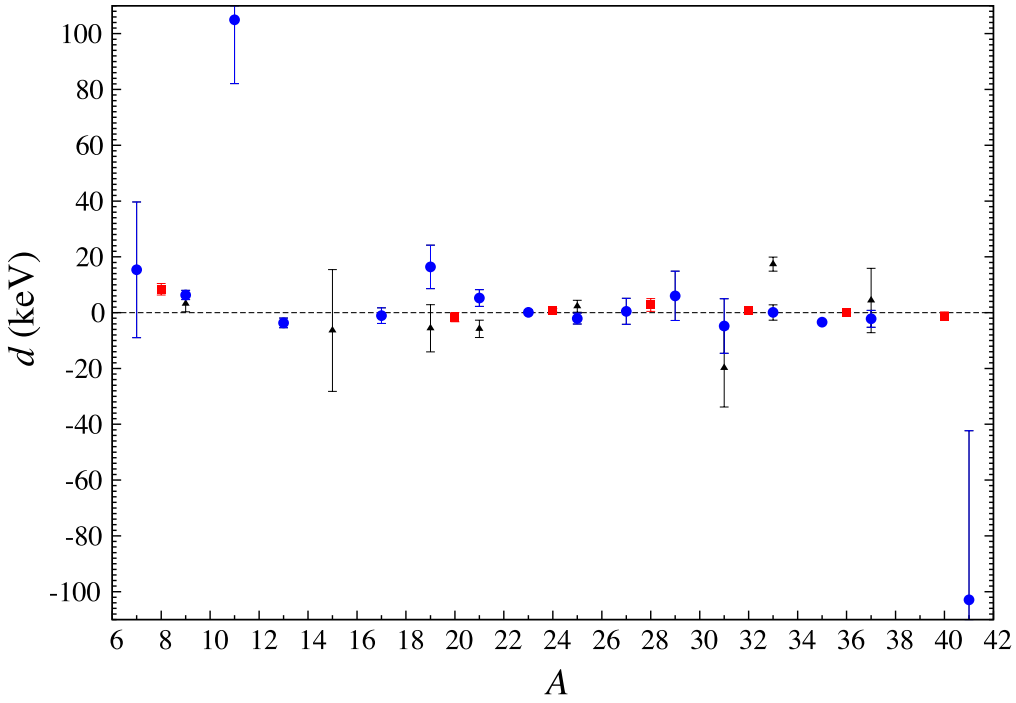


**Figure 2.12:** Experimental $d$ coefficients from the cubic form of the IMME, for all quartets and quintets. The blue dots and red squares are the $d$ coefficients of the lowest-lying quartets and quintets, while the black triangles are the $d$ coefficients of higher lying quartets. Figure reproduced with permission from [129].

This offset of $\approx 1500$ keV can be corrected for by including the difference in mass between the proton and neutron. Nuclei with higher $T_z$ should be heavier than nuclei with lower $T_z$. The $b$-term now becomes

$$b = \Delta_{nH} - \frac{3e^3}{5r_0}\frac{(A-1)}{A^{1/3}}. \tag{2.21}$$

The mass difference $\Delta_{nH} = 782$ keV, which is the mass difference between the neutron and hydrogen atom, corresponds to half of the difference needed to correct the shift in binding energies.

It may be that the quadratic form of the IMME can not explain the measured mass excesses, and quartic $d$ and quintic $e$ terms may be required. For example, large deviations from the IMME have been observed in the $A = 9$ $J^\pi = 3/2^+$ and $A = 33$ and 35 $J^\pi = 3/2^+$ quartets [130, 131, 129] and in the $A = 8$ and 32 quintets [132, 133, 134]. These higher order terms could arise from isospin mixing between nearby states, second-order Coulomb effects [129], or missing 3N interacitons. It is precisely these effects that provide a stringent test of theory.

In the extended IMME, where $d$ and $e$ terms are considered, the $d$ and $e$ terms may be directly determined for IMME quartets and quintets, respectively. In an isospin quartet, the $d$ term is given by

$$d = \frac{1}{6}(-ME(T_z = -3/2) + 3ME(T_z = -1/2) - 3ME(T_z = 1/2) + ME(T_z = 3/2)) \tag{2.22}$$

and the $d$ and $e$ coefficients in an isospin quintet are given by

$$d = \frac{1}{12}(-ME(T_z = -2) + 2ME(T_z = -1) - 2ME(T_z = 1) + ME(T_z = 2)), \tag{2.23}$$

$$e = \frac{1}{24}(ME(T_z = -2) - 4ME(T_z = -1) + 6ME(T_z = 0) - 4ME(T_z = 1) + ME(T_z = 2)). \tag{2.24}$$

The uncertainty of these terms can be found by a simple propagation of errors. In general, the experimental $d$ terms are consistent with zero, except in a few cases as mentioned above. Figure 2.12 shows the experimental $d$ terms for all known isospin quartets and quintets. It is remarkable that, except in a handful of cases, the experimental $d$ terms are all close to zero.

### 2.5.1 Two-level mixing and the $d$ term

The primary cause of the $d$ term is from two-level mixing of nearby states with the same spin but different isospin. This causes the perturbed wave functions to have a mixed isospin character; thus the state no longer belong to the isobaric multiplet. As an example, we take two nearly degenerate states with a matrix element $V$ connecting them [135]. The good wave functions can then be found by diagonalizing the matrix

$$\begin{pmatrix} E & V \\ V & E+\Delta \end{pmatrix} \tag{2.25}$$

where $E$ is the energy of one state and $\Delta$ is the difference in energy. The eigenvalues are

$$\lambda = E + \frac{\Delta}{2} \pm \frac{1}{2}\sqrt{\Delta^2 + 4V^2}. \tag{2.26}$$

The resulting energy shift is quite complicated because of interference between the Coulomb,

isovector, and isotensor parts of the isospin non-conserving interactions. Such a mechanism has been employed in the $A = 9$ isospin quartet [130], and it was shown to be the main driver for the observed $d$-term.

### 2.5.2 Testing the IMME

Historically, the quadratic behaviour of the IMME has been confirmed in a number of experiments. However, much of the data – ground state and excitation energies – tend to have quite large uncertainties, limiting the precision of the investigation of isospin-symmetry-breaking effects in nuclei. For example, understanding these isospin-symmetry-breaking effects is important for calculations of the isospin-symmetry-breaking correction $\delta_C$ in super-allowed Fermi beta decays [136]. It has only been in recent years, with the advent of Penning trap mass spectrometers, that some of the IMME multiplets have been found to deviate from the quadratic form of the IMME.

In order to test the predictions of both effective interactions and $\chi$EFT interactions we have measured the masses of $^{20,21}$Mg, which are the most proton-rich members of the $A = 20$, $T = 2$ isospin quintet and the $A = 21$, $T = 3/2$ isospin quartet. The test of the $\chi$EFT based interaction is quite interesting as this is the first time this interaction will be tested with both active protons and neutrons in the valence space.

# Chapter 3

# Experimental setup

TRIUMF's Ion Trap for Atomic and Nuclear science (TITAN) is located in the Isotope Separator Accelerator (ISAC) [137] facility at TRIUMF in Vancouver, British Columbia. TITAN currently consists of three ion traps: (1) a Radio-Frequency Quadrupole (RFQ) cooler and buncher, used to prepare the beam from ISAC, (2) an Electron Beam Ion Trap (EBIT), used to charge breed the beam to increase the achievable precision of a mass measurement, and (3) a Measurement Penning Trap (MPET), used to perform high precision mass measurements on short-lived ($t_{1/2} \lessapprox 100\,\text{ms}$) nuclides. A schematic outline of the TITAN system is shown in figure 3.1. From its first operation in 2007, TITAN has focussed on measuring the masses of halo nuclei. For example, TITAN has measured the masses of the halo nuclei $^{6,8}$He [138], $^{11}$Li [67] and $^{11}$Be [139]. Beryllium-12 [140] is an interesting case as the halo state is not the ground state, but instead is an excited state [141]. Since then, TITAN has conducted several measurement campaigns of medium mass nuclei to investigate such phenomena as the Island of Inversion [142, 143], the presence of deformation in potential r-process nuclei in the neutron-rich Rb and Sr isotopic chains [144, 145], measuring the $^{71}$Ge-$^{71}$Ga $Q$-value to calibrate the SAGE and GALLEX neutrino detectors [146], and measuring the mass of $^{74}$Rb [147] to test the unitarity of the CKM matrix.

Two properties distinguish TITAN from other on-line Penning Trap Mass Spectrometry (PTMS) systems: The ability to charge breed exotic beams leads to increased precision and resolving power. The unique combination of production source and MPET injection optics permit measurements of the shortest-lived nuclides at TITAN. These qualities are exemplified by the mass measurement of $^{11}$Li, whose half-life of 8.8 ms, is the shortest lived nuclide to have its mass measured in a Penning trap.

The precision of a PTMS measurement is inversely proportional to the charge state of the

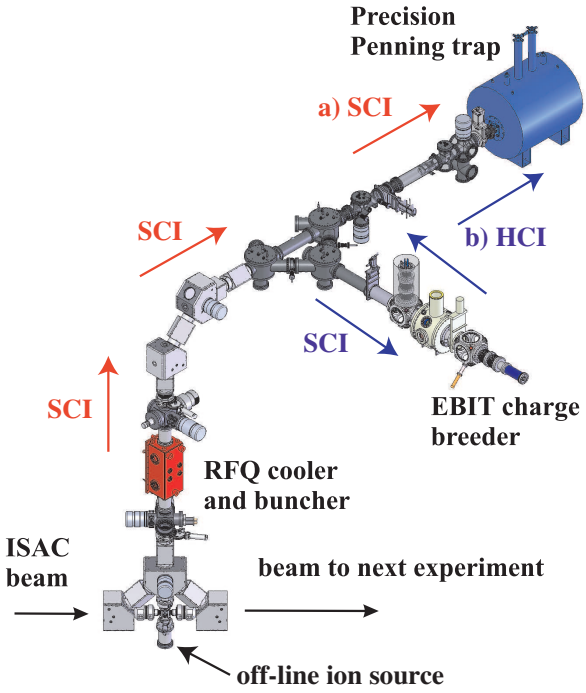


**Figure 3.1:** Rendering of TITAN. Beam is delivered from ISAC or the TITAN ion source to the RFQ. Singly charged ions (SCI) are sent either to EBIT, for charge breeding and decay spectroscopy, or to MPET. Highly charged ions (HCI) can be extracted from EBIT and sent to MPET for precision mass measurements.

ion [148]

$$\frac{\delta m}{m} \propto \frac{m}{qBT_{RF}\sqrt{N}} \tag{3.1}$$

where $q$ is the charge state of the ion, $B$ is the magnetic field strength of the trap, $T_{RF}$ is the excitation time of the ion, and $N$ is the number of detected ions. Several factors conspire to limit the achievable precision in on-line mass measurements: (1) the magnetic field strength $B$ is limited—large homogeneous magnetic fields represent a technological challenge, (2) the excitation time $T_{RF}$ is limited by the half-life of the nuclide, and (3) $N$ is fixed both by the yield of the ion of interest and the limited access to online beam time at rare isotope beam facilities. These limitations can be overcome by charge breeding, the process of removing electrons from the trapped beam through impact ionization with the electron beam, in the EBIT. An increase in the charge state $q$ leads to an increase in the achievable precision, and also greatly shortens the measurements time ($\approx T_{RF}N$) to reach a given precision. For example, in 22 hours the TITAN measurement of $^{74}$Rb in a charge state $q = 8^+$ [147] achieved a precision comparable to that of the ISOLTRAP system [149], which needed more than 150 hours of data collection

using singly charged ions [150].

## 3.1 Beam production

Currently there are two primary methods for producing exotic beams: the fragmentation of heavy ion beams on a thin target, called in-flight fragmentation [151, 152], and the spallation and fragmentation of a thick, high-temperature target by a light beam, called Isotope Separation on-line (ISOL) [152]. In-flight fragmentation has the ability to produce any beam, as it is essentially free of chemistry effects, because the high-energy secondary beam cannot chemically react with the target material. While wide in its reach, in-flight fragmentation can suffer from low yields of the nuclide of interest, especially for nuclei far from the valley of stability. On the other hand, ISOL facilities can have very high yields, even for beams far from stability. Nevertheless, these high yields quite often suffer losses due to in-target chemistry effects/reactions (such as binding to the lattice of the target material), because the reaction products are produced nearly at rest with respect to the target, and must diffuse to the target surface to be ionized and extracted. Several other niche production methods are in use, notably the CARIBU facility [153] at Argonne National Laboratory, where the spontaneous fission products from the decay of $^{252}$Cf are caught in a gas cell, and the ion guide isotope separator on-line (IGISOL) facility [154] at JFYL in Jyväskylä, Finland, in which fission products from the reaction of protons on U or Th targets are caught in a gas cell. At both CARIBU and IGISOL, the produced beam does not need to diffuse out of a thick ISOL target, greatly reducing in-target losses due to chemistry.

Stopped beam experiments at fragmentation facilities can also be affected by chemistry. The high-energy beams are stopped in a gas cell, usually filled with a He buffer gas to slow the beam through collisions. The stopping beam creates a harsh environment, with large amounts of space charge, allowing the beam and buffer gas impurities to form exotic molecules. Many times these molecules are close in mass to the beam of interest, which can be a problem for Penning-trap-based experiments due to contamination effects.

## 3.2 ISAC

At TRIUMF beams are produced by bombarding a thick production target with a high-current, high-energy (up to 100 $\mu$A at 480 MeV) proton beam. A schematic of the ISAC target and extraction front end are shown in figure 3.2. The target material is composed of many foils, stacked along the beam axis, helping to speed the diffusion of the fragments to the surface of the target material. To further speed diffusion of the fragments, the tube housing the target

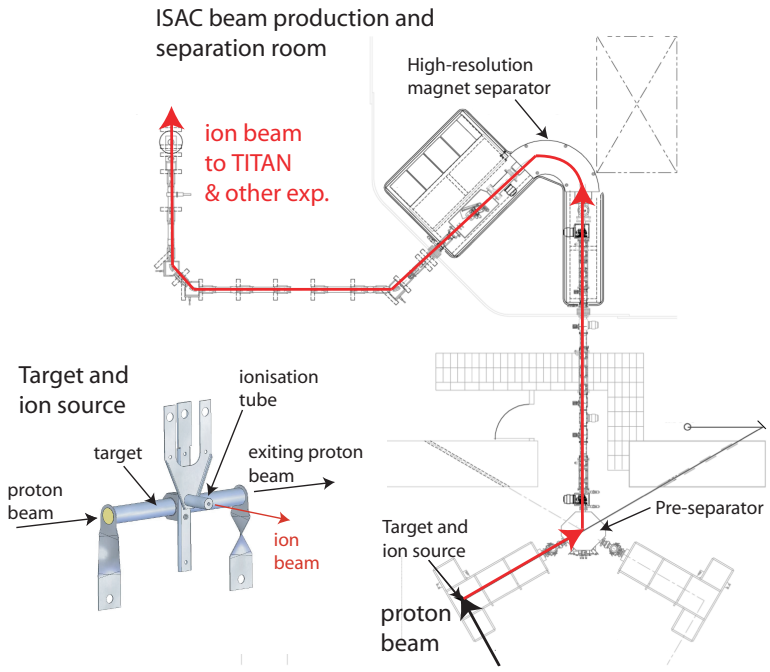


**Figure 3.2:** Overview of the ISAC target and dipole separation magnet. Figure from [155].

is ohmically heated to $\approx 2000\,^{\circ}$C. It is during this diffusion that chemistry can occur: the synthesized radio-nuclides may chemically bind to the target material and will not be released, or the ionization potential of the desired element is not suitable to the ion source, resulting in no ionized beam. The produced rare isotopes are released from the target's surface and travel in a random walk to the target exit. Here a heated tube that is coated with a high-work-function material, typically rhenium, surface ionizes the beam, allowing species with ionization potentials below approximately 6 eV to be ionized [156]. Atoms are surface ionized by being desorbed from a hot surface, and in the process are spontaneously ionized. Many species, such as refractory elements and gases, can not be readily ionized in such a scheme. For example, phosphorous is a very reactive element and will readily react with the target material, and be bound to the target. Gases, such as the halogens and noble gases, have very high ionization potentials so a special ionizer, for example a forced electron beam ion arc discharge [157], must be used to ionize the beam. Elements, such as the alkaline earth metals and the transition metals, with ionization energies between 6-9 eV are not efficiently surface ionized, instead, they can be laser ionized, as discussed in section 3.2.1.

Once the beam is ionized and extracted from the target, it is electrostatically accelerated to energies between $10-60$ keV. The desired isotope is then selected by passing the beam through

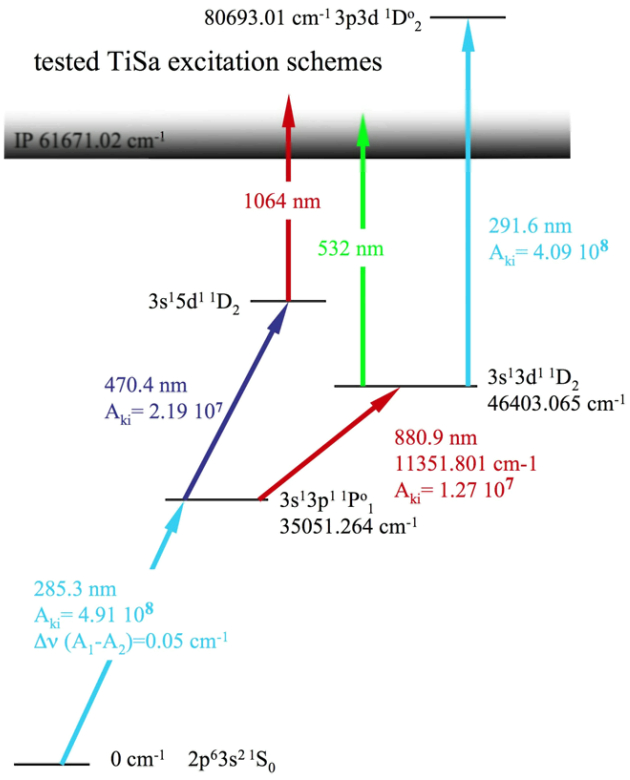


**Figure 3.3:** Laser ionization schemes for magnesium ($Z = 12$). Only the states relevant to the ionization scheme are shown. The rightmost scheme is the most efficient. Figure reproduced with permission from [158].

a dipole magnet, which separates the beam based on $m/q$. The dipole separator has a resolving power of $m/\Delta m \approx 3000$, which is sometimes sufficient to select the element of interest from the contaminants; however, often this resolving power is insufficient for providing a pure beam. These background contaminants can render many experiments impossible due to extremely bad signal-to-contaminant ratios. A new ion source technique, discussed in section 3.2.1, has been developed to confront these issues.

### 3.2.1 TRIUMF resonance ionization laser ion source and the ion-guide laser ion source

For certain elements that may not be efficiently surface ionized, it is possible to use a Resonance Ionization Laser Ion Source (RILIS), by inducing transitions to auto-ionizing states in the element of interest, provided that a suitable ionization scheme is known. By using step-wise excitation to the auto-ionizing state, element specific ionization is achieved. Since the laser

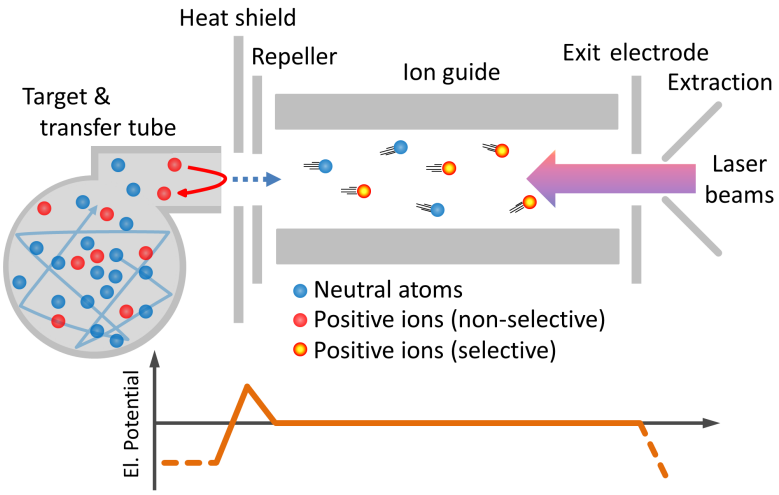


**Figure 3.4:** Schematic of the ISAC target with IG-LIS. Surface ionized species are stopped by the repeller, while neutral atoms can drift into the RFQ volume. Resonant laser ionization ionizes only the element of interest, allowing dramatic increases in beam purity. Figure from [162].

ionization is element specific, while the mass separator selects on the mass number $A$, their combination represents a powerful approach to producing isotopically pure beams. As an example, the demonstrated ionization schemes for Mg are shown in figure 3.3. At ISAC the TRIUMF's Resonance Ionization Laser Ion Source (TRILIS) source uses three frequency tunable titanium:sapphire (Ti:Sa) lasers that are pumped by a frequency doubled Nd:YAG laser [158]. The Ti:Sa laser can be frequency doubled, tripled and quadrupled to nearly cover the wavelength range $200 - 1000$ nm [158, 156]. Once the most efficient ionization scheme has been found, the total efficiency of the laser ionization system most strongly depends on the available laser power for a given wavelength. At TRILIS for the ionization of Mg, the first ionization step (285.3 nm) is nearly saturated, while the second ionization step (880.9 nm) is fully saturated [159]. Increasing the laser power in either of these transitions would have a small effect on the overall ionization rate. However, the final ionization step (291.6 nm) is not saturated, and can benefit from any increase in laser power. The RILIS technique has been successively used at many ISOL facilities, such as ISOLDE [160], IGISOL [161], and ISAC [158].

In some cases the number of surface-ionized contaminants still overwhelms the RILIS-produced beam. To overcome this, a new ion source has been developed at TRIUMF, the Ion Guide Laser Ion Source (IG-LIS) [159], which is a variation of the originally proposed laser ion source trap (LIST)[163, 164]. In both cases, a repeller electrode is located at the exit of the target, preventing surface-ionized species from leaving the target volume, allowing only neutral species to drift into an ion-guide volume. The neutral atoms are then exposed to laser light

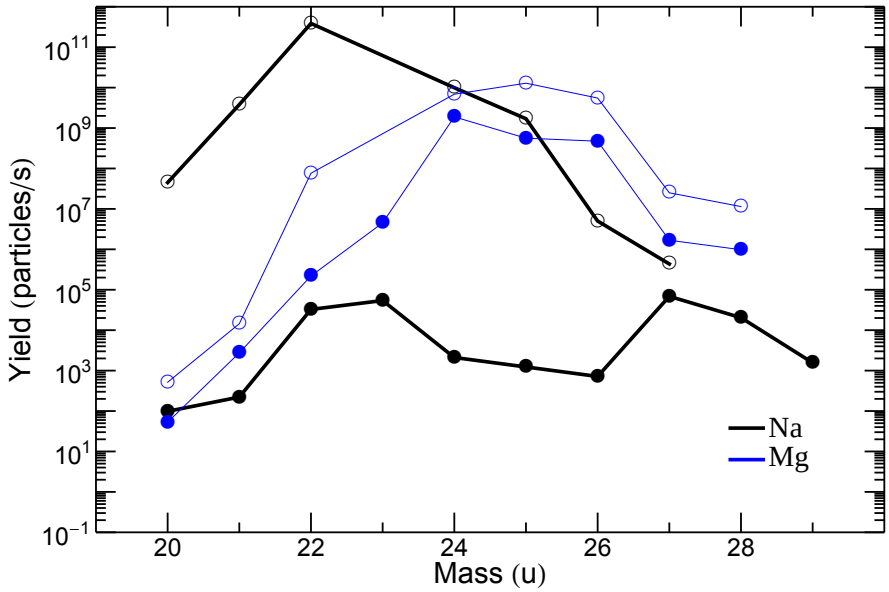


**Figure 3.5:** IG-LIS yields measured during the $^{20,21}$Mg experiment. Open circles are yields measured with a previous surface ion-source target, filled circles are the yields measured with IG-LIS. The Na yields are reduced by a factor of $\approx 10^6$, while the Mg yields are reduced by $\approx 10$. Data from [159].

which provides the element specific ionization, suppressing the background contaminants by many orders of magnitude. The LIST source uses an RFQ buncher to bunch the laser-ionized beam coming from the target, creating an ion bunch with well defined beam properties. Beam bunching also results in more brilliant beams for reaction experiments. By synchronizing the data acquisition to the extraction pulse, these reaction experiments can reduce backgrounds coming from any "leaky" beam escaping the trap. The IG-LIS source does not trap the beam longitudinally, instead the RFQ is used as an ion-guide to radially confine and guide the beam to the extraction electrode. A schematic of IG-LIS is shown in figure 3.4. During the present $^{20}$Mg experiment, IG-LIS improved the signal-to-contaminant ratio by more than a factor of $10^4$. Figure 3.5 summarizes the IG-LIS yield measurements for the laser-ionized species magnesium, and the surface-ionized species sodium. These species provided an excellent test of IG-LIS's ion suppression capabilities. On the proton-rich side of stability, the alkali metal sodium is closer to stability than magnesium, meaning the sodium will be produced in much larger quantities than magnesium. As seen in figure 3.5, the sodium yields could be suppressed by up to 6 orders of magnitude. IG-LIS also reduces the magnesium yield by approximately one order of magnitude due to both shorter ion-laser interaction times in the short IG-LIS volume and the suppression of any surface ionization of the beam of interest; however, for many

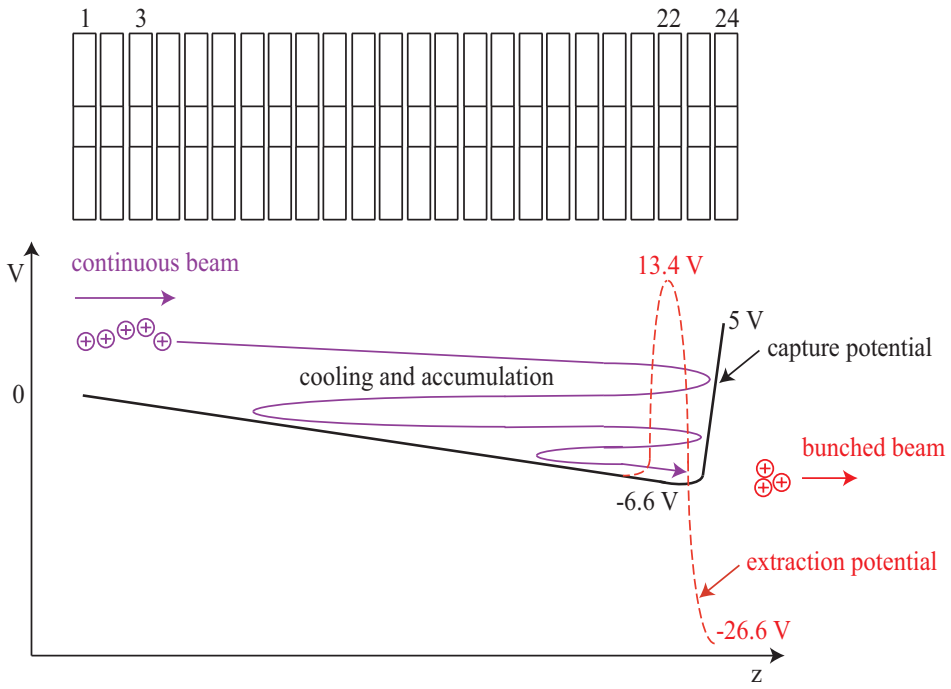


**Figure 3.6:** (top) Axial segmentation allows for a drag and trapping field to be created. Segments 22 and 24 are switched for ejection. (bottom) Axial field in the RFQ during trapping and ejection. Figure reproduced with permission from [155].

applications this is more than compensated by the large background suppression. There is a limit to the achievable suppression, as neutral contaminant ions can also drift in to the IG-LIS volume, and become ionized due to the hot electrode surfaces, resulting in background rates of $100 - 1000$ ions/second. This is generally only a problem when the contaminant beam yield is many orders of magnitude more than the beam of interest.

## 3.3 TITAN

### 3.3.1 TITAN RFQ cooling and bunching

At TITAN, the ISAC beam is first delivered to the radio-frequency quadrupole (RFQ) linear Paul trap cooler and buncher [165]. The RFQ is biased several volts below the beam energy so that the beam enters with little energy. Through collisions with the helium buffer gas, the overall beam emittance is reduced, a requirement for precision mass measurements. Furthermore, the beam delivered from ISAC is continuous, so the RFQ bunches the beam permitting efficient injection into either EBIT or MPET.

TITAN's RFQ is segmented into 24 axial electrodes, each of which can be individually biased to create an axial drag field to pull ions into a potential well. The potential well at segment 23 provides axial confinement, while transverse confinement is provided through the application of a quadrupole RF field on the RFQ electrodes. A schematic of the electrode structure and the applied potentials during injection and extraction is shown in figure 3.6. The radio frequency is driven by a square wave with frequencies up to 1.2 MHz and peak-to-peak amplitudes up to 400 $V_{pp}$. The inner radius of the radio frequency rods is $r_0 = 11$ mm, and the total length of the RFQ is 700 mm. To cool the beam, a He buffer gas is introduced to the RFQ volume at a pressure of $\approx 0.01$ mbar. Helium is chosen for two reasons: First, the ionization energy of He is 24 eV which reduces the probability of charge exchange reactions, and second, He is much lighter than most isotopes measured using TITAN, which is beneficial for cooling. If the buffer gas is heavier than the injected beam, the energy of the injected beam increases in a process called RF-heating [166, 167]. For a model using so-called hard-sphere collisions in a Paul trap, the average energy transfer to the beam ion can be calculated as [167]

$$\langle \varepsilon_{\mathrm{RF}} \rangle = \kappa \frac{\kappa - 1}{(1+\kappa)^2} \tag{3.2}$$

where $\kappa = M/m$ is the ratio of the buffer gas with mass $M$ and the beam particle with mass $m$. For $0 < \kappa < 1$ the beam will be cooled, but for $\kappa > 1$ the beam will gain energy. For beams with $A < 12$, a buffer gas of $H_2$ is used instead of He, increasing the extraction efficiency by nearly a factor of 2 [165]. Once the ions are thermalized with the buffer gas, a process taking several milliseconds, they are ejected from the RFQ by quickly changing the voltages on segments 22 and 24. The beam is then accelerated to $1-2$ keV to the pulsed drift tube, where the beam is then pulsed to ground. The RFQ has an overall transfer efficiency of between $7-15\%$, depending on the beam used. Alkali metals typically have the highest efficiencies because they do not react with impurities in the buffer gas, while a beam of noble gases does react with impurities in the buffer gas, resulting in greatly decreased efficiencies. The probability for charge exchange can be reduced by decreasing the overall cooling time, however, this both reduces the total cooling time, potentially affecting the beam quality and it also reduces the total accumulation time, leading to a reduction in the total efficiency.

The potential felt by the ions in the well formed at electrode 23 is

$$\Phi(x,y,z;t) = \frac{\psi(t)}{r_0^2}\left(x^2 - y^2\right) + \frac{U_{\mathrm{end}} g}{z_0^2}\left(2z^2 - x^2 - y^2\right) \tag{3.3}$$

where $\psi(t)$ is a time-varying RF-signal, $U_{\mathrm{end}}$ is the axial trap depth, $r_0$ is the distance from the

axis to the outside of a rod, $z_0$ is the length of the trapping electrode and $g$ is a geometric factor. The first term provides radial confinement, while the second term provides axial confinement. In essence, this is a combined linear mass filter and Paul trap, and it is given the name of linear Paul trap [168, 169]. This differs from a Paul trap in that the trapping potential $U_{\text{end}}$ is held constant in a linear Paul trap, while in a Paul trap it is a function of time. A general choice for $\psi(t)$ is

$$\psi(t) = U_{dc} - U_{RF} S(\Omega t) \tag{3.4}$$

where $U_{DC}$ is a potential offset applied between adjacent rods, $U_{RF}$ is the amplitude of the time varying field $S(\Omega t)$, and $\Omega$ is the angular frequency of the field. We introduce the dimensionless time parameter $\xi = \Omega t/2$ to simplify the following derivations. This leads to the following equations of motion

$$\frac{\partial^2 x}{\partial \xi^2} + (a_x + a_{\text{end}} - 2q_x S(2\xi))x = 0 \tag{3.5}$$

$$\frac{\partial^2 y}{\partial \xi^2} + (a_y + a_{\text{end}} - 2q_y S(2\xi))y = 0 \tag{3.6}$$

$$\frac{\partial^2 z}{\partial \xi^2} - 2a_{\text{end}} z = 0 \tag{3.7}$$

with

$$a_u = a_x = -a_y = \frac{8qeU_{\text{dc}}}{mr_0^2\Omega^2} \tag{3.8}$$

$$q_u = q_x = -q_y = \frac{4qeU_{\text{RF}}}{mr_0^2\Omega^2} \tag{3.9}$$

$$a_{\text{end}} = -\frac{8qeU_{\text{end}}g}{mz_0^2\Omega^2}. \tag{3.10}$$

An important note is that for positive ions $a_{\text{end}}$ is always negative [170]. If $U_{\text{end}}$ is negative, the axial potential becomes a hill, causing ions to be lost axially. If we now introduce the effective term $a'_u = a_u + a_{\text{end}}$, we can write the radial equations of motion in the well known Mathieu form

$$\frac{\partial^2 u}{\partial \xi^2} + (a'_u - 2q_u S(2\xi))u = 0 \tag{3.11}$$

where $u$ corresponds to either the $x$ or $y$ solution. This is slightly different from the normal Mathieu equation due to the extra $a_{\text{end}}$ term. These are the same equations for a linear mass filter; however, $a_x$ and $a_y$ are shifted up by $-a_{\text{end}}$.

Several methods exist to solve the Mathieu equations. As the time-varying signal is peri-

odic, the solution lends itself to matrix methods. The transition matrix of the RF field moves the initial position and velocity of the particle to the final position and velocity

$$\begin{pmatrix} x_{n+1} \\ v_{n+1} \end{pmatrix} = \mathbf{M} \cdot \begin{pmatrix} x_n \\ v_n \end{pmatrix} = \mathbf{M}^n \cdot \begin{pmatrix} x_0 \\ v_0 \end{pmatrix} \tag{3.12}$$

where $x_0$ and $v_0$ are the initial position and velocity of the ion, and $x_n$ and $v_n$ are the position and velocity after $n$ applications of the periodic waveform. We can rewrite this using the eigenvectors $\vec{m}_i$ and eigenvalues $\lambda_i$ of $\mathbf{M}$

$$\begin{pmatrix} x_n \\ v_n \end{pmatrix} = \mathbf{M}^n \cdot \begin{pmatrix} x_0 \\ v_0 \end{pmatrix} = C_1 \lambda_1^n \vec{m}_1 + C_2 \lambda_2^n \vec{m}_2. \tag{3.13}$$

where the $C_i$'s describe the ion's initial conditions in terms of the eigenvectors of $\mathbf{M}$. If an ion's motion is to be stable, the position and velocities must remain finite as $n \to \infty$, requiring $\left|\lambda_{1,2}\right| \leq 1$. The eigenvalues of $\mathbf{M}$ are

$$\lambda_{1,2} = \frac{\mathrm{Tr}\{\mathbf{M}\}}{2} \pm i\sqrt{|\mathbf{M}| - \left(\frac{\mathrm{Tr}\{\mathbf{M}\}}{2}\right)^2}. \tag{3.14}$$

From Liouville's theorem (valid without buffer gas as the forces are conservative), the total phase space area of the ion bunch in the RFQ must be conserved, so the determinant of $\mathbf{M}$ must be 1. Substituting $s = \mathrm{Tr}\{\mathbf{M}\}/2$ the eigenvalues become

$$\lambda_{1,2} = s \pm i\sqrt{1 - s^2}. \tag{3.15}$$

There are several interesting properties of the eigenvalues: $\lambda_1^* = \lambda_2$ and $\lambda_1 \lambda_2 = 1$. From the earlier stability requirement that $\left|\lambda_{1,2}\right| \leq 1$ it follows that $s \leq 1$, otherwise the eigenvalues become real and greater than 1. The stability requirement is then simply

$$\mathrm{Tr}\{\mathbf{M}\} \leq 2 \tag{3.16}$$

for any given transition matrix.

To solve for $\mathbf{M}$ we can divide the waveform into time regions of constant voltage, solve the equations of motion in each time section, and take the product of the resultant set of matrices.

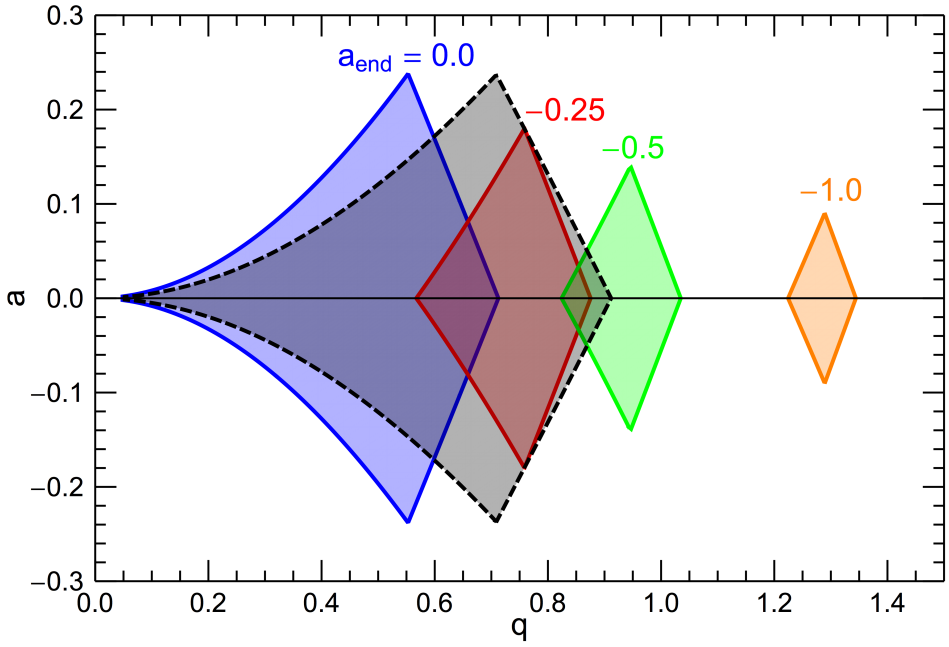


**Figure 3.7:** Stable regions (shaded) in a 50% duty-cycle square-wave driven linear Paul trap for different values of $a_{\text{end}}$. As the trap becomes deeper, the smaller the stable region becomes. For comparison, a sine-wave filter $a_{\text{end}} = 0$ is plotted as a dashed region.

Solving the equations of motion for a constant $S(t)$, yields the transition matrix [171]

$$\mathbf{M}(\tau, f) = \begin{pmatrix} \cos\left(\tau\sqrt{f}\right) & \sin\left(\tau\sqrt{f}\right)/\sqrt{f} \\ -\sqrt{f}\sin\left(\tau\sqrt{f}\right) & \cos\left(\tau\sqrt{f}\right) \end{pmatrix} \tag{3.17}$$

where $f = a' - 2q$, and $\tau$ is the length of time that the waveform is constant. It is then possible to build-up any given waveform through the application of $\mathbf{M}(\tau, f)$. The two most common waveforms are sinusoidal and square-wave, however, nearly all RFQ's in use at RIB facilities are sinusoidal.

Axially, the ions are confined for any choice of $a_{\text{end}}$, however, while providing axial confinement, the axial potential also adds a repulsive radial force. If the axial trap is too deep, the ions will collide with the RFQ rods and be lost. Figure 3.7 shows the effect of increasing the axial trap depth with regions inside the curves being stable, while the regions outside being unstable. In this mode of operation, it is possible to operate the linear Paul trap as a mass filter. By increasing the trap depth, only species with the correct $m/q$ will be confined, the others will be lost radially. At TITAN, the RFQ is operated with a trap well of $U_{\text{end}} = -1$ or $-2$ V, corresponding to an $a_{\text{end}}$ of $\approx -0.01$. The DC offset, $a_{x,y}$, is kept at zero, while $q$ is typically

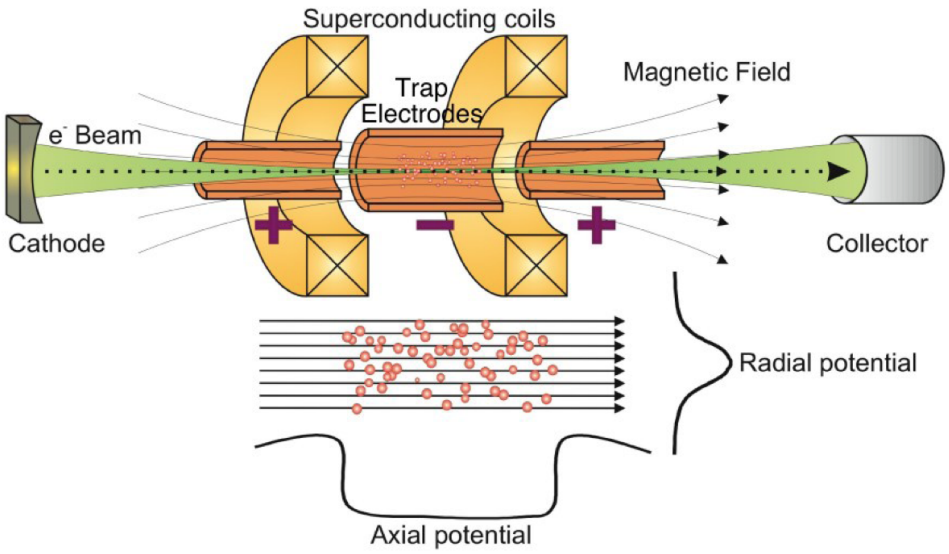


**Figure 3.8:** Schematic of the ion trap and electron beam in the electron beam ion trap. The central electrodes create a potential well, confining the ions axially, while the magnetic field and space charge from the electron beam provides radial confinement.

chosen to be close to 0.6.

### 3.3.2 Electron beam ion trap

A unique feature of TITAN, in the context of rare isotope science, is the ability to charge breed radioactive nuclides in an Electron Beam Ion Trap (EBIT) [172], creating what are known as Highly Charged Ions (HCI). In an EBIT, axial ion confinement is provided by an electrostatic potential well, while radial confinement is provided by a strong magnetic field and the space charge of the electron beam. Currently at TITAN, the EBIT typically use electron beam energies of up to $\approx 5$ keV and currents of up to 400 mA. High electron beam energies are required to reach the highest charge states of heavy nuclides. As an example, the ionization energy of hydrogen-like $U^{91+}$ is $\approx 130$ keV. The magnetic field compresses the electron beam near the trap centre, where the field is the strongest, creating a high current density, leading to faster charge breeding, provided good overlap of the electron beam and the ion cloud. Figure 3.8 shows a schematic drawing of the EBIT.

Charge-bred ions from EBIT are primarily used to increase the precision of mass measurements, as can be seen in equation 3.1. Several mass measurements that have benefited from the use of HCI's include: $^{74}$Rb [147], the mass of which is important for tests of the CKM matrix, the $^{71}$Ge-Ga [146] and $^{51}$Cr-V [173] $Q$-values which are important for neutrino sources

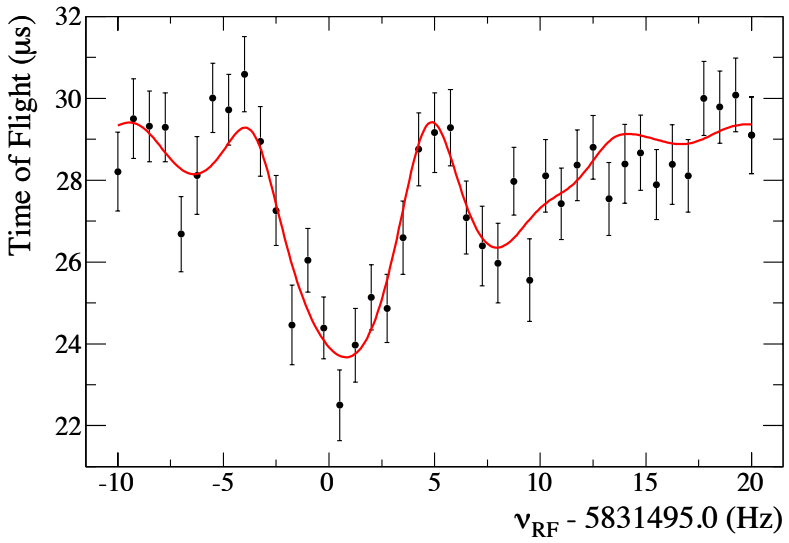


**Figure 3.9:** Resolving the 100 keV isomer in $^{78}$Rb using ions charge bred to $q = 8^+$, and an excitation time of 197 ms. An equivalent separation with SCI would need excitation times of $\approx 1.6$ s. Figure from [174].

that are used to calibrate neutrino detectors, and measurements of neutron-rich Rb and Sr isotopes [144, 145] that provide important input for astrophysical *r*-process calculations. HCI's can also increase the achievable resolving power $\mathscr{R}$ of a Penning trap mass spectrometer, as the resolving power goes as [148]

$$\mathscr{R} \approx \omega_c T_{RF} = \frac{qBT_{RF}}{m}. \tag{3.18}$$

This was demonstrated in $^{78}$Rb [174], where the ground state and 100 keV isomer could be resolved with an excitation time of 197 ms, the separation is clearly seen in figure 3.9. For Singly Charged Ions (SCI), an equivalent resolving power would have required excitation times of $> 1$ s.

### 3.3.3 Cooler Penning trap

Charge breeding increases the energy spread of the ion beam, which has a detrimental effect on mass measurements in MPET. To reduce the energy spread a cooler Penning trap (CPET) [175] has been constructed, and is being commissioned off-line. By using either electrons or protons, CPET will cool the charge breed beam sympathetically through collisions. A He buffer gas is not used, because excessive ion losses will result from charge exchange reactions between the HCI's and the He gas. Electrons are an ideal candidate because they quickly self cool through

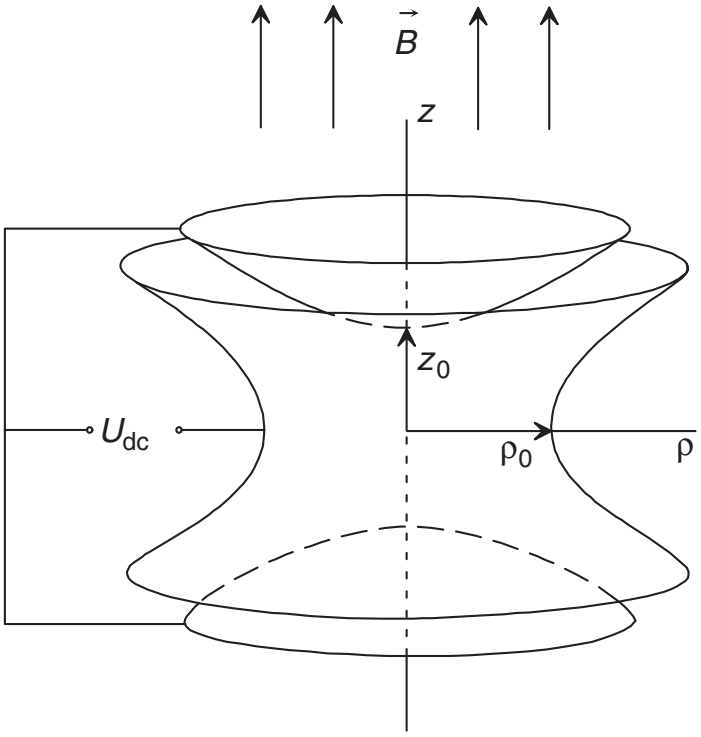


**Figure 3.10:** Schematic of a Penning trap. Figure reproduced with permission from [41].

synchrotron radiation in a strong 7 T magnetic field, while protons do not. A detriment of using electrons is that they can be captured by the HCI, causing a loss of the ion of interest; however, simulations have shown survival rates for $U^{92+}$ of more than 90% for a cooling time of 500 ms [176].

CPET is planned to be installed in the TITAN beam line in early 2016.

### 3.3.4 Measurement Penning trap

The measurement Penning trap (MPET) is the principle trap of TITAN, dedicated to performing accurate and precise mass measurements. The mass is determined by measuring the cyclotron frequency $\omega_c = qB/m$ of an ion in a homogeneous magnetic field. The magnetic field only provides radial confinement, while axial confinement is provided by a three dimensional electric quadrupole field. A natural choice for the electric field is a harmonic potential,

$$V = ax^2 + by^2 + cz^2 \tag{3.19}$$

where $a$, $b$ and $c$ are undetermined coefficients. By solving the Laplace equation, we find that the sum of the coefficients must be zero. The natural choice is to preserve cylindrical symmetry

**Table 3.1:** Characteristic trap dimensions for MPET.

| Parameter | Length (mm) |
|---|---|
| $r_0$ | 15 |
| $z_0$ | 11.785 |
| $d_0$ | 11.21 |

by setting $a = b$, constraining $a = -c/2$, leading to the potential

$$V(z,r) = \frac{c}{2}(2z^2 - r^2). \tag{3.20}$$

$c$ is determined by taking the difference between the two equipotentials, as shown in figure 3.10, where the top and bottom sheets are called the "end-cap" electrodes and the middle sheet is called the "ring" electrode. This leads to the potential

$$V_0 = V(z_0,0) - V(0,r_0) = c(2z_0^2 - r_0^2) \tag{3.21}$$

$$c = \frac{V_0}{2d_0^2} \tag{3.22}$$

where $r_0$ is the distance from the trap centre to the closest approach of the ring electrode, $z_0$ is the distance from the trap centre to the closest approach of the end-cap electrodes, and $d_0^2 = (2z_0^2 + r_0^2)/4$ is called the characteristic trap distance. These trap measurements for MPET are summarized in table 3.1. The quadrupole potential is then

$$V(z,r) = \frac{V_0}{2d_0^2}\left(2z^2 - r^2\right). \tag{3.23}$$

#### 3.3.4.1 Ion motion in a Penning trap

In a Penning trap the ions are affected by both the electric field and the magnetic field. A superconducting solenoid magnet provides a strong and homogeneous magnetic field $\vec{B} = B_0\hat{z}$ in the trapping volume. The combination of these fields yields the equations of motion [177]

$$\ddot{x} - \omega_c\dot{y} - \frac{\omega_z^2}{2}x = 0 \tag{3.24}$$

$$\ddot{y} + \omega_c\dot{x} - \frac{\omega_z^2}{2}y = 0 \tag{3.25}$$

$$\ddot{z} + \omega_z^2 z = 0 \tag{3.26}$$

**Table 3.2:** Eigenfrequencies for $^{39}K^{+}$ in MPET.

| Motion | Frequency |
|---|---|
| $\nu_c$ | 1 457 822.6 Hz |
| $\nu_+$ | 1 451 683.4 Hz |
| $\nu_z$ | 133 508.2 Hz |
| $\nu_-$ | 6 139.2 Hz |

where we have defined $\omega_z^2 = qV_0/md_0^2$. To solve for the radial motions, we introduce the complex coordinate $u = x + iy$, transforming the radial equation of motion to

$$\ddot{u} + i\omega_c \dot{u} - \frac{\omega_z^2}{2} u = 0. \tag{3.27}$$

The radial motion should be periodic, so we try a solution of the form $u \propto \exp(-i\omega t + \phi)$. This yields two eigenfrequencies

$$\omega_\pm = \frac{1}{2}\left(\omega_c \pm \sqrt{\omega_c^2 - 2\omega_z^2}\right), \tag{3.28}$$

where $\omega_\pm$ are called the reduced cyclotron and magnetron frequencies. For the eigenfrequencies to be real, the condition $\omega_c > \sqrt{2}\omega_z$, or in terms of the applied fields $qB_0^2/m > 4V_0/d_0^2$, must be fulfilled. For typical choices of trapping voltages, this leads to the hierarchy $\omega_c > \omega_+ \gg \omega_z \gg \omega_-$. Typical values for the eigenfrequencies of $^{39}K^{+}$ in MPET are shown in table 3.2. The solution to the radial equation of motion is then

$$x(t) = r_+ \cos(\omega_+ t + \phi_+) + r_- \cos(\omega_- t + \phi_-) \tag{3.29}$$

$$y(t) = r_+ \sin(\omega_+ t + \phi_+) - r_- \sin(\omega_- t + \phi_-), \tag{3.30}$$

where $\phi_\pm$ are the initial phases of the ion motion in the reduced cyclotron and magnetron modes, respectively.

From equation 3.28 the eigenfrequencies can be combined into several useful relationships [177]:

$$\omega_c = \omega_+ + \omega_- \tag{3.31}$$

$$\omega_z^2 = 2\omega_+\omega_- \tag{3.32}$$

$$\omega_c^2 = \omega_+^2 + \omega_z^2 + \omega_-^2. \tag{3.33}$$

From the above, we see that the cyclotron frequency is not an eigenfrequency of the ion's motion, it is instead a combination of the radial eigenfrequencies. By measuring the eigenfrequencies directly, or by measuring a "side-band" frequency, a frequency that is a linear combination of the eigenfrequencies, the cyclotron frequency can be determined. Two methods for measuring the eigenfrequencies directly are Fourier-Transform Ion Cyclotron Resonance (FT-ICR) [178] and Phase-Imaging Ion Cyclotron Resonance (PI-ICR) [179]. FT-ICR measures the current on a trapping electrode induced by an ion's motion. This method produces the most precise mass values; however, it involves ion observation times of several tens of seconds, a problem for the short-lived nuclides measured with TITAN. Another draw back is detecting the induced current requires a high-quality LC circuit tuned to the desired eigenfrequency, limiting the ability to quickly change isotopes, as such a resonant circuit would also have to be changed. In on-line measurements, several different isotopes are usually measured in a single beam time, limiting the FT-ICR technique to stable and very long-lived nuclides.

The PI-ICR technique also measures the eigenfrequencies, not by measuring induced currents, but instead projects the phase of the ion's motion onto a position-sensitive detector. This technique has shown great promise in measuring stable isotopes, reaching precisions of 0.2 ppb [180].The PI-ICR technique can in principle reach the same precision as the FT-ICR technique, provided the same care is taken in preparing the ion, but with the benefit of not needing a tuned LC circuit.

#### 3.3.4.2 Sideband quadrupole excitation

One way to access the cyclotron frequency is to excite the frequency sideband $\omega_c = \omega_+ + \omega_-$, and measure the amount of conversion from a state of pure magnetron motion to a state of pure reduced cyclotron motion. An ion is excited with a weak quadrupole field

$$V_{RF} = \frac{V_q}{2a^2} \cos\left(\omega_{RF} t + \phi_{RF}\right) \left(x^2 - y^2\right) \tag{3.34}$$

where $V_q$ is the excitation amplitude at a distance $a$ from the trap centre, with frequency $\omega_{RF}$ and phase $\phi_{RF}$. This field is applied radially by split electrodes, as schematically shown in figure 3.11. Usually the excitation voltage is applied on a split ring electrode, but at TITAN the excitation is applied on the split correction guard electrodes. To produce a quadrupolar excitation field, adjacent electrodes receive signals that are 180° out of phase. By breaking the cylindrical symmetry of the trapping field with the excitation, the two radial eigenmotions can be coupled, leading to an interconversion of modes. Similarly, quadrupole excitations can be applied in the $xz$ or $yz$ planes, allowing the axial and radial motions to be coupled [181].

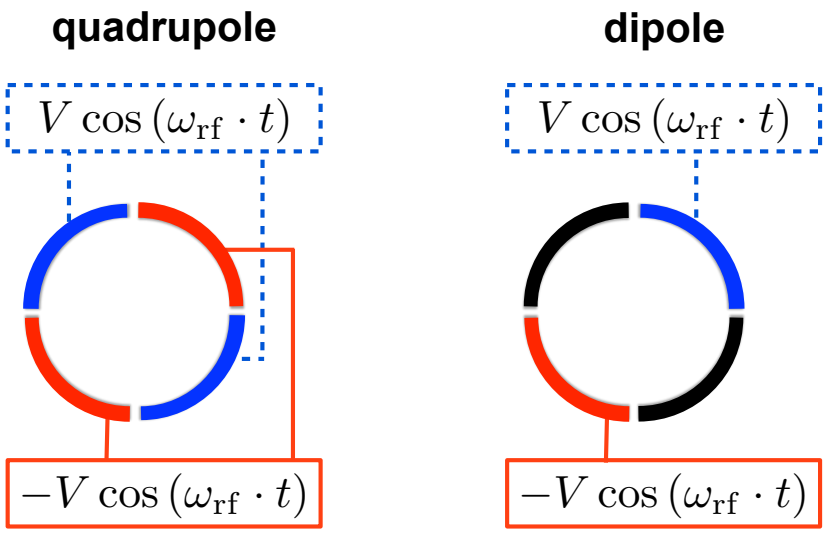


**Figure 3.11:** RF application for quadrupole and dipole excitation. The annular segment represents the guard electrodes of MPET as shown in figure 3.22, which are segmented into four parts.

The equation of motion can be solved classically [182], however, the solution is much more readily obtained in the quantum domain [183]. First, we write the Hamiltonian as

$$H = \frac{1}{2m}\left(\vec{p} - q\vec{A}\right)^2 + qV(z,r) \tag{3.35}$$

where $\vec{A}$ is the vector potential of the magnetic field, chosen to be $\vec{A} = (B/2)(-y\hat{x} + x\hat{y})$ for convenience. It is possible to write the canonical coordinates as [184, 183]

$$q_+ = -\sqrt{\frac{m}{\omega_1}}(\dot{y} + \omega_- x) \qquad p_+ = \sqrt{\frac{m}{\omega_1}}(\dot{x} - \omega_- y) \tag{3.36}$$

$$q_- = \sqrt{\frac{m}{\omega_1}}(\dot{y} + \omega_+ x) \qquad p_- = \sqrt{\frac{m}{\omega_1}}(\dot{x} - \omega_+ y) \tag{3.37}$$

$$q_3 = \sqrt{m\omega_z}z \qquad p_3 = \sqrt{\frac{m}{\omega_z}}\dot{z} \tag{3.38}$$

which leads to the Hamiltonian

$$H = \frac{\omega_+}{2}\left(q_+^2 + p_+^2\right) - \frac{\omega_-}{2}\left(q_-^2 + p_-^2\right) + \frac{\omega_z}{2}\left(q_z^2 + p_z^2\right). \tag{3.39}$$

This is the Hamiltonian for two normal simple harmonic oscillators, in $+$ and $z$, and an inverted oscillator in $-$. The quantum problem can now be formulated by constructing the annihilation

and creation operators

$$a_{\pm} = \frac{1}{\sqrt{2\hbar}}\left(q_{\pm} + ip_{\pm}\right), \quad a_{\pm}^{\dagger} = \frac{1}{\sqrt{2\hbar}}\left(q_{\pm} - ip_{\pm}\right), \tag{3.40}$$

which follow the standard commutation relations. The quadrupole excitation field can now be written in terms of the creation and annihilation operators:

$$V_{rf} = \frac{V_q}{2a^2}\left(e^{-i(\omega_{rf}t+\phi_{rf})}\left(a_+^{\dagger 2} + a_-^2 + 2a_+^{\dagger}a_-\right) + e^{i(\omega_{rf}t+\phi_{rf})}\left(a_+^2 + a_-^{\dagger 2} + 2a_-^{\dagger}a_+\right)\right). \tag{3.41}$$

The first term describes the process of absorbing a photon from the exciting field, and creating two quanta of reduced cyclotron motion with energy $2\hbar\omega_+$. The second term describes the process of absorbing a photon from the exciting field, and annihilating two quanta of magnetron motion with energy $2\hbar\omega_-$. The third term describes the process of absorbing a photon with energy $\hbar\omega_c$ and converting a quanta of magnetron motion into a quanta of reduced cyclotron motion. The last three terms describe the inverse process. Only the interconversion of modes is of interest, thus we arrive at the Hamiltonian

$$H(t) = \hbar g\left(e^{-i(\omega_{rf}t+\phi_{rf})}a_+^{\dagger}(t)a_-(t) + e^{i(\omega_{rf}t+\phi_{rf})}a_-^{\dagger}(t)a_+(t)\right) \tag{3.42}$$

where $g = qV_q/(2m\sqrt{\omega_c^2 - 2\omega_z^2})$ is the coupling constant between the magnetron and reduced cyclotron modes. Ignoring the axial motion, the complete Hamiltonian for the radial motion during an excitation is [183]

$$\begin{aligned} H(t) = {} & \hbar\omega_+\left(a_+^{\dagger}a_+ + \frac{1}{2}\right) - \hbar\omega_-\left(a_-^{\dagger}a_- + \frac{1}{2}\right) \\ & + \hbar g\left(e^{-i\left(\omega_{rf}t+\phi_{rf}\right)}a_+^{\dagger}(t)a_-(t) + e^{i\left(\omega_{rf}t+\phi_{rf}\right)}a_-^{\dagger}(t)a_+(t)\right). \end{aligned}$$

Rather than solving the Schrödinger equation for the Hamiltonian above, we find the amount of conversion from one mode to the other by considering a quantum two-level system excited by a time-varying potential. We start with the time-dependent Schrödinger equation

$$i\hbar\frac{\partial\Psi}{\partial t} = \left(\hat{H}_0 + \hat{V}\right)\Psi \tag{3.43}$$

where $\hat{H}_0$ is the time independent Hamiltonian and $\hat{V}$ is the sinusoidal excitation. Expanding

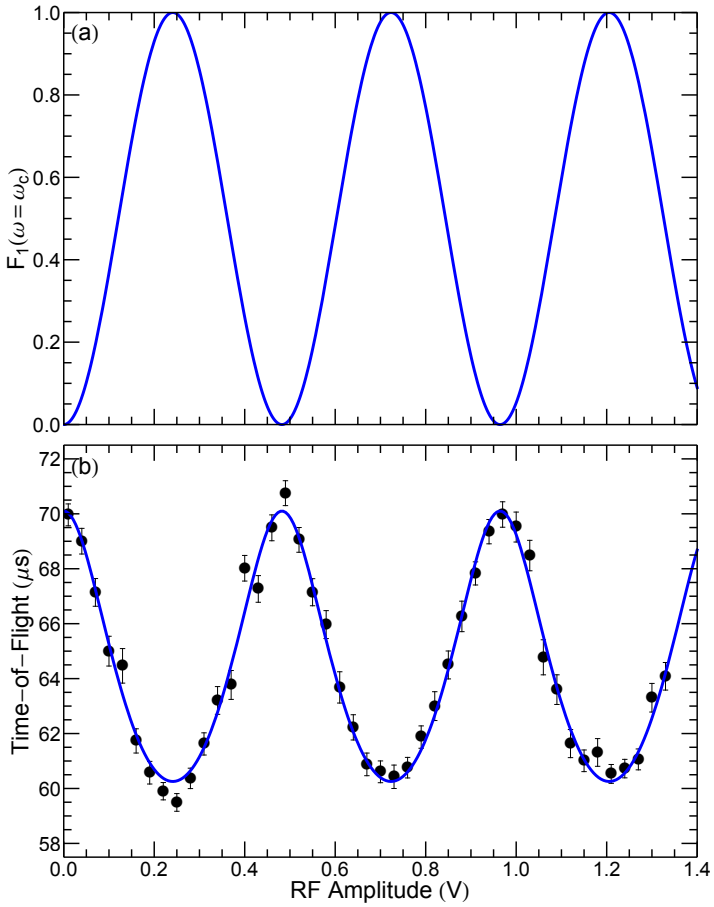


**Figure 3.12:** Conversion between magnetron (slower) and reduced cyclotron (faster) as a function the excitation amplitude for an excitation time of 0.1 s. (a) Transition probability (b) Observed time-of-flight as a function of the RF amplitude. The blue line is a fit to the data. One full conversion occurs near $V_{rf} \approx 0.24$ V.

$\Psi$ in terms of the unperturbed wave functions $\Psi^0$

$$\Psi = \sum_k b_k \Psi_k^{(0)},$$

we are lead to the following set of differential equations [185, 186]

$$i\hbar \frac{\partial b_m}{\partial t} = \sum_k b_k V_{mk} e^{i\omega_{mk} t} \tag{3.44}$$

where $V_{mk}$ is the matrix element connecting states $m$ and $k$, and $\omega_{mk} = (E_m - E_k)/\hbar$. We now

assume a sinusoidal perturbation with frequency $\omega$

$$\hat{V} = \hat{F}\cos(\omega t) \tag{3.45}$$

$$= \frac{\hat{F}}{2}\left(e^{i\omega t} + e^{-i\omega t}\right) \tag{3.46}$$

where $\hat{F}$ is a general operator. Substituting this into equation 3.44 leads to

$$i\hbar\frac{\partial b_m}{\partial t} = \sum_k b_k F_{mk}\left(e^{i(\omega_{mk}+\omega)t} + e^{i(\omega_{mk}-\omega)t}\right). \tag{3.47}$$

We note that the right hand side of the above is identical in form to equation 3.42. If $\omega$ is close to $\omega_{mn}$, then only these states will contribute to the solution. In the other states, the frequency terms are large and will be averaged out over the time that $\hat{V}$ is applied. By making this "rotating wall" approximation we only need to examine the slowly varying term. This leads to the two coupled equations

$$i\hbar\frac{\partial b_m}{\partial t} = b_n F_{mn} e^{i\varepsilon t} \tag{3.48}$$

$$i\hbar\frac{\partial b_n}{\partial t} = b_m F_{nm} e^{-i\varepsilon t} \tag{3.49}$$

where $\varepsilon = \omega_{mn} - \omega$ is the frequency detuning. Here we care about converting magnetron motion into reduced cyclotron motion, so the frequency that will create maximal conversion is $\omega_{+-} = (E_+ - E_-)/\hbar = \omega_+ + \omega_- = \omega_c$. Solving these equations leads to

$$b_-(t) = Ae^{i\varepsilon t/2}\left(\cos\Omega t - \frac{i\varepsilon}{2\Omega}\sin\Omega t\right) - Be^{i\varepsilon t/2}\frac{ig}{\Omega}\sin\Omega t \tag{3.50}$$

$$b_+(t) = -Ae^{-i\varepsilon t/2}\frac{ig}{\Omega}\sin\Omega t + Be^{-i\varepsilon t/2}\left(\cos\Omega t - \frac{i\varepsilon}{2\Omega}\sin\Omega t\right) \tag{3.51}$$

where $g = F_{mn}/\hbar$, $\Omega = \sqrt{\varepsilon^2/4 + g^2}$, and $A$ and $B$ are determined from the initial normalization of the wave function. This solution is much easier to work with when it is expressed as a matrix

$$\begin{aligned}\begin{pmatrix} b_-(t) \\ b_+(t) \end{pmatrix} &= W(\varepsilon,t)M(\varepsilon,g,t)\begin{pmatrix} b_-(0) \\ b_+(0) \end{pmatrix} \\ &= \begin{pmatrix} e^{i\varepsilon t/2} & 0 \\ 0 & e^{-i\varepsilon t/2} \end{pmatrix}\begin{pmatrix} \cos\Omega t + \frac{i\varepsilon}{2\Omega}\sin\Omega t & -\frac{ig}{\Omega}\sin\Omega t \\ -\frac{ig}{\Omega}\sin\Omega t & \cos\Omega t - \frac{i\varepsilon}{2\Omega}\sin\Omega t \end{pmatrix}\begin{pmatrix} b_-(0) \\ b_+(0) \end{pmatrix}\end{aligned} \tag{3.52}$$

where $W(\varepsilon,t)$ is the phase evolution of the state vector, and $M(\varepsilon,g,t)$ is the propagation matrix.

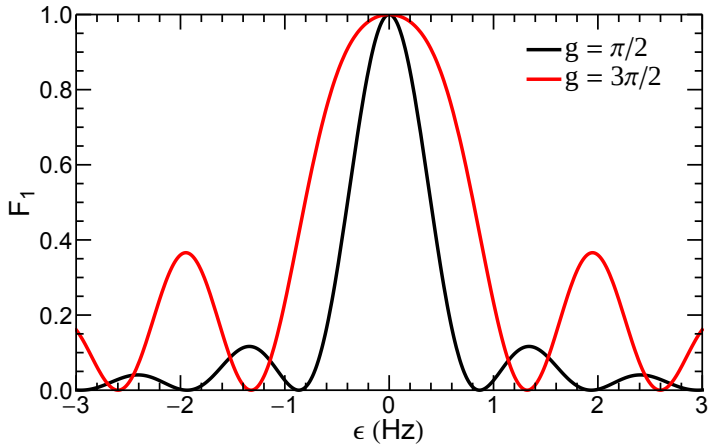


**Figure 3.13:** Quadrupole excitation line shape for $g = \pi/2, 3\pi/2$ for an excitation time of 1 second.

If we start with a state of pure magnetron motion, then the probability $F_1(\varepsilon, g, t)$ for an ion to be converted to a state of pure reduced cyclotron is the (1,2) component of the propagation matrix [183]

$$F_1(\varepsilon, g, t) = \left|M_{1,2}(\varepsilon, g, t)\right| = \frac{g^2}{\Omega^2} \sin^2 \Omega t. \tag{3.53}$$

Maximal conversion for $\varepsilon = 0$ occurs when $\Omega t = gt = (2n+1)\pi/2$ for integer $n$. Conversely, minimal conversion occurs with $gt = n\pi$. This is identical in form to Rabbi flopping, meaning the ion motion will change between magnetron and reduced cyclotron motion as a function of $g$ or $t$. This behaviour is demonstrated in figure 3.12, where the excitation amplitude, which is proportional to $g$, was varied for the ion $^{39}K^+$ with a fixed excitation time of 100 ms. Figure 3.13 demonstrates the probability to be converted from a state of pure magnetron motion to pure reduced cyclotron motion as a function of the frequency detuning. The conversion line shape is narrowest when $g = \pi/2$, a feature making it the most interesting for experiment.

We must now connect the quantum solution with the classical ion motion. In MPET, an ion typically has a few electron volts of energy, corresponding to quantum numbers of $\approx 10^9$. By constructing coherent states of the magnetron and reduced cyclotron oscillators the classical motions [182] can be recovered [183]. Figure 3.14 shows the radial evolution of an ion subject to a quadrupole excitation. During the excitation, the radius of the reduced cyclotron motion slowly grows, while the radius of the magnetron motion slowly decreases.

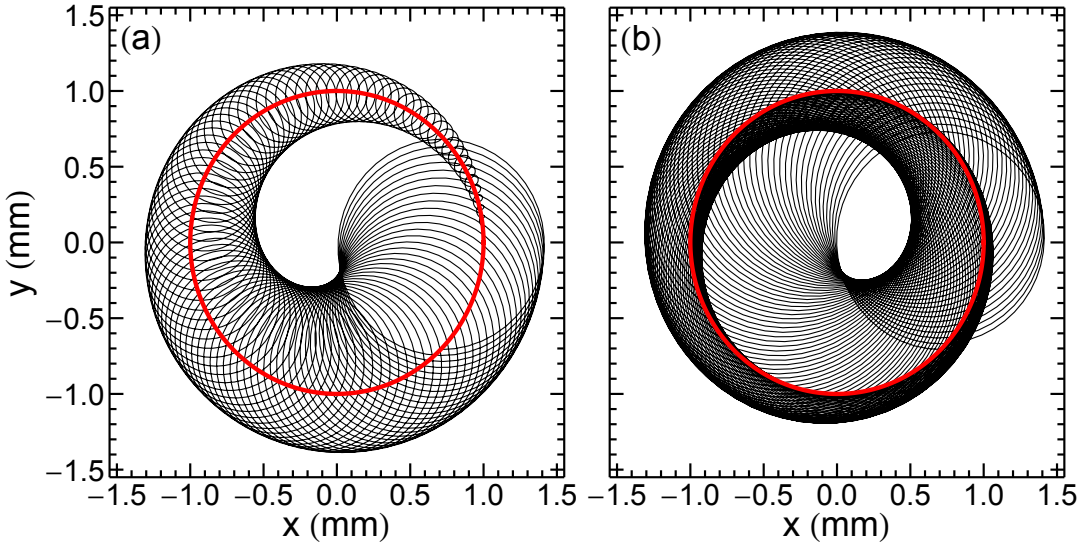


**Figure 3.14:** Ion motion under a quadrupolar excitation. (a) $t \in [0, \tau/2]$, (b) $t \in [\tau/2, \tau]$, where $\tau$ is the time required for one complete conversion. The ion is started on a magnetron radius of 1 mm, as denoted by the red circle.

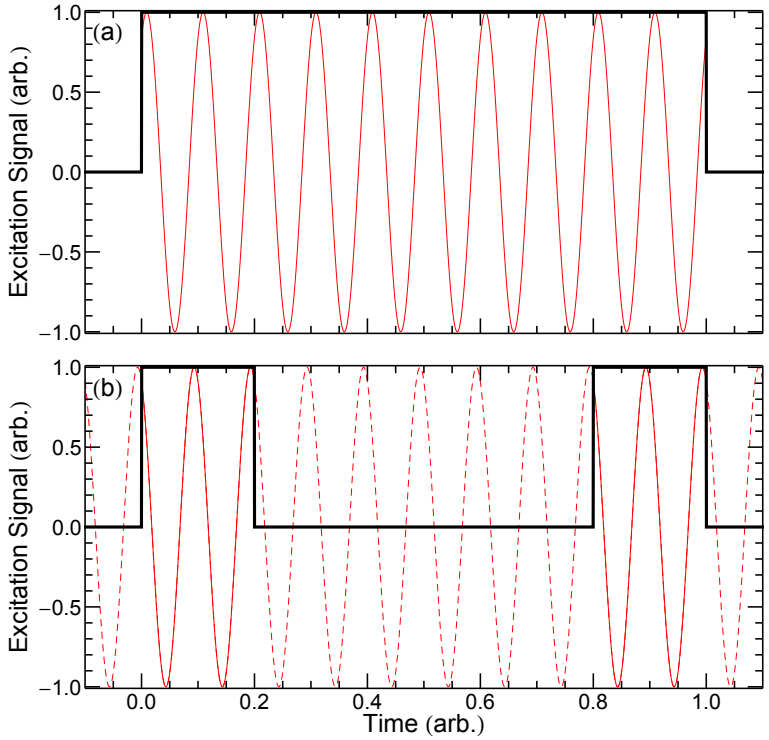


**Figure 3.15:** Excitation pulses for (a) quadrupole and (b) Ramsey excitations. The black lines show when the signal is applied, and the red line shows the sinusoidal excitation. The red dashed line shows that the excitation is phase coherent between the first and second excitation pulses of the Ramsey scheme.

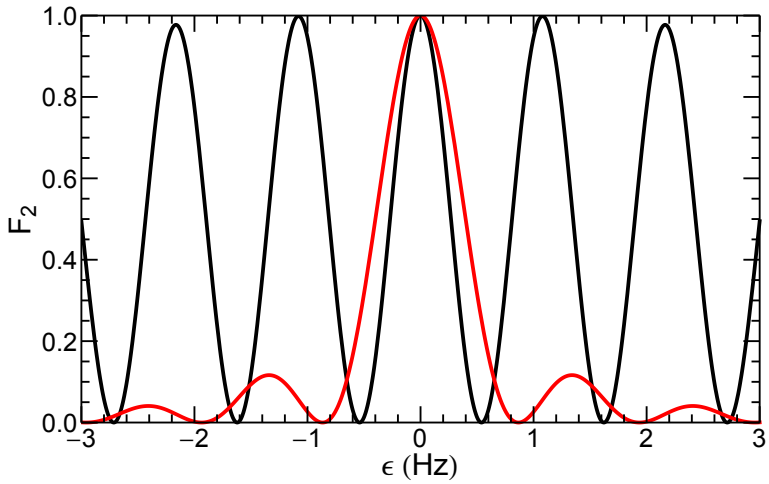


**Figure 3.16:** Ramsey excitation line shape (black), compared with a quadrupole excitation (red). The Ramsey line shape uses an excitation scheme $t_1 - t_0 - t_2$ of $0.1 - 0.8 - 0.1$ s, while the quadrupole excitation uses an excitation time of 1 s.

#### 3.3.4.3 Ramsey excitation

Instead of applying the excitation field in one pulse, the excitation can be applied at two different times, allowing for a phase to accumulate between the RF-field and the ion motion. This time-separated oscillatory field technique [187, 183, 188] was first pioneered by Ramsey for molecular beams, for which he received the Nobel prize, and as such are called "Ramsey" excitations. The Ramsey method leads to an interference-type line shape, narrowing the central lobe, thereby increasing the precision of the measurement. The line shape can be found by successive applications of $M(\varepsilon, g, t)$, being careful to track the phase difference between the RF and ion motion. The excitation is split into two pulses, one of length $t_1$, and the other of length $t_2$, separated by a waiting period of length $t_0$. For full conversion $g(t_1 + t_2) = \pi/2$, which is the same condition for single pulse quadrupole excitation length of $t_1 + t_2$. Figure 3.15 shows the difference in the time structure between a single pulse and a Ramsey pulse. An important part of the Ramsey excitation is that the phase between the first and second RF pulses be phase coherent; otherwise, the maximum conversion will be shifted in frequency [183, 189]. At TITAN, phase coherence is accomplished by using an RF switch to turn on and off the RF that is applied to the trap, while keeping the RF function generator continually running. The

transition probability is

$$F_2(\varepsilon,g,t_2,t_0,t_1) = |M(\varepsilon,g,t_2)M(\varepsilon,0,t_0)M(\varepsilon,g,t_1)|^2_{1,2} \tag{3.54}$$

$$\begin{aligned} F_2(\varepsilon,g,t_2,t_0,t_1) = \frac{g^2}{\Omega^2}\Bigg(&\sin^2\left(\frac{\varepsilon t_0}{2}\right)\sin^2\left(\Omega(t_1-t_2)\right) \\ &+\left(\cos\left(\frac{\varepsilon t_0}{2}\right)\sin\left(\Omega(t_1+t_2)\right)+\frac{\varepsilon}{2\Omega}\sin\left(\frac{\varepsilon t_0}{2}\right)\right. \\ &\left.\left(\cos(\Omega(t_1+t_2))-\cos(\Omega(t_1-t_2))\right)\right)^2\Bigg), \end{aligned} \tag{3.55}$$

which is found through successive applications of the propagation matrix $M(\varepsilon,g,t)$. The line shape is narrowest when $t_1 = t_2$, reducing to

$$F_2(\varepsilon,g,t_2,t_0,t_1) = \frac{g^2}{\Omega^2}\left(\cos\left(\frac{\varepsilon t_0}{2}\right)\sin(2\Omega t)+\frac{\varepsilon}{2\Omega}\sin\left(\frac{\varepsilon t_0}{2}\right)\left(\cos(2\Omega t)-1\right)\right)^2. \tag{3.56}$$

If $t_0 = 0$, the normal line shape (equation 3.53) is recovered. A Ramsey conversion line shape is plotted in figure 3.16. The Ramsey technique increases the overall precision by a factor of 2-3, depending on the choice of excitation and waiting times, allowing for more precise measurements, or for the same precision as with the one pulse excitations but in a shorter amount of time.

#### 3.3.4.4 Dipole cleaning

Contaminant ions may be delivered simultaneously with the ion of interest. These contaminants can potentially shift the measured cyclotron frequency in the trap through their mutual interactions [190, 191]. By applying a dipole field to the trap at one of the eigenfrequencies it is possible to remove unwanted ions from the trapping region [181]. The dipole field is created by applying 180° out of phase signals to opposite electrodes, as shown in figure 3.11. The growth of the eigenmotion depends on the relative phase difference between the RF excitation and the ion motion, but given a large enough excitation amplitude, and a long enough excitation pulse, the motion will grow linearly [192] until the ion is lost on the trap electrodes, either radially in the case of radial excitations, or ejected from the trap by axial excitations. At TITAN, the reduced cyclotron motion of unwanted ions is excited, causing the ions orbit to increase in radius. The magnetron motion could also be excited; however, the magnetron motion is nearly constant with mass, limiting the resolving power.

#### 3.3.4.5 Time-of-flight ion cyclotron resonance

In order to measure the conversion line shape, the Time-of-Flight Ion Cyclotron Resonance (TOF-ICR) technique [182] is used at TITAN. By converting the magnetron motion to reduced cyclotron motion, a large gain in radial energy occurs (because $\omega_+ >> \omega_-$), and this gain in energy can be measured in the TOF of an ion from the trap to a detector. The ion acts as a current-carrying loop, having a magnetic dipole moment depending on the radial energy of the ion $\mu(\omega) = E(\omega)/B_0$, where $\omega$ is the frequency of the applied excitation. Extracting an ion through a magnetic field gradient creates a force on the magnetic dipole, changing the radial energy into axial energy, and causing the time-of-flight to the detector to change depending on the radial energy of the ion in the trap. If the electric and magnetic fields are known along the flight path to the detector, the TOF can be calculated as

$$T = \int_{z_0}^{z_1} \left( \frac{m}{2(E_0 - qV(z) - \mu(\omega)B(z))} \right)^{1/2} \mathrm{d}z \tag{3.57}$$

where $E_0$ is the initial total energy of the ion, $V(z)$ and $B(z)$ are the electric potential and magnetic field strength along the $z$-axis from the trap at $z_0$ to the detector at $z_1$. The radial energy of the ion after an excitation is dominated by the kinetic energy of the reduced cyclotron motion

$$E(\omega) \approx \frac{1}{2} m\omega_+^2 F_1(\omega_c - \omega, g, t)\rho_-^2(0) \tag{3.58}$$

where $\rho_-(0)$ is the initial radius of the magnetron motion. The cyclotron frequency is the found by scanning the excitation frequency $\omega_{rf}$ and finding the minimum in the TOF distribution, as seen in figure 3.17 for $^{23}Na^+$.

#### 3.3.4.6 Measuring the axial frequency of the Penning trap

Using TOF-ICR methods it is possible to directly determine the reduced cyclotron frequency $\omega_+$, and to infer the magnetron frequency using the relationship $\omega_- = \omega_c - \omega_+$. These methods are not directly applicable to determining the axial frequency, since there is no convenient way to couple the axial and radial modes. Moreover, if one could couple the axial and radial modes, the resonance would be "washed out" due to the axial motion of the ion in the trap. Instead, we can measure the phase evolution of the ions by varying the trapping time. By intentionally closing the trap at the incorrect time, we can create ions which have sizeable axial oscillations. Usually, the correct time to close the trap is the time when they are near the trap centre, such that they have the minimum possible axial energy. As the switch timings are well controlled, we can start the ions on the same axial phase on each injection cycle. The TOF to the detector

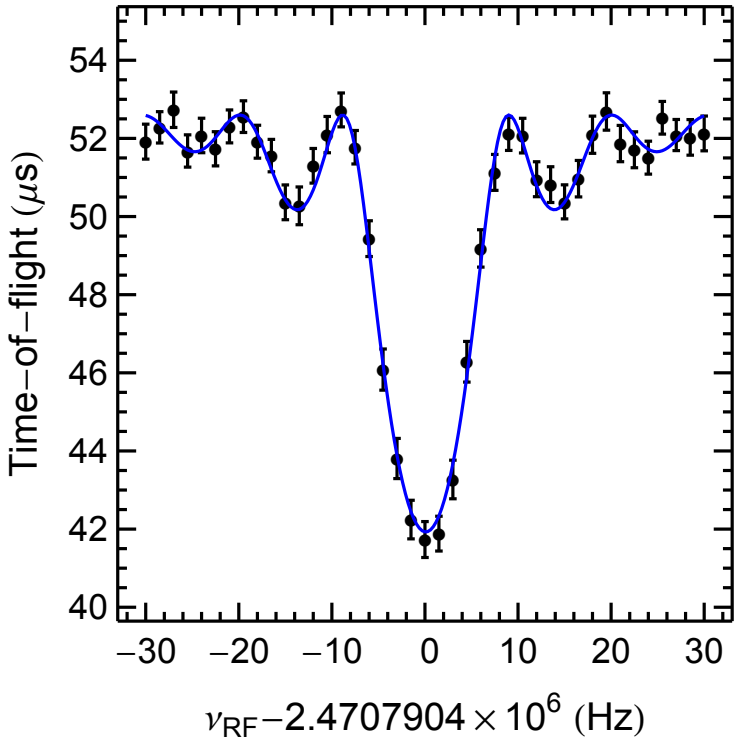


**Figure 3.17:** TOF-ICR resonance of $^{23}Na^{+}$ for an excitation time of 97 ms. The blue line is a fit of the theoretical line shape [182].

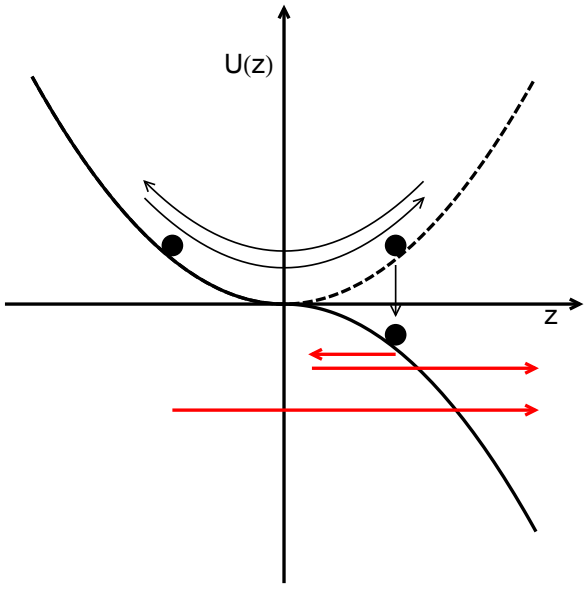


**Figure 3.18:** Ion trajectories when being ejected. The ion on the left is already travelling to the right, so no additional turn-around time is required. The ion on the right is travelling to the left, and must turn-around before leaving the trap.

is then

$$T = \int_{z_0}^{z_1} \left( \frac{m}{2(E_0 - qU(z))} \right)^{1/2}. \tag{3.59}$$

There is the added complication that the TOF depends on the axial phase of the motion – the velocity vector of the ion matters. This is because the ion can be moving away from the exit when the trap is opened. To calculate the correct TOF, we must account for the "turn-around" time of the ion bunch. Because the potential in the $z$-direction is harmonic, we know the velocity of the ion at the moment the trap is opened,

$$E = \frac{1}{2} m A^2 \omega_z^2 \cos^2(\omega_z t + \phi_0) \tag{3.60}$$

where $A$ is the amplitude of the axial oscillation, and $\phi_0$ is the initial phase of the ion. To simplify calculating the turn-around time, we assume that the trap electrodes switch instantaneously, preserving the ion's kinetic energy and spatial position, changing only the potential energy. The position where the ion turns around is found by solving $U(z) = E$, with the turn-around time being twice the length of time for the ion to go from the starting position $A\cos(\omega_z t + \phi_0)$ to the turn-around position. A drawing of extracting an ion from the trap is shown in figure 3.18. In the figure two ions are shown: an ion on the right of the trap moving towards the left, and an ion on the left of the trap moving to the right. For the ion moving left, it continues travelling to the left until it turns around and can exit the trap, while the ion moving to the right can immediately leave the trap. The rest of the TOF to the detector is calculated as normal. A measurement of the axial frequency is shown in figure 3.19. Each data point is the average of 205 injection-ejection cycles, with the total trapping time varied between 1 and 100 ms. The "kink" in the TOF, at $\approx 2\,\mu$s, occurs just before the ions turn around and begin travelling towards the exit. The longest TOF occurs just after turning around, when the ions are heading away from the detector, while the fastest time of flight occurs when the ions are near the centre of the trap, and are travelling towards the detector. This is expected, as the ions on the exit side of the trap have their potential energy reduced when the trap is opened. Ions on the entrance side of the trap have more potential energy, leading to slightly higher velocities, and a shorter TOF. For $^{39}K^+$, the axial frequency was measured to be 133508.24 (18) Hz, with a fitted oscillation amplitude of 1.8(1) mm.

This technique can also be used to minimize the axial oscillation amplitude of the ion bunch. Because of higher order components in the trapping potential, the axial and radial modes in a Penning trap can couple, leading to a potential shift in the measured cyclotron frequency. By carefully eliminating axial oscillations, any frequency shifts related to the axial

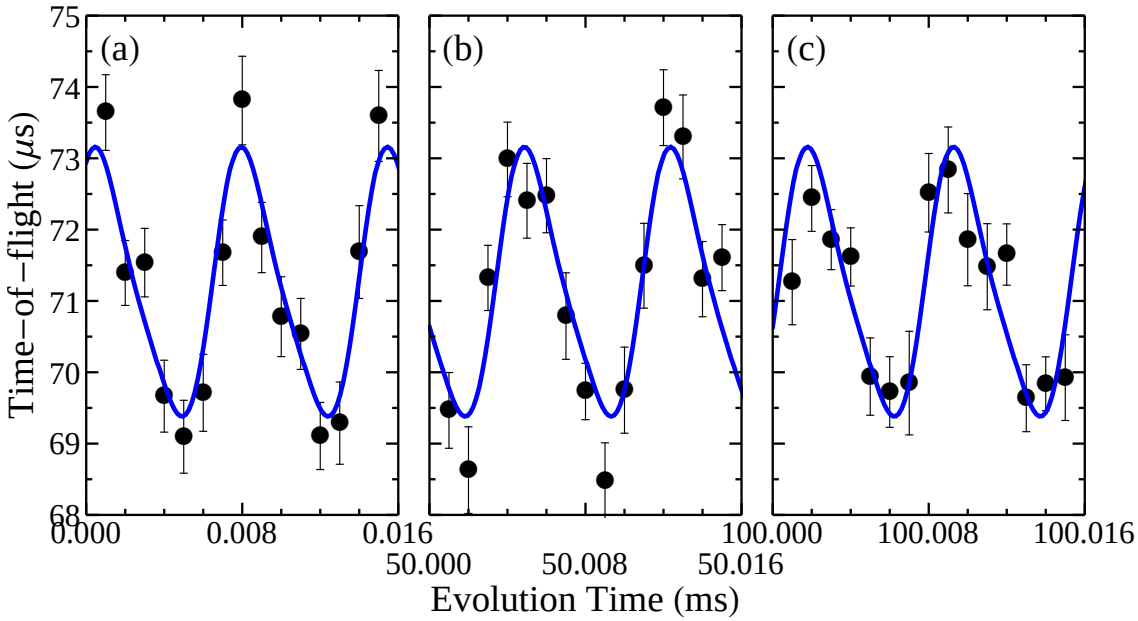


**Figure 3.19:** Axial frequency measurement of $^{39}$K by evolving the axial phase of the ion bunch. The evolution times are (a) $0.001 - 0.015$ ms, (b) $50.001 - 50.015$ ms, (c) $100.001 - 100.015$ ms. The axial frequency was found to be $133508.24\,(18)$ Hz.

motion can be eliminated. Further, large axial oscillations can "wash-out" the measured resonance, affecting the achievable statistical precision of the measurement. By varying both the time when the trap closes and the incoming energy of the ion bunch, it is possible to eliminate nearly all axial oscillations [155].

### 3.3.5 Technical setup

The field strength of the superconducting magnet is 3.7 T, which is nearly half of the average field strength of other on-line Penning trap spectrometers, most having field strengths ranging between 6–9.4 T [149, 193, 194]. To compensate for the low magnetic field strength, highly charged ions can be used.

To prepare the initial magnetron motion, a Lorentz Steerer (LS) is used [195]. This is different from the usual method of dipole excitation at the magnetron frequency. Not only is this dipole excitation time consuming, requiring excitation times of $> 10$ ms, but the RF phase of the magnetron pulse must be locked to the ion capture time [196]. Long excitation times are needed because the magnetron frequency is very low and the driving voltage is limited by the RF amplifier. The RF phase must be locked because ions cannot be injected with zero initial magnetron motion and the magnetron radius after excitation depends on the phase difference

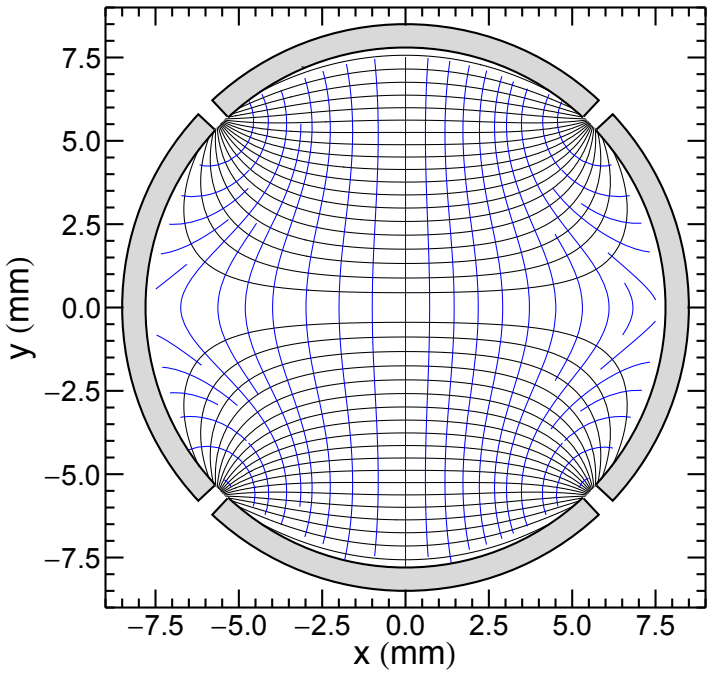


**Figure 3.20:** Lorentz Steerer schematic, with equipotentials [195] (black), and E-field direction lines (blue). Near the centre of the Lorentz steerer, the electric field is almost entirely along the $y$-axis. The top electrode is at 1 V, the bottom electrode is at $-1$ V, and the side electrodes are at 0 V.

between the magnetron motion and RF pulse. The LS is located near the trap, and it is wholly contained in the strong magnetic field of the superconducting solenoid. The LS eliminates this preparation stage by starting the ion on an initial magnetron motion during injection, a development allowing access to nuclides with half-lives below 50 ms. Among others, the LS has allowed TITAN to measure the mass of $^{11}$Li [67], having a half-life of only 8.8 ms, which is the shortest lived nuclide measured in a Penning trap. When an ion passes through the LS it experiences an $\vec{E} \times \vec{B}$ field, causing the ion to drift off axis. Figure 3.20 illustrates the electric potential and field direction for an ion inside the LS. Typically the LS voltages are set such that the ions are injected into MPET with magnetron radii of $\approx 1$ mm. This is much smaller than the 7.6 mm inner radius of the LS, meaning the electric field the ion experiences is nearly unidirectional. The LS can also correct for off axis injection caused by ion optics upstream of the trap. By manipulating the voltages on the four electrodes the ion's initial position can be accurately set. For example, the phase of the magnetron motion can be controlled to within a few degrees [195].

After passing through the LS, the ions must be pulsed down in energy to be captured in the trap, as the transport energy of the ions is typically $\approx 2$ keV, while the trap is held at ground

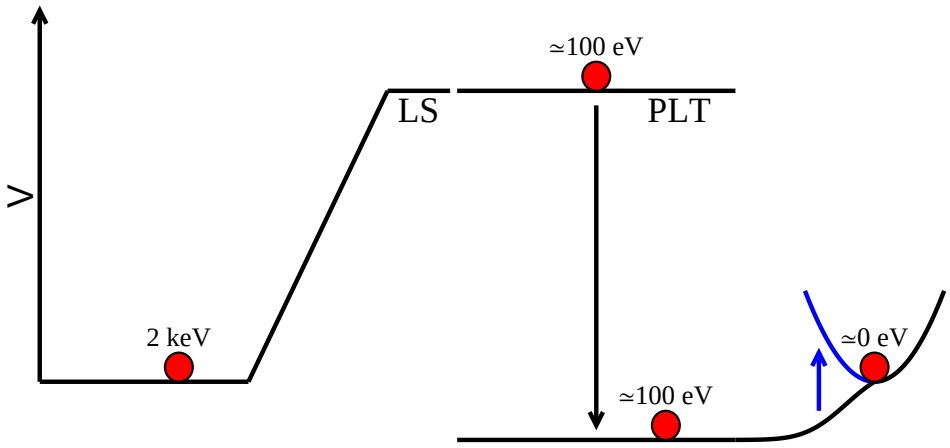


**Figure 3.21:** Schematic of an ion's energy during injection into MPET. The pulsed drift tube (PLT) is pulsed down when ions are passing through, removing nearly all of the transport energy. The ions then climb into the trap, and are captured by changing the potential on the trap end-cap.

potential. A schematic of this is shown in figure 3.21. A long pulsed drift-tube (PLT) acts as an ion energy elevator, removing enough kinetic energy so that the ion when trapped has, at most, a few electron volts of energy. This is an important step, as excess axial energy may "wash-out" the resonance due to an increase in the TOF spread of the extracted ion beam. Optimal injection parameters are found by scanning both the capture time and the lower level of the PLT. A general procedure for optimizing injection is discussed in [155]. However, if one wishes to measure the axial frequency, a slight change of the capture time from the optimal setting induces axial oscillations. Once optimal settings are found, the timings for nuclides near-by in mass can be calculated by a simple scaling of the timings with the mass-to-charge ratio. This is particularly useful when the nuclide of interest is produced at very low rates, as too much time would be needed to optimize the injection.

For the electrode configurations, MPET uses hyperboloids of revolution for the end cap and ring electrodes of the trap. To correct for higher order terms arising both from truncating these electrodes and from holes to allow for injection and ejection, so-called guard electrodes correct for the electrode truncation while correction tubes correct for the holes in the end caps. The characteristic distances are $r_0 = 15$ mm, $z_0 = 11.785$ mm, and $d_0 = 11.21$ mm. Figure 3.22 shows a schematic of the real trap electrodes. Between the ring and end caps a potential difference of 35.75 V is used, with the end caps set to 20 V and the ring set to $-15.75$ V. Determining the correct settings for the correction electrodes is a time consuming process, however, to find the correct settings one can follow the method presented in [198, 155]. Following this proce-

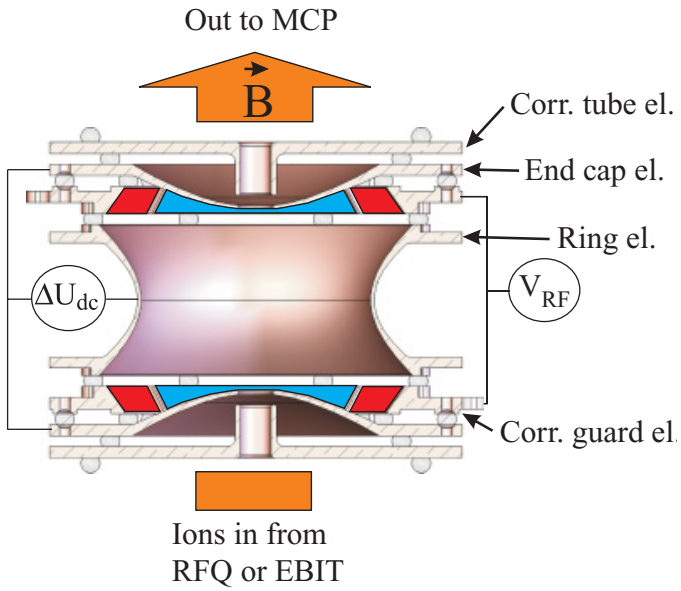


**Figure 3.22:** Schematic of MPET's trap electrodes. The guard electrodes are coloured to match the colour scheme in figure 3.11. The grey circles are sapphire balls that are used to electrically separate the trap electrodes. Figure from [197].

dure, the guard electrodes are set to 0.189 V, while the correction tubes are set to 28.17 V. This procedure only needs to be completed once, as all parameters, including the trap geometry, are kept constant.

After trapping and excitation, the ion is ejected from the trap towards a detector with single-ion sensitivity. MPET uses two detectors, a Micro-Channel Plate (MCP) mounted in-line with the trap and a Daly detector [199] mounted perpendicular to the optical axis [197]. MCP's are $\approx 40\%$ efficient when detecting singly charged ions, while a Daly detector can have efficiencies of $> 90\%$. When an ion impinges on an MCP, it releases electrons from low work function material in one channel of the MCP. These released electrons start a cascade, amplifying the initial signal up to $10^6$ times. If an ion hits in between channels, the probability for a cascade, and detection, is reduced. A Daly detector first impinges the ion beam on a material with a low work function, releasing several electrons for each incoming ion. At TITAN, a plate of naturally anodized aluminium is used, releasing $\approx 3$ electrons for incident ion energies of 5 keV [200]. These released electrons are then accelerated towards another MCP where they are detected. Increasing the initial number of charged particles increases the likelihood that at least one will be detected, leading to a large overall increase in the detection efficiency. The Daly detector was used during the $^{20,21}$Mg experiment, and was found to be two-fold more efficient than the on-axis MCP.

### 3.3.6 Determining the mass

Once an ion's cyclotron frequency has been measured, the mass can be determined provided the magnetic field is well known. This is not possible because the field strength is not constant. It varies with pressure and temperature, and it is slowly decaying due to residual resistance in the superconducting coils. By taking the frequency ratio between two different species these fluctuations can be largely eliminated. In the following, we call one ion the "ion of interest" and the other the "calibrant" or "reference" ion. The frequency ratio $R$ is defined to be

$$R = \frac{\nu_{c,\mathrm{ref}}}{\nu_c} = \frac{q_{\mathrm{ref}}}{q}\frac{m}{m_{\mathrm{ref}}}. \tag{3.61}$$

where $m$ is the mass of the ion. To obtain the atomic mass, we must correct for the missing electrons and their binding energy

$$M = \frac{q}{q_{\mathrm{ref}}} R\left(M_{\mathrm{ref}} - q_{\mathrm{ref}} m_e + B_{e,\mathrm{ref}}\right) + q m_e - B_e \tag{3.62}$$

where $M$ is the atomic mass of the species, $m_e$ is the mass of the electron, and $B_e$ is the total binding energy of the missing electrons. The electron binding energies for singly charged ions are usually quite small, having values between $\approx 5 - 10\,\mathrm{eV}$. In most measurements the statistical uncertainty ($\geq 100\,\mathrm{eV}$) dominates, so the binding energy can be ignored. Quite often, atomic masses are reported in short-hand notation as mass excesses $ME = M - A \cdot u$, where $u$ is the atomic mass unit, defined such that the mass of $^{12}$C is exactly 12 u. The mass excess removes the bulk of the mass that comes from the constituent protons and neutrons, enabling a clearer picture of the differences in binding energy between isobaric nuclides.

While the simple frequency ratio above can largely calibrate the magnetic field, there remains the issue that the two measurements are not performed at the same time. This can be corrected for by performing two reference measurements, one before and one after the measurement of the ion of interest. The reference frequency can be linearly interpolated to the time of the measurement of the ion of interest, removing magnetic field instabilities that are linear in time. Not only does the frequency ratio eliminate magnetic field fluctuations, it also eliminates many other systematic effects.

### 3.3.7 Systematic shifts

Due to many differing effects, the measured cyclotron frequency may be shifted from the true cyclotron frequency. Here we will examine these potential shifts, and assign upper limits on their size. In nearly all cases we will find that the systematic effects are much smaller than

the desired measurement precision. We parametrize the shift in the frequency ratio $\Delta R/R$ by calculating the difference between the measured ratio and the ideal ratio

$$\frac{\Delta R}{R} = \frac{R_{\text{measured}} - R_{\text{ideal}}}{R_{\text{ideal}}}. \tag{3.63}$$

One can see that systematic shift will cancel to high order through this procedure. Assume that the ion of interest and the reference ions have different systematic shifts $\delta\nu_c$ and $\delta\nu_{c,\text{ref}}$. The measured frequency ratio would be

$$R_{\text{measured}} = \frac{\nu_{c,\text{ref}} + \delta\nu_{c,\text{ref}}}{\nu_c + \delta\nu_c} = \frac{\nu_{c,\text{ref}}}{\nu_c} \cdot \frac{1 + \delta\nu_{c,\text{ref}}/\nu_{c,\text{ref}}}{1 + \delta\nu_c/\nu_c} \approx R_{\text{ideal}} \left(1 + \frac{\delta\nu_{c,\text{ref}}}{\nu_{c,\text{ref}}} - \frac{\delta\nu_c}{\nu_c}\right) \tag{3.64}$$

If both ions have the same $m/q$, then the systematic shifts will be close in size, causing the systematics to largely cancel. Thus, we can expect the systematic shifts to be small. To simplify calculations, the shifts are expressed in terms of $\Delta(m/q)$, where $m$ is expressed in atomic mass units, and $q$ is the charge state, or number of removed electrons. Suitable references can always be found, so $\Delta(m/q)$ of 2 or 3 is typical, however, the difference can be as large as 10 or more.

#### 3.3.7.1 Relativistic effect

An ion's velocity in the reduced cyclotron mode is $v_+ = \omega_+\rho_+$, a value depending on the magnetic field strength and radius of the motion. For example in MPET, for a $^{39}K^+$ ion on a 1 mm orbit, the velocity is $v/c \approx 3 \cdot 10^{-5}$, resulting in a relativistic correction factor $\gamma - 1$ of $4.6 \cdot 10^{-10}$. The relativistic cyclotron frequency is given by

$$\omega_c = \frac{qB}{\gamma m}, \tag{3.65}$$

resulting in a measured frequency shift upwards of 0.4 ppb. For heavy SCI, like $^{39}K^+$, the relativistic effect is evidently quite small, and can be neglected. For light SCI or HCI, the relativistic shift can be quite large (several ppb), and must must be corrected for [201].

In the measurements presented here, the relativistic shift can be neglected because the precision of all measurements were $> 80$ ppb.

#### 3.3.7.2 Spatial magnetic field inhomogeneities

Care was taken during the construction of the magnet to ensure the magnetic field was homogeneous in the trapping region, but some inhomogeneities still exist due to the finite size of the solenoid, and by inhomogeneities caused by the material used to construct the trap, vacuum

vessel, etc. The frequency shift is given by [202]

$$\Delta\nu_c = \beta_2 \left( \left(z^2 - \rho_+^2\right) - \frac{\nu_-}{\nu_c} \left(\rho_+^2 + \rho_-^2\right) \right) \tag{3.66}$$

where $\beta_2$ is the quadrupole coefficient of the magnetic field inhomogeneity, and $z$ is the amplitude of the axial motion. For TITAN the upper limit on the shift in the frequency ratio is [198]

$$\frac{\Delta R}{R} < 4.3 \cdot 10^{-10} \Delta(m/q). \tag{3.67}$$

#### 3.3.7.3 Non-harmonic imperfections of the trapping potential

The electric potential of the trap is not a pure quadrupole field, because higher order terms arise both from truncating the trap electrode surfaces, and from the holes in the end caps for injecting and ejecting ions. These higher order terms are corrected for by adding electrodes to compensate these finite size effects. "Guard" electrodes are added between the end cap and ring electrodes to correct for the electrode truncation, while "tube" electrodes are added near the end caps to correct for the injection and ejection holes. These electrodes are shown in figure 3.22. A general procedure to minimize these non-harmonic potentials was developed in [155] to determine the optimal trap settings. The frequency shift is less than

$$\frac{\Delta R}{R} < 3.6 \cdot 10^{-10} \Delta(m/q). \tag{3.68}$$

#### 3.3.7.4 Harmonic distortion and magnetic field misalignment

Precision machining and setting of the trap electrodes is a difficult procedure. Any distortion of the ring electrode from cylindrical symmetry can lead to a frequency shift. This distortion is parametrized by an ellipticity factor $\eta$. Further, the trap axis may be at an angle $\theta$ with respect to the magnetic field axis. Both of these misalignments lead to a frequency shift of [203]

$$\Delta\nu_c = \left( \frac{9}{4}\theta^2 - \frac{1}{2}\eta^2 \right) \nu_-. \tag{3.69}$$

The shift in the frequency ratio is then given by [203]

$$\frac{\Delta R}{R} = \left( \frac{9}{4}\theta^2 - \frac{1}{2}\eta^2 \right) \left( \frac{\Delta A}{A_{\text{ref}}} \right) \left( \frac{\nu_-}{\nu_{+,\text{ref}}} \right) \tag{3.70}$$

where $A$ is the mass number. The shift can be estimated by considering what the maximum machining tolerances in the components holding the trap together are. The largest potential shift arises from the maximal tolerances in the sapphire balls that separate the trap electrodes (see figure 3.22). The maximum angle is then estimated to be $\theta \approx 4.2 \cdot 10^{-3}$ rad [198]. The shift could be of the order

$$\frac{\Delta R}{R} < 4.3 \cdot 10^{-9} \Delta(m/q). \tag{3.71}$$

This is certainly a very conservative estimate, since it is unlikely that sapphire balls with opposite tolerances would be placed to give the maximal deviation. The alignment and distortion parameters can be measured through a specific combination of the eigenfrequencies [203]

$$\left(\frac{9}{4}\theta^2 - \frac{1}{2}\eta^2\right) \approx \frac{2\omega_- \omega_+}{\omega_z^2} - 1. \tag{3.72}$$

Using the measured eigenfrequencies in table 3.2, and using a conservative error of 0.2 Hz for the magnetron frequency, the frequency ratio shift becomes

$$\frac{\Delta R}{R} = -0.6(17) \cdot 10^{-9} \Delta(m/q). \tag{3.73}$$

Again, shifts on the order of 1 ppb are much smaller than the precision usually measured in an on-line experiment.

#### 3.3.7.5 Ion-ion interactions

Ideally only a single ion would be trapped at a time, but quite often multiple ions, either of the same species or of a contaminant species, will be trapped simultaneously. These additional charges not only modify the potential inside the trap, but they also interact with each other through their mutual Coulomb interactions. Through these interactions, the observed eigenfrequencies may be shifted, leading to a systematic shift in the measured cyclotron frequency. These shifts have been observed, and they vary linearly with the number density, assuming the same charge state [190]. Other shifts arise due to the simultaneous trapping of different species [191].

To correct for these shifts, one can determine the cyclotron frequency as a function of the number of detected ions and extrapolating to the detector efficiency, correcting for both the ion-ion interaction and the efficiency of the detector. Such an analysis is called a "count-class" analysis [204], and it can be applied when a total of greater than $\approx 1000$ ions have been collected in a resonance spectrum. Trap extractions are divided into classes based on the number of ions detected. A typical count-class analysis for $^{23}$Na with 4 count-classes is shown

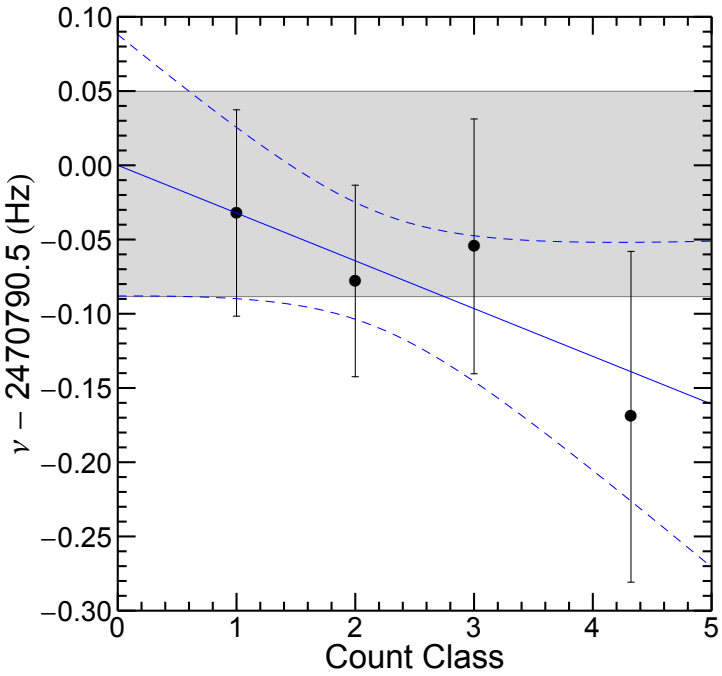


**Figure 3.23:** Count class analysis for $^{23}$Na with four count classes. The dashed lines are the $\pm 1\sigma$ line fits, while the filled area show the error band when the count class is extrapolated to the detector efficiency. A typical detector efficiency of 0.6 was used.

in figure 3.23. The classes are divided in such a way that each combined class has as close to an equal number of ions as possible. In figure 3.23, the first, second, and third classes contain extraction events where 1, 2, or 3 ions were detected, while the fourth class contains all events with 4 or more detected ions. The position of the class on the $x$-axis is taken to be the centre of gravity of the class. In the fourth class of figure 3.23, it is close to 4 because most events in that class have 4 detected ions. A linear fit is done to the count-class data, and is extrapolated to the detector efficiency. In this way the cyclotron frequency when one ion is in the trap can be extracted. In figure 3.23, the solid blue line is a linear fit to the count-class data, while the dotted blue lines show the $\pm 1\sigma$ error bands. In cases where statistics are too low, the difference between the analysis with only one detected ion to that of an analysis with all detected ions can be used. The difference is taken to be the systematic error.

In the present measurements, a count-class analysis is done for each measured isotope.

#### 3.3.7.6 Non-linear magnetic field fluctuations

As mentioned at the beginning of this section, the cyclotron frequency of both the ion of interest and the calibrant ion are measured. However with TITAN, it is not possible to measure the

frequency of both ions simultaneously. In the time between measurements, the magnetic field may decay, or otherwise fluctuate, in a non-linear manner, the result of which would be a systematic shift of the measured mass. In order to minimize these potential shifts, the time between reference measurements is usually kept below one hour. The effect of changing the time between the reference measurements was determined to be $\delta v/v = 0.04(11)$ ppb/h [201]. This is below the sensitivity of the present measurements, and is not included in the analysis herein.

# Chapter 4

# Results and discussion

In this chapter we discuss the results of the mass measurements of $^{51,52}$Ca, $^{51}$K, and $^{20,21}$Mg. The Ca and K mass values, along with the recent measurements by ISOLTRAP [59], will be compared to existing phenomenological interactions and interactions based on $\chi$EFT, with the aim of elucidating the ground state structure near the $N = 34$ shell closure. The Mg mass values will be used to test the IMME in the $A = 20$ and 21 isotopic chains. This will be compared to the IMME calculated with the USDA/B interactions, and $\chi$EFT based calculations. The $\chi$EFT calculations are particularly interesting, as they are the first $\chi$EFT based calculations to included both active neutrons and protons in the valence space.

The measurements were completed in three separate experiments. First, beams of $^{51,52}$Ca were produced by bombarding a Ta target with 75 $\mu$A of 480 MeV protons, and ionized with TRILIS. Second, the $^{51}$K beam was made with a $UC_x$ target with 1.4 $\mu$A of protons, with a surface ion source. Third, beams of $^{20,21}$Mg were produced by bombarding a SiC target with 40 $\mu$A of protons, and were ionized using IG-LIS. Yields are presented in table 4.1.

**Table 4.1:** Ion yields [205] for $^{51,52}$Ca, $^{51}$K and $^{20,21}$Mg.

| Species | $T_{1/2}$ | Yield (ions/s) |
|---|---|---|
| $^{51}$Ca | 10.0 s | $1.4 \cdot 10^4$ |
| $^{52}$Ca | 4.6 s | $1.3 \cdot 10^3$ |
| $^{51}$K | 365 ms | $\approx 75$ |
| $^{20}$Mg | 90.8 ms | 50 |
| $^{21}$Mg | 122 ms | $2.7 \cdot 10^3$ |

## 4.1 Existing data

### 4.1.1 $^{51}$Ca

Creating beams of neutron rich Ca isotopes has been a challenge for rare-beam facilities. Because of this, mass measurements in this region have generally relied on multi-nucleon transfer reactions. The mass of $^{51}$Ca, as of the Atomic Mass Evaluation 2003 (AME03) [206], is derived from three-neutron-transfer reactions, using beams of $^{14}$C or $^{18}$O on a $^{48}$Ca target [207, 208, 209, 210]. Additionally, two TOF mass measurements of $^{51}$Ca agree with each other [211, 212], but disagree at the $\approx 1\sigma$ level with the reaction based experiments. A more recent measurement at GSI using the fragment separator and experimental storage ring (FRS-ESR) [213], agrees with the TOF measurements, but is in strong disagreement with the reaction values. Figure 4.1 summarizes these results, with the TITAN value for comparison.

First, we will examine the reaction based measurements. Three-nucleon transfer reactions are quite complicated, due to the possibility of multiple steps during the transfer, leading to low cross-sections, and resulting in low statistics. Further, due to the possibility of contaminants in the target material, it is possible that observed states in the outgoing reaction channel may be misidentified. As all four reaction experiments used enriched $^{48}$Ca targets, the residual $^{40}$Ca contamination resulted in large backgrounds. Other target contaminants include $^{16}$O and $^{14}$C. In reactions on these contaminants, the outgoing projectile-like particle ($^{15}$O or $^{11}$C) have energies that are close to the ground state energy of the reaction on $^{48}$Ca, however, the spectrometers used in these reactions were capable of separating these reactions. Because of this, it is unlikely that a peak was misidentified. Another potential source of error in these reactions is false calibration of the reaction spectrometer. In order to calibrate the spectrometer, reactions on well known targets are performed. This further eliminates the possibility that a contaminant reaction peak was identified as belonging to the reaction of interest.

Beyond the general disagreement of the reaction experiments on the ground state mass of $^{51}$Ca, none of the experiments agree on the energies of the excited states. Two recent measurements also corroborate the conclusion that these early multi-nucleon transfer reactions identified the wrong state as the ground state. One measurement used deep inelastic collisions of $^{238}$U on a target of $^{48}$Ca [214], while the other used the $\beta$-decay of $^{51}$K and the $\beta - n$ decay of $^{52}$K [215]. These measurements agree with each other, but disagree with the values extracted from the above reaction-based experiments. For example, in [210] the lowest excited state was found to be $1.01(11)$ MeV, while in the two recent measurements the lowest excited state was found to be $1.72$ MeV. Further, the energy levels from the recent experiments agree well with

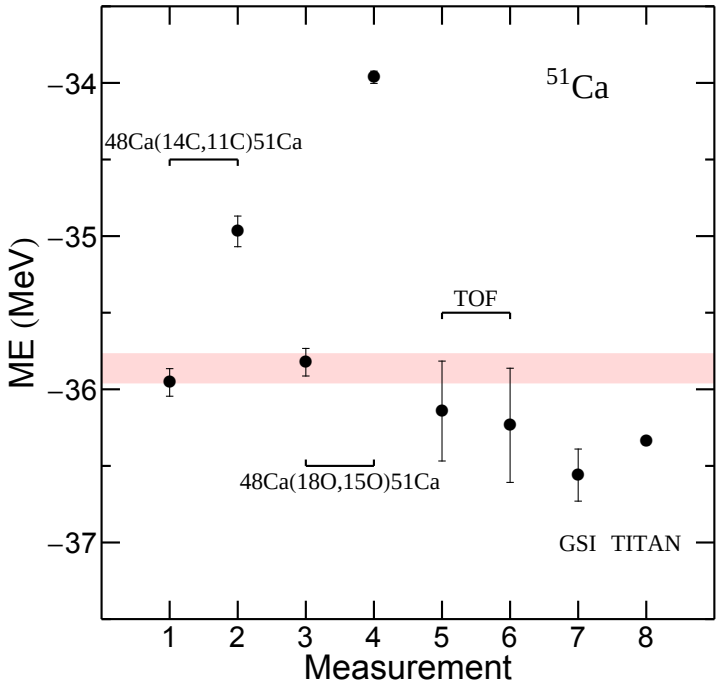


**Figure 4.1:** All $^{51}$Ca mass measurements, as compared to the TITAN value. Only two reaction based measurements agree with each other, while the other two are in great disagreement. The TOF measurements agree with each other, and are in slight disagreement with the reaction measurements. The red band shows the AME03 [85] value. The TITAN value is shown for comparison.

calculations done with both KB3G and GXPF1A.

### 4.1.2 $^{52}$Ca

In the case of $^{52}$Ca, only two prior mass measurements exist and are included in the Atomic Mass Evaluation 2003 [206]. The first measurement comes from a $\beta$-end point measurement [216], while the second comes from a TOF measurement [211]. The measurements strongly disagree with each other. The mass excess from the $\beta$-decay measurement is $-35.75(32)$ MeV, while the TOF measurement is $-32.5(5)$ MeV. In the AME2003, the evaluators chose to disregard the $\beta$-end point measurement, taking the value of the TOF measurement, and slightly inflating the error bar. The end-point measurement also determined the $Q$-value of the $^{52}$Sc $\rightarrow^{52}$ Ti, allowing for a determination of the mass excess of $^{52}$Ca. However, if any of the intermediate measurements were wrong, the value for $^{52}$Ca would suffer large systematic shifts. Figure 4.2 shows the previous measurements together with our TITAN value.

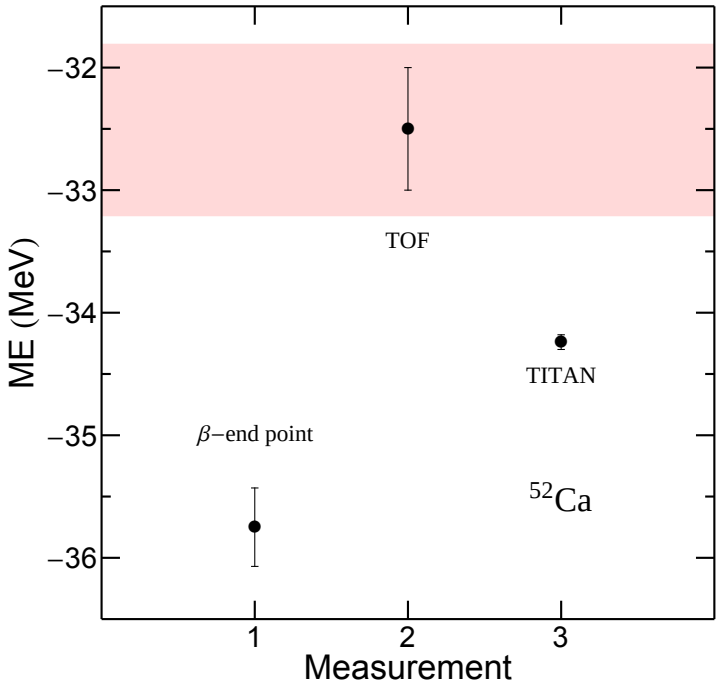


**Figure 4.2:** All $^{52}$Ca mass measurements. All measurements disagree. The red band shows the AME03 [85] value.

### 4.1.3 $^{53,54}$Ca

The masses of $^{53,54}$Ca were measured for the first time using the multi-reflection time-of-flight device at ISOLTRAP [59]. ISOLTRAP is a multi-trap experiment at the ISOLDE/CERN facility, which employs a Penning trap and a recently added MR-TOF system for isobar separation and mass measurement. The measured mass excesses are $-229387.8(43.3)$ keV for $^{53}$Ca and $-225161.0(48.6)$ keV for $^{54}$Ca. ISOLTRAP also measured the masses of $^{51,52}$Ca in a Penning trap and the mass of $^{52}$Ca with the multi-reflection device. In each case, the masses agree well with the values measured with TITAN. This lends credence to the accuracy of the mass values for $^{53,54}$Ca.

### 4.1.4 $^{51}$K

The mass of $^{51}$K has not been measured prior to the present measurements. The mass value tabulated in the AME03 is based on observed trends in the mass surface [206]. In general, the mass surface varies slowly and regularly as a function of $N$ and $Z$. Rapid changes in this regularity signals changes in structure, structure such as new sub-shell closures or deformation. Quite often, these predictions are accurate, agreeing well with new experimental data [15].

The TITAN mass excess of $-22516(13)$ keV agrees at the $1\sigma$ level with the AME03 value of $-22000(500)$ keV.

### 4.1.5 $^{20,21}$Mg

Prior to our TITAN mass measurements, the mass of $^{20}$Mg was measured using the $^{24}$Mg($^{4}$He,$^{8}$He)$^{20}$Mg reaction [217, 218], while the mass of $^{21}$Mg was measured using the $^{24}$Mg($^{3}$He,$^{6}$He)$^{21}$Mg reaction [219, 220]. For $^{20}$Mg the measured $Q$-values were -60900(210) and -60677(27) keV, and for $^{21}$Mg the measured $Q$-values were -27488(40) and -27512(18) keV. In each case, the measurements are in good agreement with each other.

#### 4.1.5.1 Isospin multiplet energy levels

Determining the energy level of an isospin multiplet member relies on knowing both the ground-state and excited state energies accurately. Except in the cases discussed below, the excitation energies will be taken from the National Nuclear Data Center [114], while the ground-state masses will be taken from the AME2012 [69]. The energy of the $J^{\pi} = 0$, $T = 2$ state in $^{20}$Na depends on knowing the proton separation energy. Recent measurements of the ground-states of $^{20}$Na and $^{19}$Ne, led to an improved proton separation energy of $2190.1(11)$ keV. Combining this with a new excitation energy measurement with the value compiled in [221], leads to an average value of $6524.0(98)$ keV, a value that is shifted by 10 keV as compared to the tabulated value [114]. In $^{21}$Mg, a new measurement of the $J^{\pi} = 1/2^{+}$ state was completed [222] which, when averaged with the NNDC [114] value, yields $200.5(28)$ keV.

## 4.2 Discussion and measurements from this study

To determine the atomic masses presented here, we follow the procedure described in section 3.3.6. For $^{51}$Ca, $^{51}$V was used as a reference, for $^{52}$Ca, $^{58}$Ni and $^{52}$Cr were used as references in two separate measurements, while for $^{20,21}$Mg, $^{23}$Na was used as a reference. In all cases, the mass of the reference is much better known than the precision achieved in the experiment. Because high precision was not required in these measurements, the standard one-pulse quadrupole excitation was used. Further, the measurements were completed with singly charged ions, as the gain in precision from charge breeding were not needed. The Ca and K measurements will be compared to the values from AME03, as previous measurements in [223], and the measurements presented here, dominate the data in both AME11 and AME12.

In order to correct for the ion-ion interaction arising from potential contaminants simultaneously trapped with the ion of interest, a "count-class" analysis [204] (section 3.3.7.5) was

conducted. In the case of the $^{51,52}$Ca and $^{51}$K measurements, large amounts of contamination from V and Cr were observed. This contamination was removed from the trap via dipole cleaning.

For the $^{20,21}$Mg measurements a count-class analysis was not strictly needed, because the IG-LIS blocked nearly all contaminants from being ionized. However, to be conservative a count-class analysis was done, and the corresponding errors were folded into the total uncertainty. Enough statistics were collected so that the count-class error was included in the statistical analysis for $^{21}$Mg, while for $^{20}$Mg the difference between the analyses with one detected ion and with all detected ions yielded a systematic error of 38 ppb. Because these results are of a higher precision than the Ca and K measurements we also include the conservative harmonic distortion and magnetic field misalignment shift of $4.3\Delta(m/q)$ ppb, resulting in systematic errors of 9.6 ppb for $^{21}$Mg and 12.9 ppb for $^{20}$Mg.

### 4.2.1 Calcium and Potassium at $N = 32$

Typical resonances for $^{51,52}$Ca are shown in figure 4.3. For $^{51}$Ca, the measured mass excess of $-36339(23)$ keV is in disagreement with the AME03 value of $-35863(94)$ keV, differing by $476(97)$ keV. As shown in figure 4.1, this result is in agreement with the TOF based measurements, but is in strong disagreement with the 4 reaction based measurements. Recently, ISOLTRAP also measured the mass of $^{51}$Ca [59], obtaining a value of $-36332.07(58)$ keV, which agrees with our measurement.

For $^{52}$Ca, the measured mass excess of $-34245(61)$ keV disagrees with the AME03 value of $-32509(699)$ keV. The TITAN mass value is 1.74 MeV more bound than the AME03 value. This is comparable to the deuteron's binding energy of 2.22 MeV. ISOLTRAP has also measured $^{52}$Ca, obtaining a value of $-34266.02(71)$ keV [59], which also agrees will with the TITAN measurement.

These measurements, combined with the measurement of $^{51}$K, create much more binding leading up to the sub-shell closure at $N = 32$. This is quite significant, and is in line with the observed high excitation energy of the E($2^+$) state in $^{52}$Ca [118]. Figure 4.4 shows the $S_{2n}$ values tabulated in AME03, the TITAN values and the recent ISOLTRAP values. The values for $^{50}$Ca and $^{48-50}$K are from a previous TITAN measurement campaign [223]. The TITAN and ISOLTRAP mass values clearly show a sub-shell closure at $N = 32$, using the previous explained signature for the behaviour.

Next, we examine if theory is able to reproduce these results. Figure 4.5 shows the $S_{2n}$ energies for the calcium chain, while figure 4.6 shows the difference between the experimentally measured and theoretical values. The NN+3N(MBPT) was calculated in the extended $pfg_{9/2}$

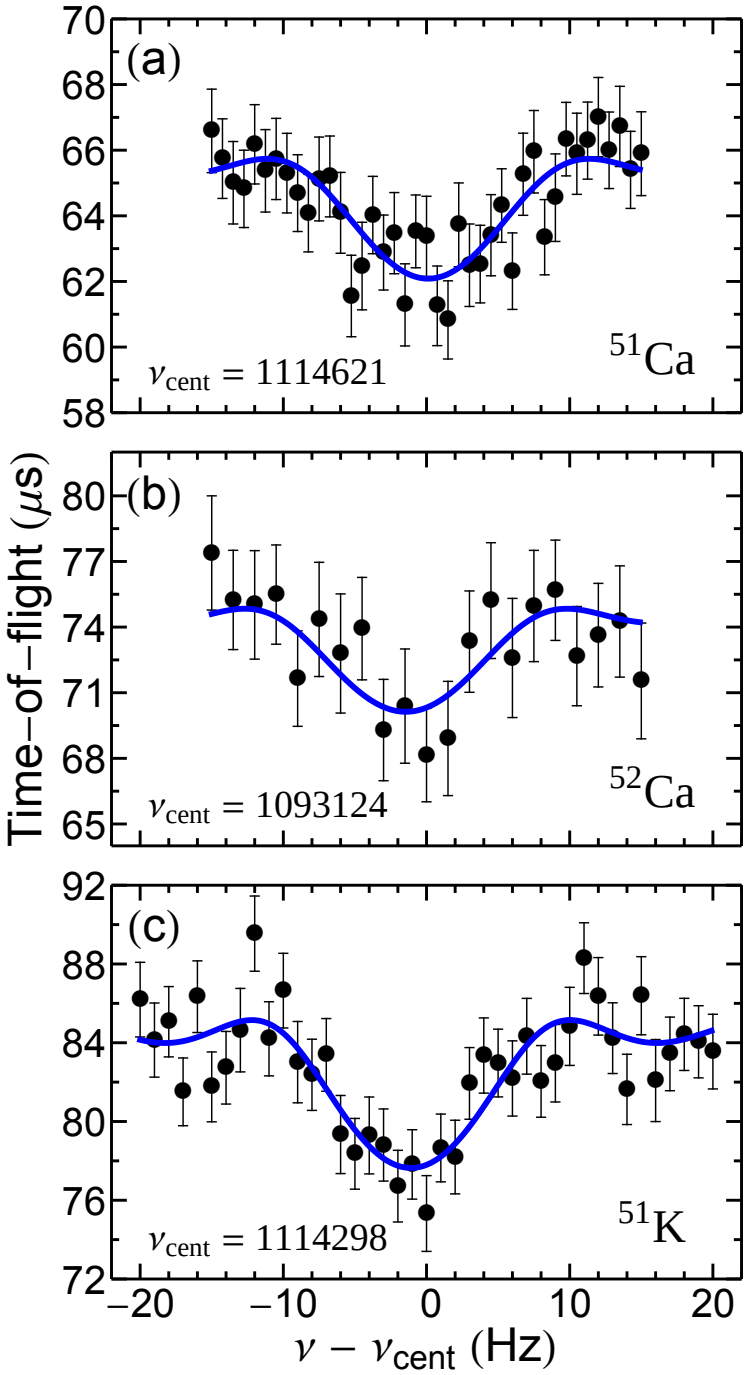


**Figure 4.3:** Typical TOF-ICR resonances (as in figure 3.17) of $^{51,52}$Ca and $^{51}$K. The blue line is a fit of the theoretical line shape [182].

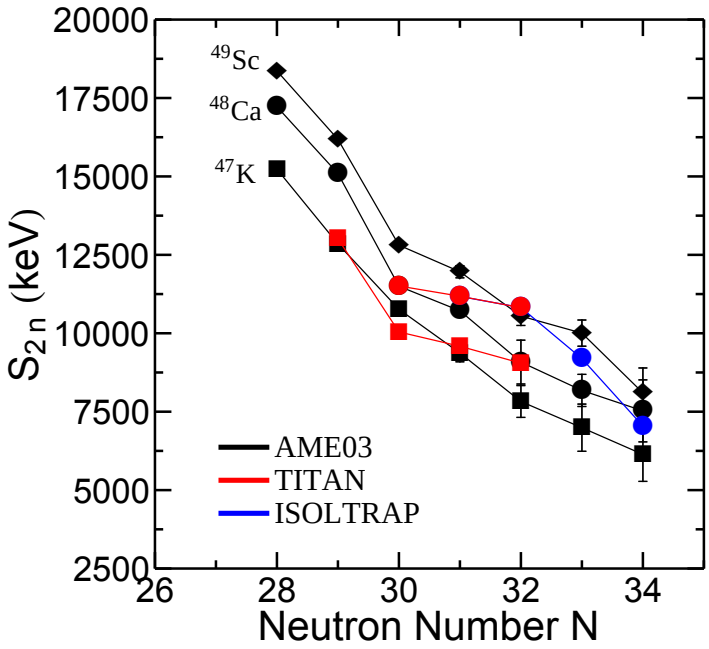


**Figure 4.4:** $S_{2n}$ for the Ca, K and Sc isotopic chains near $N = 32$. Points in black are those tabulated in AME03, the red points are the TITAN measurements, and the blue points show the recent ISOLTRAP measurements [59]. The values for $^{50}$Ca and $^{48-50}$K are from a previous TITAN measurement campaign [223].

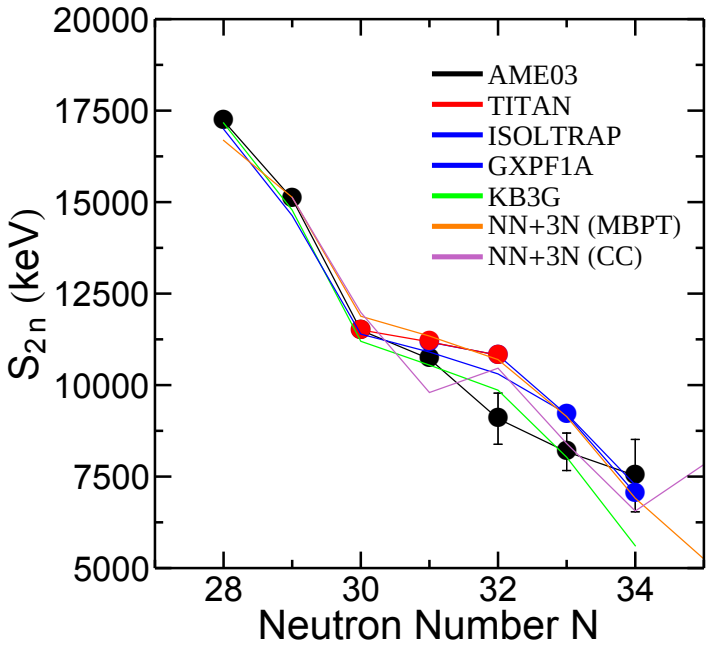


**Figure 4.5:** $S_{2n}$ energies for Ca comparing theory to the TITAN and ISOLTRAP values. Calculations with the GXPF1A and NN+3N(MBPT) agree well with the experimental data.

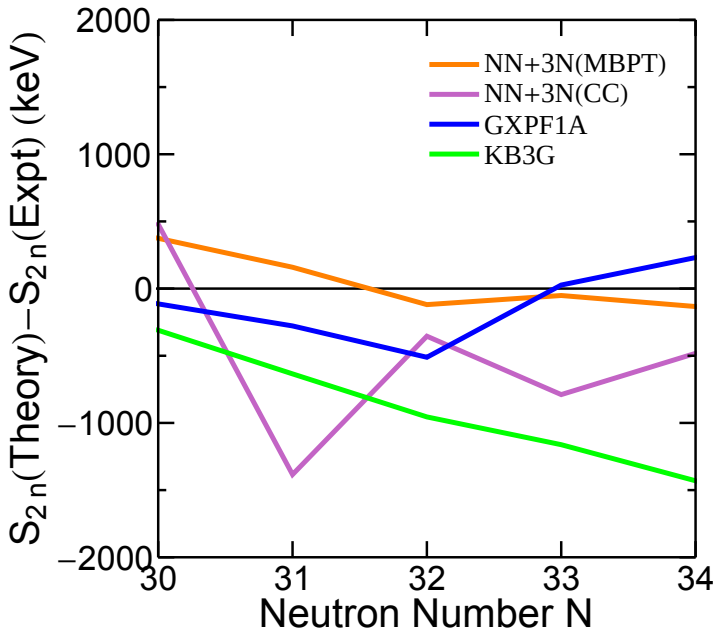


**Figure 4.6:** Difference between calculated and experimental $S_{2n}$ energies. The NN+3N(MBPT) calculation agrees well with the experimental values.

valence space, on top of a closed $^{40}$Ca core. The NN forces are included at next-to-next-to-next-to leading order (N$^3$LO), while the 3N forces are included at N$^2$LO. For the 3N interaction, the short-range coupling constants were fit to the binding energy of $^3$H and the charge radius of $^4$He [224]. The dominant component of the 3N interaction amongst the valence neutrons is due to the long range, two-pion exchange component of the 3N force [58, 119]. In the CC calculation, the chiral NN interaction was included at N$^2$LO, while a schematic 3N interaction was included by integrating one nucleon in the leading order 3N force over the Fermi momentum in symmetric nuclear matter [120]. The short range couplings were adjusted to reproduce the binding energies of $^{48,52}$Ca. The calculation is done using the CCSD approximation, and includes 3-particle-3-hole excitations perturbatively within the Λ-CCSD(T) approach [225]. The NN+3N(MBPT) calculation reproduces the experimental values quite well, while the GXPF1A calculation is in fair agreement. The CC and KB3G calculations have much larger deviations, with both the CC and KB3G calculations consistently underbinding, as compared to experiment. As already shown in figure 2.7, both the NN+3N(MBPT) and CC calculations are able to reproduce the measured E(2$^+$) in $^{54}$Ca, while the phenomenological interactions GXPF1A and KB3G do not. Mass measurements thus provide an alternative way of differentiating between the models. Here, the calculations using NN+3N(MBPT) seems to provide a better description than the CC calculations or the phenomenological interactions.

**Table 4.2:** Measured mass values for $^{51,52}$Ca, $^{51}$K, and $^{20,21}$Mg compared with the atomic mass evaluation [85, 69]. The Ca and K values are compared to AME03, while the Mg values are compared to AME12.

| Nuclide | Reference | $T_{1/2}$ | $T_{RF}$ (ms) | Frequency Ratio $r$ | ME (keV) | $\mathrm{ME_{AME}}$ (keV) | $\Delta$ME (keV) |
|---|---|---|---|---|---|---|---|
| $^{51}$Ca | $^{58}$Ni | 10.0 (8) s | 77 | 0.87961718 (42) | −36339. (23) | −35863. (94) | 476. (97) |
| $^{52}$Ca | $^{58}$Ni | 4.6 (3) s | 77 | 0.89691649 (187) | −34260. (101) | −32509. (699) | 1750. (700) |
| $^{52}$Ca | $^{52}$Cr | 4.6 (3) s | 77 | 1.00043782 (158) | −34236. (76) | −32509. (699) | 1730. (700) |
| $^{52}$Ca average | | | | | −34245. (61) | −32509. (699) | 1740. (700) |
| $^{51}$K | $^{51}$V | 365 (5) ms | 77 | 1.00062561 (28) | −22516. (13) | −22002. (503) | 510. (500) |
| $^{20}$Mg | $^{23}$Mg | 90 (6) ms | 97 | 0.870765248 (87) | 17477.7 (18) | 17559. (27) | 81. (27) |
| $^{21}$Mg | $^{23}$Mg | 122 (2) ms | 97 | 0.913956913 (35) | 10903.85 (74) | 10914. (16) | 10. (16) |

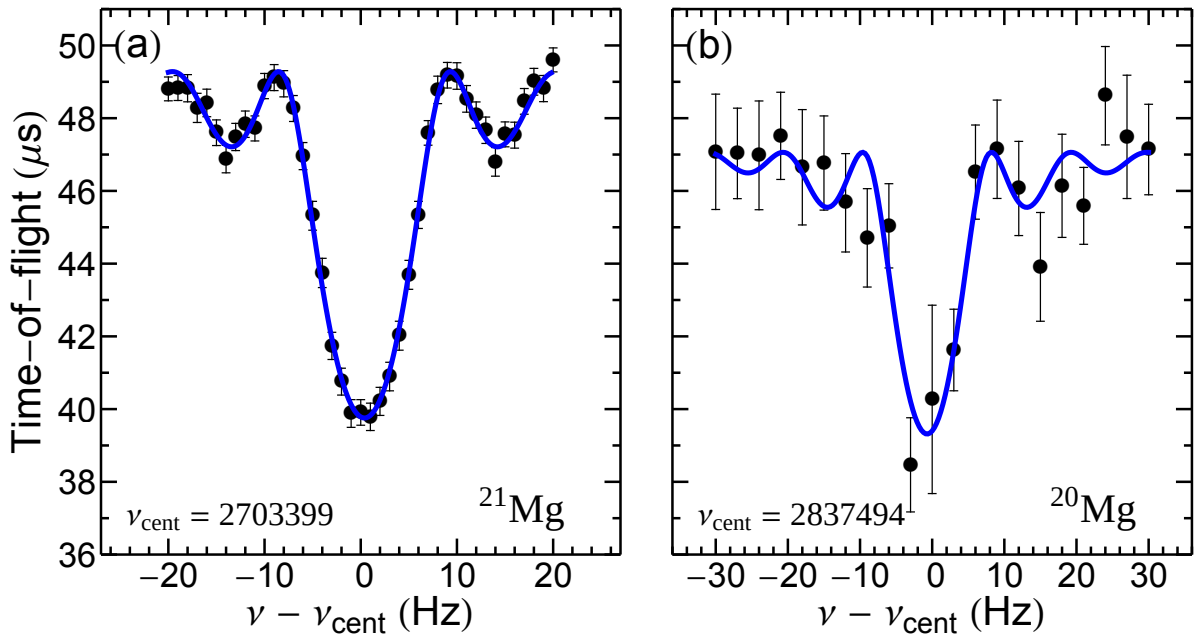


**Figure 4.7:** Typical TOF-ICR resonances (as in figure 3.17) for $^{20,21}$Mg. The blue line is a fit of the theoretical line shape [182].

### 4.2.2 $A = 20, 21$ isobaric multiplet mass equation

Resonances for $^{20,21}$Mg are shown in figure 4.7. The measured mass excess of 10903.85(74) keV for $^{21}$Mg agrees with the tabulated AME12 value of 10914(16) keV, however, the measured uncertainty has been improved by over an order of magnitude. The measured mass excess of 17477.7(18) keV for $^{20}$Mg disagrees with the tabulated AME12 value of 17559(27) keV at the $3\sigma$ level, with the uncertainty being improved by an order of magnitude. The measured values are summarized in table 4.2.

Table 4.3 summarizes the fit results of the quadratic and quartic forms of the IMME for the $A = 20$ and 21 multiplets. For each multiplet the $\chi^2$ of the fit increased as compared to the values tabulated in [129]. For the $A = 20$ multiplet, nearly all of the uncertainty now resides in the excitation energy of the $T = 2$ state in $^{20}$Na. The $\chi^2$ of the quadratic fit increased from 1.1 to 10.2, an increase of nearly an order of magnitude. The best fit is obtained with the cubic fit,

**Table 4.3:** Extracted IMME parameters for the $A = 20$ and 21 multiplets. Mass excesses are taken from [69] and excitation energies $E_x$ from [114] and [226], except where noted. Also shown are the $d$ and $e$ coefficients for cubic and quartic fits and the $\chi^2$ values of the fit. Shell model calculation results using the USDA/B plus INC interactions are presented.

**Table 4.3:** Continued from previous page.

| Nuclide | $T_z$ | ME(g.s.) (keV) | $E_x$ (keV) |
|---|---|---|---|
| $A = 20$, $J^\pi = 0^+$, $T = 2$ | | | |
| $^{20}$O | +2 | 3796.17 (89) | 0.0 |
| $^{20}$F | +1 | -17.45 (3) | 6519.0 (30) |
| $^{20}$Ne | 0 | -7041.9306 (16) | 16732.9 (27) |
| $^{20}$Na | -1 | 6850.6 (11) | 6524.0 (97) [a] |
| $^{20}$Mg | -2 | 17477.7 (18) [b] | 0.0 |

| Ref. | $a$ (keV) | $b$ (keV) | $c$ (keV) | $\chi^2$ |
|---|---|---|---|---|
| This Work | 9689.79 (22) | -3420.57 (50) | 236.83 (61) | 10.2 |
| Ref. [129] | 9693 (2) | -3438 (4) | 245 (2) | 1.1 |

| Fit | $d$ (keV) | $e$ (keV) | $\chi^2$ |
|---|---|---|---|
| Cubic | 2.8 (11) | - | 3.7 |
| Quartic Only | - | 0.89 (12) | 9.9 |
| Quartic | 5.4 (17) | −3.5 (18) | - |
| USDA | −0.1 | - | |
| USDA | - | −1.7 | |
| USDB | −0.1 | - | |

| $A = 21$, $J^\pi = 5/2^+$, $T = 3/2$ | | | |
|---|---|---|---|
| $^{21}$F | +3/2 | -47.6 (18) | 0.0 |
| $^{21}$Ne | +1/2 | -5731.78 (4) | 8859.2 (14) |
| $^{21}$Na | -1/2 | -2184.6 (3) | 8976.0 (20) |
| $^{21}$Mg | -3/2 | 10903.85 (74) [b] | 0.0 |

| Ref. | $a$ (keV) | $b$ (keV) | $c$ (keV) | $\chi^2$ |
|---|---|---|---|---|
| This Work | 4898.4 (13) | -3651.36 (63) | 235.00 (77) | 28.0 |
| Ref. [129] | 4894 (1) | -3662 (2) | 243 (2) | 3.0 |

| Fit | $d$ (keV) | $\chi^2$ |
|---|---|---|
| Cubic | 6.7 (13) | - |
| USDA | −0.3 | |
| USDB | 0.3 | |

| $A = 21$, $J^\pi = 1/2^+$, $T = 3/2$ | | | |
|---|---|---|---|
| $^{21}$F | +3/2 | -47.6 (18) | 279.93 (6) |
| $^{21}$Ne | +1/2 | -5731.78 (4) | 9148.9 (16) |
| $^{21}$Na | -1/2 | -2184.6 (3) | 9217.0 (20) |
| $^{21}$Mg | -3/2 | 10903.85 (74) [b] | 200.5 (28) [c] |

| Ref. | $a$ (keV) | $b$ (keV) | $c$ (keV) | $\chi^2$ |
|---|---|---|---|---|
| This Work | 5170.4 (14) | -3633.6 (10) | 220.9 (10) | 9.7 |
| Ref. [129] | 5171 (10) | -3617 (2) | 217 (2) | 3.5 |

| Fit | $d$ (keV) | $\chi^2$ |
|---|---|---|
| Cubic | −4.4 (14) | - |
| USDA | −1.2 | |
| USDB | 1.9 | |

[a] Average of Refs. [227, 221]
[b] Present work
[c] Average of Refs. [226, 222]

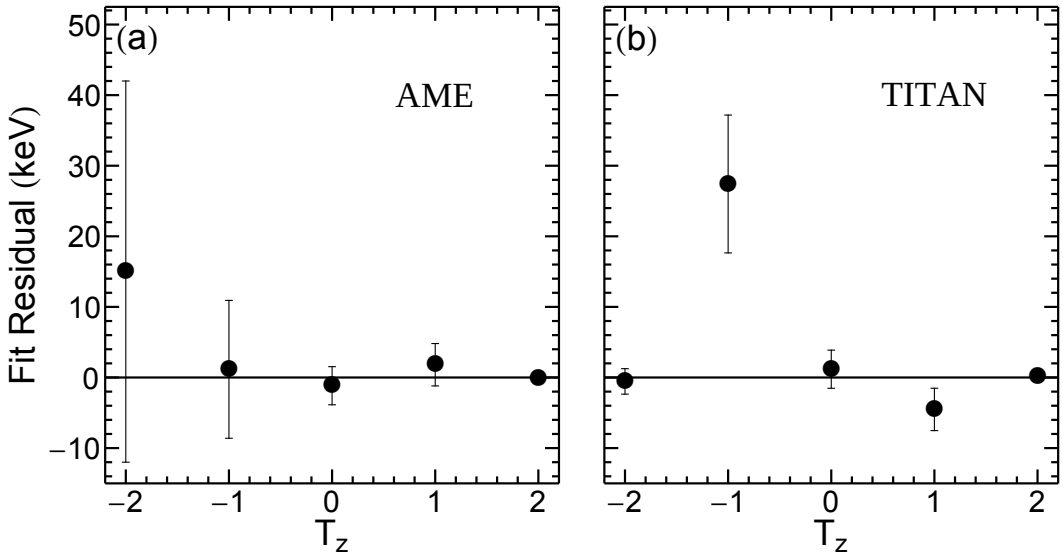


**Figure 4.8:** $A = 20$ $J^\pi = 0^+$ $T = 2$ quadratic residuals for (a) the AME2012 [69] mass values, and (b) using the TITAN mass value for $^{20}$Mg. The large error bar for $^{20}$Na ($T_z = -1$) is due to the uncertainty in the excitation energy. Excitated state energies are listed in table 4.3

resulting in $d = 2.8(11)$ keV and a $\chi^2$ of 3.7. A quadratic only fit results in $e = 0.89(12)$ keV, and a $\chi^2$ of 9.9.

For $A = 21$ there are two $T = 3/2$ isobaric multiplets, a ground state multiplet with $J^\pi = 5/2^+$ and an excited state multiplet with $J^\pi = 1/2^+$. For the $J^\pi = 5/2^+$ multiplet, the $\chi^2$ of the quadratic fit increased from 3 to 28.0, an increase of nearly an order of magnitude. For the $J^\pi = 1/2+$ multiplet, the $\chi^2$ of the quadratic fit increased from 3.5 to 9.7. According to this, the IMME has failed in both instances. Large cubic terms are required for both multiplets, taking the values $d = 6.7(13)$ kev for $J^\pi = 5/2^+$ and $d = -4.4(14)$ keV for $J^\pi = 1/2^+$.

To test the role of 3N forces in these nuclei, the values for the IMME were calculated using both the phenomenological interactions USDA/B supplemented with an isospin non-conserving (INC) Hamiltonian of reference [228] and the NN+3N $\chi$EFT valence space interaction. The results for the USDA/B $d$ and $e$ coefficients are presented in table 4.3. For $A = 20$ in the USDA, the $e$ term comes from mixing of states of similar energy but different isospin in $^{20}$F, $^{20}$Ne, and $^{20}$Na. The largest mixing comes from a pair of close by $T = 0, 2$ states in $^{20}$Ne. The largest mixing for a single level stems from a $J^\pi = 0^+$, $T = 0$ state in $^{20}$Ne that is 641 keV above the $T = 2$ state. The INC mixing matrix element of 49 keV pushes the $T = 2$ state down by 3.8 keV, resulting in a quintic coefficient of $e = -1.7$ keV. With the USDB, these states are nearly degenerate, resulting in an uncertainty that is too large to give a meaningful result. With

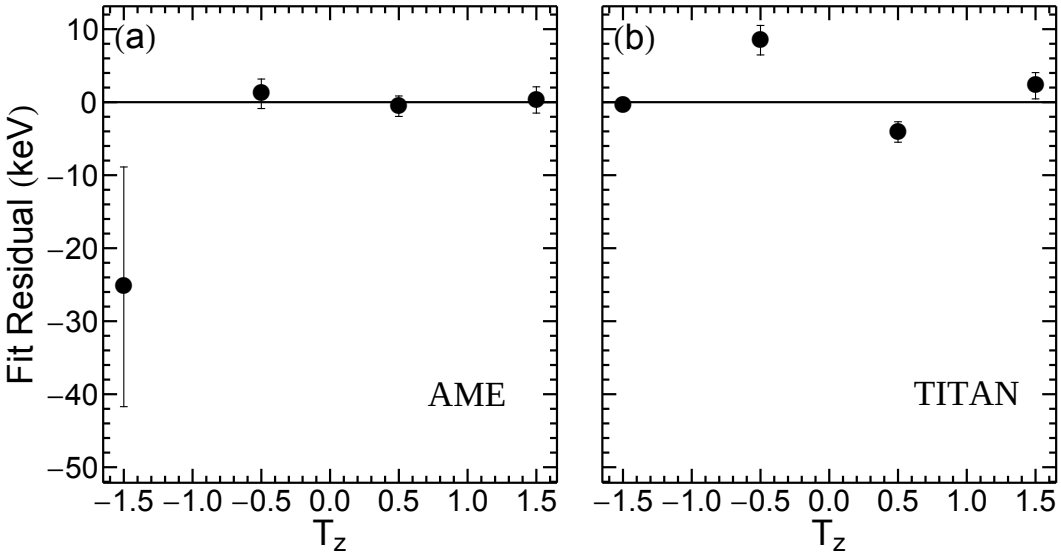


**Figure 4.9:** Ground state $A = 21$ $J^{\pi} = 1/2^{+}$ $T = 3/2$ quadratic residuals for (a) the AME2012 [69] mass values, and (b) using the TITAN mass value for $^{21}$Mg. Excitated state energies are listed in table 4.3

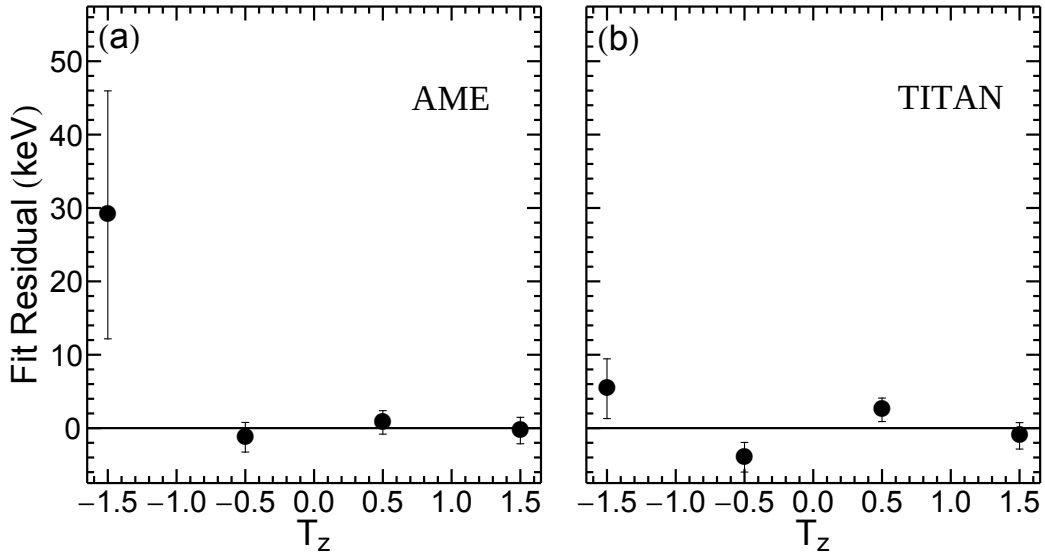


**Figure 4.10:** Excited state $A = 21$, $J^{\pi} = 1/2^{+}$ $T = 3/2$ quadratic residuals for (a) the AME2012 [69] mass values, and (b) using the TITAN mass value for $^{21}$Mg. Excitated state energies are listed in table 4.3.

an INC mixing matrix element of 49 keV, a $T = 0$ level 350 keV above the $T = 2$ state would reproduce the experimental $e$ value. There is a state $657(15)$ keV above the $T = 2$ state with unknown spin that could reproduce the experimental $e$ value if the INC matrix element was $\approx 70$ keV.

The calculated $d$ term for $A = 20$ comes from mixing in $^{20}$F and $^{20}$Na, however, the $T = 2$ states are well separated from nearby $T = 1$ states, resulting in a small shift and a too small $d$ term. The $d$-term for both the USDA and USDB are $-0.1$ keV. Experimentally, there are many $T = 1$ states with unknown spin near the $J^{\pi} = 0^{+}$, $T = 2$ state. If one of these states was an intruder ($p$- to $sd$-shell excitation) $0^{+}$ state there could be enough isospin mixing to give a large $d$ value.

The results for the $A = 21$ $d$-coefficients for the $J = 5/2^{+}$ multiplet are $-0.3$ keV with the USDA and 0.3 keV with the USDB, while for the $J = 1/2^{+}$ multiplet are 1.2 keV with the USDA and 1.9 keV with the USDB. These do not agree with experiment. These non-zero values come from mixing with nearby $T = 1/2$ states in $^{21}$Ne and $^{21}$Na that can be interpreted in terms of a two-level repulsion due to the INC Hamiltonian, as outlined in section 2.5.1.

For the $J = 5/2^{+}$ state the largest two-level shift is due to a $T = 1/2$, $J = 5/2^{+}$ state in $^{21}$Ne, which in the USDA is 372 keV below the $T = 3/2$ isobaric analogue state. The INC mixing matrix element is 25 keV, pushing the $T = 3/2$ level up by 1.6 keV, contributing $+0.8$ keV to the $d$-coefficient. In order for this single state to give $+6.7$ keV for $d$ it would have to lie about 50 keV below the $J = 5/2^{+}$, $T = 3/2$ isobaric analogue state. There are experimental levels that lie 10, 58 and 77 keV below the isobaric analogue state with unknown spins [114], which may contribute to the observed $d$-coefficient. Further experimental investigation is required to determine the spins of these states, which would shed light on the large measured $d$-term.

For the $J = 1/2^{+}$ state the largest two-level shift is due to a $T = 1/2$, $J = 1/2^{+}$ state in $^{21}$Ne that in the USDA is 246 keV above the $T = 3/2$, $J = 1/2^{+}$ isobaric analogue state. The INC mixing matrix element is 27 keV, pushing the $J = 1/2^{+}$, $T = 3/2$ level down by 3.0 keV, and giving a contribution of 1.5 keV to the $d$-coefficient. In order for this single level to give $d = -4.4$ keV it would have to lie about 100 keV below the $J = 1/2^{+}$, $T = 3/2$ IAS. There is an experimental level 71 keV below with an unknown spin [114] that may contribute to the large measured $d$-term. Again, further experimental investigation is required to determine the spins of these states, which would shed light on the large measured $d$-term.

For the $A = 21$ multiplets, it is possible that the experimental results can be explained by INC mixing with nearby $T = 1/2$ states, however, a full understanding from theory, and its relationship to experiment, must be explored in more detail. In the two-level discussion above, we only give the results for the most important state, but there are other states, including those

**Table 4.4:** Experimental and calculated ground-state energies (in MeV) of $^{20,21}$Mg with respect to $^{16}$O.

| Nuclide | Exp. | USDA | USDB | NN + 3N | Exp. - NN + 3N |
|---|---|---|---|---|---|
| $^{20}$Mg | $-6.94$ | $-6.71$ | $-6.83$ | $-6.89$ | $-0.05$ |
| $^{21}$Mg | $-21.59$ | $-21.79$ | $-21.81$ | $-23.18$ | 1.59 |

in $^{21}$Na, that contribute to the total.

The $A = 20, 21$ IMME's were also calculated using $\chi$EFT interactions. These calculations represent the first time that active protons and neutrons in the valence space have been used with $\chi$EFT interactions in the shell model framework [162]. The calculated ground state energies for both $^{20,21}$Mg are listed in table 4.4, along with the results from the USDA/B. The USDA and USDB both reproduce the ground state energies, while the $\chi$EFT calculation only reproduces $^{20}$Mg. However, the ground state of $^{21}$Mg is overbound by 1.6 MeV. Because of these large deviations in the cases where protons and neutrons are active in the valence space, the calculated $d$ and $e$ terms have uncertainties that are too large to make a quantitative judgement on their accuracy. For example, the $A = 20$ $d$ term was calculated to be $-18$ keV, which is vastly different from the experimental value of $2.8(11)$ keV. An interesting feature of these $\chi$EFT calculations is the overbinding decreases as the $T_z$ of the nuclei increases. While $^{21}$Mg is 1.6 MeV overbound, $^{21}$F is only 0.8 MeV overbound. This results in a large cubic term of $d = -38$ keV for the $A = 21$ multiplet. The $\chi$EFT calculations are currently being improved, and recent developments [229] may result in closer agreement with experiment for these multiplets. While these calculations cannot reproduce the experimental values, they do represent an important first step in developing interactions based on $\chi$EFT.

# Chapter 5

# Summary

The abundance of data in experimental nuclear physics is only possible due to the increase in the power and range of exotic beam facilities. The addition of the proposed facilities, such as the Radioisotope Beam Factory (RIBF) in Japan, the Facility for Rare Isotope Beams (FRIB) and the CARIBU facility in the USA, and the Advanced Rare Isotope Laboratory (ARIEL) in Canada will greatly increase the reach of experiments to access the approximately 7000 bound nuclei that are predicted to exist [1]. Many of these nuclei are neutron-rich, and touch on many important aspects of nuclear physics, as their masses are important inputs for astrophysical *r*-process calculations, and in determining the evolution of nuclear structure towards the neutron dripline.

In the past decade, three-nucleon forces have been shown to be crucial in determining the structure of neutron rich nuclei, as three-nucleon forces become increasingly important far from stability. These three-nucleon forces have been derived in the framework of effective field theories based on quantum chromodynamics. $\chi$EFT based interactions offer predictive power to the whole nuclear chart, as only a few coupling constants need to be fit to existing data. Currently, these $\chi$EFT calculations are able to account for the two-nucleon interactions at next-to-next-to-next-to-leading order ($N^3LO$), while the three-nucleon interactions are included at $N^2LO$. Three-nucleon interactions are required, because when bare two-nucleon interactions are used, experiment is not reproduced. This is particularly seen in the magic number $N = 28$ in the calcium isotopic chain, as it is only reproduced with the inclusion of the three-nucleon interaction. This is in contrast to the established calculations performed with phenomenological models, which are fit to a large amount of experimental data in the region applicable to the model. Further, these phenomenological models only include the effect of two-nucleon interactions. While these phenomenological models can reproduce the magic number at $N = 28$, it may be that fitting the matrix elements in these models may mimic the effects of three-nucleon forces.

In this work, the first Penning trap mass measurements of the radioactive nuclei $^{51,52}$Ca, $^{51}$K, and $^{20,21}$Mg were performed at TRIUMF's Ion Trap for Atomic and Nuclear science (TITAN). The measurements of $^{20,21}$Mg required the first use of the Ion Guide Laser Ion Source (IG-LIS), which suppressed the sodium contaminants by up to a factor of $10^6$.

The measured Ca and K nuclides were used to test the predictions of $\chi$EFT based calculations in the vicinity of the predicted neutron magic numbers $N = 32$ and 34. The mass measurements showed a significant flattening of the two-neutron separation energies leading up to $N = 32$, with large deviations from the values tabulated in the 2003 Atomic Mass Evaluation. In fact, the mass of $^{52}$Ca was found to deviate from the tabulated value by 1700(700) keV. The TITAN mass values for $^{51,52}$Ca were confirmed by a later mass measurement by the ISOLTRAP Penning trap mass spectrometer. The masses of $^{53,54}$Ca were measured by ISOLTRAP's multi-reflection time-of-flight mass spectrometer. The combination of the TITAN and ISOLTRAP mass measurements showed excellent agreement with the $\chi$EFT based calculation and the GFPX1A phenomenological interaction. A measurement of the first E($2^+$) in $^{54}$Ca at the RIKEN facility agrees with the prediction of the $\chi$EFT based interaction.

The masses of $^{20,21}$Mg were used to test the predicted quadratic behaviour of the isobaric multiplet mass equation (IMME) using both the phenomenological interactions USDA and USDB, and the $\chi$EFT three-nucleon interaction. This is the first time that $\chi$EFT calculations based in the shell model were used in open shell nuclei, representing an important step in the investigation of $\chi$EFT based calculations. It was found that large cubic terms in the IMME were required to reproduce the experimental data. Neither the USDA/B nor the $\chi$EFT calculations were able to reproduce the experimental cubic terms. The USDA/B calculations typically produced cubic terms near 0 keV, in disagreement with the 3-7 keV values found experimentally. The $\chi$EFT based calculations produced very large cubic terms of between $-20$ to $-40$ keV with quite large errors, preventing any definitive statements as to their origin.

In summary, the influence of three-nucleon forces in $\chi$EFT have:

- Reproduced the $E(2^+)$ in $^{48}$Ca, showing the need for 3N forces,
- Correctly predicted the $E(2^+)$ in $^{54}$Ca, as confirmed by a measurement at RIKEN [118]
- Correctly predicted the behaviour of the $S_{2n}$'s in the calcium isotopes, as confirmed by the measurements presented in this thesis, and by subsequent measurements by ISOLTRAP [59].

Further, we have performed the first mass measurement of $^{51}$K. The $A = 20$ and 21 isobaric multiplet mass equations were aslo tested with TITAN:

- The phenomenological interactions USDA and USDB could not reproduce the large cubic $d$ and quartic $e$ terms observed
- Interactions using 3N forces showed large deviations and errors, indicating that further work is required for cases where both protons and neutrons are active in the calculation.

In each case, theory must further refine their calculations to understand the origin of the large observed $d$ and $e$ terms.

# Bibliography


[1] J. Erler, N. Birge, M. Kortelainen, W. Nazarewicz, E. Olsen, *et al.*. The limits of the nuclear landscape. *Nature*, **486**, 509–512 (2012). doi:10.1038/nature11188. → pages 1, 2, 99

[2] S. Borsanyi, S. Durr, Z. Fodor, C. Hoelbling, S. D. Katz, *et al.*. Ab initio calculation of the neutron-proton mass difference. *Science*, **347**, 1452–1455 (2015). doi:10.1126/science.1257050. → pages 2

[3] A. Frank, J. Jolie, and P. Van Isacker. *Symmetries in atomic nuclei: from isospin to supersymmetry*. Springer tracts in modern physics. Springer, Berlin (2009). → pages 3

[4] N. D. Cook. *Models of the atomic nucleus*. Springer, Heidelberg (2006). → pages 3

[5] B. A. Brown. WSPOT: Woods Saxon code for bound states and decay widths. http://people.nscl.msu.edu/~brown/reaction-codes/home.html (Accessed Dec. 2014). → pages 4

[6] R. Anni and G. Co. Mean-field description of nuclear charge density distributions. *Nuclear Physics*, **588**, 463–478 (1995). doi:10.1016/0375-9474(95)00067-B. → pages 6

[7] R. Woods and D. Saxon. Diffuse Surface Optical Model for Nucleon-Nuclei Scattering. *Phys. Rev.*, **95**, 577–578 (1954). doi:10.1103/PhysRev.95.577. → pages 6

[8] J. D. Holt, T. Otsuka, A. Schwenk, and T. Suzuki. Three-body forces and shell structure in calcium isotopes. *J. Phys. G: Nucl. Part. Phys.*, **39**, 085111 (2012). doi:10.1088/0954-3899/39/8/085111. → pages 6, 30

[9] J. Holt, J. Menéndez, and A. Schwenk. Three-Body Forces and Proton-Rich Nuclei. *Phys. Rev. Lett.*, **110**, 022502 (2013). doi:10.1103/PhysRevLett.110.022502. → pages 6

[10] J. D. Holt, J. Menéndez, and A. Schwenk. Chiral three-nucleon forces and bound excited states in neutron-rich oxygen isotopes. *Eur. Phys. J. A*, **49**, 39 (2013). doi:10.1140/epja/i2013-13039-2. → pages 6, 31, 32

[11] M. G. Mayer. On Closed Shells in Nuclei. II. *Phys. Rev.*, **75**, 1969–1970 (1949). doi:10.1103/PhysRev.75.1969. → pages 6

[12] O. Haxel, J. Jensen, and H. Suess. On the "Magic Numbers" in Nuclear Structure. *Phys. Rev.*, **75**, 1766 (1949). doi:10.1103/PhysRev.75.1766.2. → pages 6

[13] M. G. Mayer. The shell model. *Nobel Lectures: Physics*, **3** (1963). → pages 7

[14] M. Wang, G. Audi, A. H. Wapstra, F. G. Kondev, M. MacCormick, *et al.*. The Ame2012 atomic mass evaluation. *Chinese Phys. C*, **36**, 1603–2014 (2012). doi:10.1088/1674-1137/36/12/003. → pages 7, 8

[15] D. Lunney, J. M. Pearson, and C. Thibault. Recent trends in the determination of nuclear masses. *Rev. Mod. Phys.*, **75**, 1021–1082 (2003). doi:10.1103/RevModPhys.75.1021. → pages 8, 13, 14, 86

[16] W. Satuła, D. J. Dean, J. Gary, S. Mizutori, and W. Nazarewicz. On the origin of the Wigner energy. *Physics Letters B*, **407**, 103–109 (1997). doi:10.1016/S0370-2693(97)00711-9. → pages 8

[17] E. N. M. Quint, J. F. J. van den Brand, J. W. A. den Herder, E. Jans, P. H. M. Keizer, *et al.*. Relative $3s$ spectroscopic strength in $^{206}$Pb and $^{208}$Pb studied with the $(e,e'p)$ knockout reaction. *Phys. Rev. Lett.*, **57**, 186–189 (1986). doi:10.1103/PhysRevLett.57.186. → pages 9

[18] E. Quint, B. M. Barnett, A. M. van den Berg, J. Van den Brand, H. Clement, *et al.*. Evidence for partial occupancy of the $3s_{1/2}$ proton orbit in $^{208}$Pb. *Phys. Rev. Lett.*, **58**, 1088 (1987). doi:10.1103/PhysRevLett.58.1088. → pages 9

[19] K. L. Jones, A. S. Adekola, D. W. Bardayan, J. C. Blackmon, K. Y. Chae, *et al.*. The magic nature of $^{132}$Sn explored through the single-particle states of $^{133}$Sn. *Nature*, **465**, 454–457 (2010). doi:10.1038/nature09048. → pages 9

[20] E. Epelbaum, U.-G. Meißner, and H. W. Hammer. Modern theory of nuclear forces. *Rev. Mod. Phys.*, **81**, 1773–1825 (2009). doi:10.1103/RevModPhys.81.1773. → pages 9, 10

[21] H. Yukawa. On the interaction of elementary particles. I. *Proc. Phys. Math. Soc. Jpn.*, **17**, 48–57 (1935). → pages 9

[22] M. Naghdi. Nucleon-nucleon interaction: A typical/concise review. *Phys. Part. Nuclei*, **45**, 924–971 (2014). doi:10.1134/S1063779614050050. → pages 10, 13

[23] R. B. Wiringa, V. Stoks, and R. Schiavilla. Accurate nucleon-nucleon potential with charge-independence breaking. *Phys. Rev. C*, **51**, 38 (1995). doi:10.1103/PhysRevC.51.38. → pages 10, 11

[24] V. Stoks, R. Klomp, C. Terheggen, and J. J. De Swart. Construction of high-quality *NN* potential models. *Phys. Rev. C*, **49**, 2950 (1994). doi:10.1103/PhysRevC.49.2950. → pages 10

[25] I. E. Lagaris and V. R. Pandharipande. Phenomenological two-nucleon interaction operator. *Nuclear Physics A*, **359**, 331–348 (1981). doi:10.1016/0375-9474(81)90240-2. → pages 10

[26] N. Kalantar-Nayestanaki, E. Epelbaum, J. G. Messchendorp, and A. Nogga. Signatures of three-nucleon interactions in few-nucleon systems. *Rep. Prog. Phys.*, **75**, 016301 (2011). doi:10.1088/0034-4885/75/1/016301. → pages 10, 11

[27] S. C. Pieper. The Illinois Extension to the Fujita-Miyazawa Three-Nucleon Force. In *New Facet of Three Nucleon Force - 50 Years of Fujita Miyazawa Three Nucleon Force (FM50): Proceedings of the International Symposium on New Facet of Three Nucleon Force; Hideyuki Sakai*, pages 143–152. Physics Division, Argonne National Laboratory, Argonne, IL 60439, USA (2008). doi:10.1063/1.2932280. → pages 11

[28] E. Epelbaum, A. Nogga, W. Glöckle, H. Kamada, U.-G. Meißner, *et al.*. Three-nucleon forces from chiral effective field theory. *Phys. Rev. C*, **66**, 064001 (2002). doi:10.1103/PhysRevC.66.064001. → pages 12

[29] S. C. Pieper. Quantum Monte Carlo calculations of light nuclei. *Rivista del Nuovo Cimento*, **31**, 709–740 (2008). doi:10.1393/ncr/i2009-10039-1. → pages 12

[30] N. Ishii, S. Aoki, and T. Hatsuda. Nuclear Force from Lattice QCD. *Phys. Rev. Lett.*, **99**, 022001 (2007). doi:10.1103/PhysRevLett.99.022001. → pages 12, 13

[31] N. Ishii, S. Aoki, and T. Hatsuda. Lattice QCD approach to nuclear force. In *PoS (LATTICE 2007)* (2007). → pages 13

[32] S. Aoki, T. Doi, T. Hatsuda, Y. Ikeda, T. Inoue, *et al.*. Lattice quantum chromodynamical approach to nuclear physics. *Progress of Theoretical and Experimental Physics*, **2012**, 01A105 (2012). doi:10.1093/ptep/pts010. → pages 13

[33] W. Mittig, A. Lépine-Szily, and N. A. Orr. Mass measurement far from stability. *Annual Review of Nuclear and Particle Science*, **47**, 27–66 (1997). doi:10.1146/annurev.nucl.47.1.27. → pages 13, 14

[34] E. G. J. Kessler, M. S. Dewey, R. D. Deslattes, A. Henins, H. G. Börner, *et al.*. The deuteron binding energy and the neutron mass. *Physics Letters A*, **255**, 221–229 (1999). doi:10.1016/S0375-9601(99)00078-X. → pages 13

[35] G. Savard, F. Buchinger, J. A. Clark, J. E. Crawford, S. Gulick, *et al.*. $Q$ Value of the Superallowed Decay of $^{46}$V and Its Influence on $V_{ud}$ and the Unitarity of the Cabibbo-Kobayashi-Maskawa Matrix. *Phys. Rev. Lett.*, **95**, 102501 (2005). doi:10.1103/PhysRevLett.95.102501. → pages 14

[36] T. Eronen, V. Elomaa, U. Hager, J. Hakala, A. Jokinen, *et al.*. $Q$ Values of the Superallowed $\beta$ Emitters $^{26}$Al$^m$, $^{42}$Sc, and $^{46}$V and Their Impact on $V_{ud}$ and the Unitarity of the Cabibbo-Kobayashi-Maskawa Matrix. *Phys. Rev. Lett.*, **97**, 232501 (2006). doi:10.1103/PhysRevLett.97.232501. → pages 14

[37] T. Eronen, D. Gorelov, J. Hakala, J. C. Hardy, A. Jokinen, *et al.*. $Q_{EC}$ values of the superallowed $\beta$ emitters $^{10}$C, $^{34}$Ar, $^{38}$Ca, and $^{46}$V. *Phys. Rev. C*, **83**, 055501 (2011). doi:10.1103/PhysRevC.83.055501. → pages 14

[38] E. Haettner, D. Ackermann, G. Audi, K. Blaum, M. Block, *et al.*. Mass Measurements of Very Neutron-Deficient Mo and Tc Isotopes and Their Impact on rp Process Nucleosynthesis. *Phys. Rev. Lett.*, **106**, 122501 (2011). doi:10.1103/PhysRevLett.106.122501. → pages 14

[39] T. Kuroyanagi, S. Mitarai, B. J. Min, H. Tomura, Y. Haruta, *et al.*. New neutron-deficient isotopes $^{83}$Nb and $^{85}$Nb. *Nuclear Physics A*, **484**, 264–274 (1988). doi:10.1016/0375-9474(88)90072-3. → pages 14

[40] B. Franzke, H. Geissel, and G. Münzenberg. Mass and lifetime measurements of exotic nuclei in storage rings. *Mass Spectrom. Rev.*, **27**, 428–469 (2008). doi:10.1002/mas.20173. → pages 14

[41] K. Blaum. High-accuracy mass spectrometry with stored ions. *Physics Reports*, **425**, 1–78 (2006). doi:10.1016/j.physrep.2005.10.011. → pages 14, 15, 58

[42] E. G. Myers. The most precise atomic mass measurements in Penning traps. *International Journal of Mass Spectrometry*, **349**, 107–122 (2013). doi:10.1016/j.ijms.2013.03.018. → pages 14, 15

[43] H. Savajols. The SPEG Mass Measurement Program at GANIL. *Hyperfine Interact*, **132**, 243–252 (2001). doi:10.1023/A:1011964401634. → pages 14

[44] B. Franzke. The heavy ion storage and cooler ring project ESR at GSI. *Nuclear Inst. and Methods in Physics Research, B*, **24–25, Part 1**, 18–25 (1987). doi:10.1016/0168-583X(87)90583-0. → pages 14

[45] B. Sun, F. Bosch, D. Boutin, C. Brandau, L. Chen, *et al.*. Precise measurement of nuclear isomers in the storage ring at GSI. *Nuclear Physics A*, **834**, 476c–478c (2010). doi:10.1016/j.nuclphysa.2010.01.069. → pages 15

[46] R. N. Wolf, D. Beck, K. Blaum, C. Böhm, C. Borgmann, *et al.*. On-line separation of short-lived nuclei by a multi-reflection time-of-flight device. *Nuclear Inst. and Methods in Physics Research, A*, **686**, 82–90 (2012). doi:10.1016/j.nima.2012.05.067. → pages 15

[47] Y. Ito, P. Schury, M. Wada, S. Naimi, T. Sonoda, *et al.*. Single-reference high-precision mass measurement with a multireflection time-of-flight mass spectrograph. *Phys. Rev. C*, **88**, 011306 (2013). doi:10.1103/PhysRevC.88.011306. → pages 15

[48] W. R. Plaß, T. Dickel, and C. Scheidenberger. Multiple-reflection time-of-flight mass spectrometry. *International Journal of Mass Spectrometry*, **349-350**, 134–144 (2013). doi:10.1016/j.ijms.2013.06.005. → pages 15

[49] G. Gabrielse, A. Khabbaz, D. S. Hall, C. Heimann, H. Kalinowsky, *et al.*. Precision Mass Spectroscopy of the Antiproton and Proton Using Simultaneously Trapped Particles. *Phys. Rev. Lett.*, **82**, 3198 (1999). doi:10.1103/PhysRevLett.82.3198. → pages 15

[50] S. Sturm, F. Köhler, J. Zatorski, A. Wagner, Z. Harman, *et al.*. High-precision measurement of the atomic mass of the electron. *Nature*, **506**, 467–470 (2014). doi:10.1038/nature13026. → pages 15

[51] T. Eronen and J. C. Hardy. High-precision $Q_{\mathrm{EC}}$-value measurements for superallowed decays. *Eur. Phys. J. A*, **48**, 48 (2012). doi:10.1140/epja/i2012-12048-y. → pages 15, 17

[52] J. Dilling, R. Baartman, P. Bricault, M. Brodeur, L. Blomeley, *et al.*. Mass measurements on highly charged radioactive ions, a new approach to high precision with TITAN. *International Journal of Mass Spectrometry*, **251**, 198–203 (2006). doi:10.1016/j.ijms.2006.01.044. → pages 15

[53] I. Tanihata. Neutron halo nuclei. *J. Phys. G: Nucl. Part. Phys.*, **22**, 157 (1996). doi:10.1088/0954-3899/22/2/004. → pages 15

[54] O. Sorlin and M. G. Porquet. Evolution of the $N = 28$ shell closure: a test bench for nuclear forces. *Phys. Scr.*, **T152**, 014003 (2013). doi:10.1088/0031-8949/2013/T152/014003. → pages 15, 20

[55] R. Kanungo, I. Tanihata, and A. Ozawa. Observation of new neutron and proton magic numbers. *Physics Letters B*, **528**, 58–64 (2002). doi:10.1016/S0370-2693(02)01206-6. → pages 15

[56] P. Möller, J. R. Nix, W. D. Myers, and W. J. Swiatecki. Nuclear Ground-State Masses and Deformations. *Atomic Data and Nuclear Data Tables*, **59**, 185 (1995). doi:10.1006/adnd.1995.1002. → pages 15

[57] C. Barbero, J. G. Hirsch, and A. E. Mariano. Deformation and shell effects in nuclear mass formulas. *Nuclear Physics A*, **874**, 81–97 (2012). doi:10.1016/j.nuclphysa.2011.11.005. → pages 15

[58] T. Otsuka, T. Suzuki, J. D. Holt, A. Schwenk, and Y. Akaishi. Three-body forces and the limit of oxygen isotopes. *Phys. Rev. Lett.*, **105**, 032501 (2010). doi:10.1103/PhysRevLett.105.032501. → pages 15, 91

[59] F. Wienholtz, D. Beck, K. Blaum, C. Borgmann, M. Breitenfeldt, *et al.*. Masses of exotic calcium isotopes pin down nuclear forces. *Nature*, **498**, 346–349 (2013). doi:10.1038/nature12226. → pages 15, 35, 83, 86, 88, 90, 100

[60] K. A. Olive. The Review of Particle Physics. *Chin. Phys. C*, **38**, 090001 (2014). doi:10.1088/1674-1137/38/9/090001. → pages 16

[61] R. Fayyazuddin. *Modern Introduction to Particle Physics*. World Scientific Publishing, third edition (2012). → pages 16, 23

[62] L. F. Roberts, S. Reddy, and G. Shen. Medium modification of the charged-current neutrino opacity and its implications. *Phys. Rev. C*, **86**, 065803 (2012). doi:10.1103/PhysRevC.86.065803. → pages 17

[63] O. Korobkin, S. Rosswog, A. Arcones, and C. Winteler. On the astrophysical robustness of the neutron star merger r-process. *Monthly Notices of the Royal Astronomical Society*, **426**, 1940–1949 (2012). doi:10.1111/j.1365-2966.2012.21859.x. → pages 17

[64] A. Aprahamian, I. Bentley, M. Mumpower, and R. Surman. Sensitivity studies for the main r process: nuclear masses. *AIP Advances*, **4**, 041101 (2014). doi:10.1063/1.4867193. → pages 17

[65] A. Arcones and G. Martínez-Pinedo. Nucleosynthesis in neutrino-driven winds: Influence of the nuclear physics input. *J. Phys.: Conf. Ser.*, **202**, 012007 (2010). doi:10.1088/1742-6596/202/1/012007. → pages 18

[66] I. Tanihata, H. Hamagaki, O. Hashimoto, Y. Shida, N. Yoshikawa, *et al.*. Measurements of interaction cross sections and nuclear radii in the light p-shell region. *Phys. Rev. Lett.*, **55**, 2676–2679 (1985). doi:10.1103/PhysRevLett.55.2676. → pages 17

[67] M. Smith, M. Brodeur, T. Brunner, S. Ettenauer, A. Lapierre, *et al.*. First Penning-Trap Mass Measurement of the Exotic Halo Nucleus $^{11}$Li. *Phys. Rev. Lett.*, **101**, 202501 (2008). doi:10.1103/PhysRevLett.101.202501. → pages 18, 44, 74

[68] I. Tanihata, H. Savajols, and R. Kanungo. Recent experimental progress in nuclear halo structure studies. *Progress in Particle and Nuclear Physics*, **68**, 215–313 (2013). doi:10.1016/j.ppnp.2012.07.001. → pages 18

[69] M. Wang, G. Audi, A. H. Wapstra, F. G. Kondev, M. MacCormick, *et al.*. The AME2012 atomic mass evaluation. *Chinese Phys. C*, **36**, 1603 (2012). doi:10.1088/1674-1137/36/12/003. → pages 19, 31, 32, 87, 92, 93, 95, 96

[70] A. Poves, F. Nowacki, and E. Caurier. Isovector effective charge and the staggering of $2^+ \to 0^+$ transition probabilities in the titanium isotopes. *Phys. Rev. C*, **72**, 047302 (2005). doi:10.1103/PhysRevC.72.047302. → pages 19, 34

[71] K. Heyde and J. Wood. Shape coexistence in atomic nuclei. *Rev. Mod. Phys.*, **83**, 1467–1521 (2011). doi:10.1103/RevModPhys.83.1467. → pages 19, 20

[72] B. A. Brown. Towards the future of the nuclear shell model. *Nuclear Physics A*, **704**, 11–20 (2002). doi:10.1016/S0375-9474(02)00761-3. → pages 20

[73] E. K. Warburton, J. A. Becker, and B. A. Brown. Mass systematics for $A = 29 - 44$ nuclei: The deformed $A \approx 32$ region. *Phys. Rev. C*, **41**, 1147–1166 (1990). doi:10.1103/PhysRevC.41.1147. → pages 20

[74] E. Caurier, F. Nowacki, A. Poves, and J. Retamosa. Shell model study of the neutron rich isotopes from oxygen to silicon. *Phys. Rev. C*, **58**, 2033–2040 (1998). doi:10.1103/PhysRevC.58.2033. → pages 20

[75] K. Wimmer, T. Kröll, R. Krücken, V. Bildstein, R. Gernhäuser, *et al.*. Discovery of the Shape Coexisting $0^+$ State in $^{32}$Mg by a Two Neutron Transfer Reaction. *Phys. Rev. Lett.*, **105**, 252501 (2010). doi:10.1103/PhysRevLett.105.252501. → pages 20

[76] R. Kanungo, C. Nociforo, A. Prochazka, Y. Utsuno, T. Aumann, *et al.*. Structure of $^{33}$Mg sheds new light on the $N = 20$ island of inversion. *Physics Letters B*, **685**, 253–257 (2010). doi:10.1016/j.physletb.2010.02.008. → pages 20

[77] B. Bastin, S. Grévy, D. Sohler, O. Sorlin, Z. Dombrádi, *et al.*. Collapse of the $N = 28$ Shell Closure in $^{42}$Si. *Phys. Rev. Lett.*, **99**, 22503 (2007). doi:10.1103/PhysRevLett.99.022503. → pages 20

[78] S. Takeuchi, M. Matsushita, N. Aoi, P. Doornenbal, K. Li, *et al.*. Well Developed Deformation in $^{42}$Si. *Phys. Rev. Lett.*, **109**, 182501 (2012). doi:10.1103/PhysRevLett.109.182501. → pages 20

[79] P. Doornenbal, H. Scheit, S. Takeuchi, N. Aoi, K. Li, *et al.*. In-Beam $\gamma$-Ray Spectroscopy of $^{34,36,38}$Mg: Merging the $N = 20$ and $N = 28$ Shell Quenching. *Phys. Rev. Lett.*, **111**, 212502 (2013). doi:10.1103/PhysRevLett.111.212502. → pages 20

[80] H. L. Crawford, P. Fallon, A. O. Macchiavelli, R. M. Clark, B. A. Brown, *et al.*. Shell and shape evolution at $N = 28$: The $^{40}$Mg ground state. *Phys. Rev. C*, **89**, 041303 (2014). doi:10.1103/PhysRevC.89.041303. → pages 20

[81] T. Otsuka, R. Fujimoto, Y. Utsuno, B. A. Brown, M. Honma, *et al.*. Magic Numbers in Exotic Nuclei and Spin-Isospin Properties of the NN Interaction. *Phys. Rev. Lett.*, **87**, 082502 (2001). doi:10.1103/PhysRevLett.87.082502. → pages 20, 21

[82] A. Ozawa, T. Kobayashi, T. Suzuki, K. Yoshida, and I. Tanihata. New magic number, $N = 16$, near the neutron drip line. *Phys. Rev. Lett.*, **84**, 5493–5495 (2000). → pages 20

[83] R. Kanungo, C. Nociforo, A. Prochazka, T. Aumann, D. Boutin, *et al.*. One-Neutron Removal Measurement Reveals $^{24}$O as a New Doubly Magic Nucleus. *Phys. Rev. Lett.*, **102**, 152501 (2009). doi:10.1103/PhysRevLett.102.152501. → pages 20

[84] C. R. Hoffman, T. Baumann, D. Bazin, J. Brown, G. Christian, *et al.*. Evidence for a doubly magic $^{24}$O. *Physics Letters B*, **672**, 17–21 (2009). doi:10.1016/j.physletb.2008.12.066. → pages 20

[85] G. Audi, A. H. Wapstra, and C. Thibault. The Ame2003 atomic mass evaluation. *Nuclear Physics A*, **729**, 337–676 (2003). doi:10.1016/j.nuclphysa.2003.11.003. → pages 21, 85, 86, 92

[86] E. Epelbaum. Nuclear forces from chiral effective field theory: a primer. *arXiv* (2010). → pages 23

[87] S. K. Bogner, R. J. Furnstahl, and A. Schwenk. From low-momentum interactions to nuclear structure. *Progress in Particle and Nuclear Physics*, **65**, 94–147 (2010). doi:10.1016/j.ppnp.2010.03.001. → pages 24, 25

[88] S. Bogner, R. Furnstahl, and R. Perry. Similarity renormalization group for nucleon-nucleon interactions. *Phys. Rev. C*, **75**, 061001 (2007). doi:10.1103/PhysRevC.75.061001. → pages 25, 26

[89] K. Tsukiyama, S. K. Bogner, and A. Schwenk. In-Medium Similarity Renormalization Group For Nuclei. *Phys. Rev. Lett.*, **106**, 222502 (2011). doi:10.1103/PhysRevLett.106.222502. → pages 26

[90] H. Hergert, S. Bogner, S. Binder, A. Calci, J. Langhammer, *et al.*. In-medium similarity renormalization group with chiral two- plus three-nucleon interactions. *Phys. Rev. C*, **87**, 034307 (2013). doi:10.1103/PhysRevC.87.034307. → pages 26

[91] H. Hergert, S. K. Bogner, T. D. Morris, S. Binder, A. Calci, *et al.*. *Ab initio* multireference in-medium similarity renormalization group calculations of even calcium and nickel isotopes. *Phys. Rev. C*, **90**, 041302 (2014). doi:10.1103/PhysRevC.90.041302. → pages 26

[92] T. T. S. Kuo and E. Osnes. Folded-Diagram Theory of the Effective Interaction in Nuclei, Atoms and Molecules. *Lect. Notes Phys*, **364** (1990). doi:10.1007/3-540-53023-1. → pages 26, 28

[93] B. A. Brown and W. A. Richter. New "USD" Hamiltonians for the sd shell. *Phys. Rev. C*, **74**, 034315 (2006). doi:10.1103/PhysRevC.74.034315. → pages 28, 29, 31

[94] A. Poves, J. Sánchez-Solano, E. Caurier, and F. Nowacki. Shell model study of the isobaric chains $A = 50$, $A = 51$ and $A = 52$. *Nuclear Physics*, **694**, 157–198 (2001). doi:10.1016/S0375-9474(01)00967-8. → pages 28, 29

[95] M. Honma, T. Otsuka, B. A. Brown, and T. Mizusaki. Shell-model description of neutron-rich pf-shell nuclei with a new effective interaction GXPF1. *Eur. Phys. J. A*, **25**, 499–502 (2005). doi:10.1140/epjad/i2005-06-032-2. → pages 28, 29

[96] M. Hjorth-Jensen, T. T. S. Kuo, and E. Osnes. Realistic effective interactions for nuclear systems. *Physics Reports*, **261**, 125–270 (1995). doi:10.1016/0370-1573(95)00012-6. → pages 28

[97] L. Coraggio, A. Covello, A. Gargano, and N. Itaco. From Kuo–Brown to today's realistic shell-model calculations. *Nuclear Physics A*, **928**, 43–50 (2014). doi:10.1016/j.nuclphysa.2014.03.018. → pages 28

[98] B. H. Wildenthal. Empirical strengths of spin operators in nuclei. *Progress in Particle and Nuclear Physics*, **11**, 5–51 (1984). doi:10.1016/0146-6410(84)90011-5. → pages 28, 29

[99] E. Caurier, G. Martínez-Pinedo, F. Nowacki, A. Poves, and A. P. Zuker. The shell model as a unified view of nuclear structure. *Rev. Mod. Phys.*, **77**, 427–488 (2005). doi:10.1103/RevModPhys.77.427. → pages 28, 34

[100] E. Caurier and F. Nowacki. Present Status of Shell Model Techniques. *Acta Phys. Pol. B*, **30**, 705 (1999). → pages 28, 34

[101] B. A. Brown and *et al.* OXBASH for Windows MSU-NSCL report number 1289, National Superconducting Cyclotron Laboratory, Michigan State University, East Lansing, Michigan (2004). → pages 28

[102] C. Lanczos. An Iteration Method for the Solution of the Eigenvalue Problem of Linear Differential and Integral Operators. *Journal of Research of the National Bureau of Standards*, **45**, 255–282 (1950). doi:10.6028/jres.045.026. → pages 29

[103] T. Otsuka, T. Suzuki, R. Fujimoto, H. Grawe, and Y. Akaishi. Evolution of Nuclear Shells due to the Tensor Force. *Phys. Rev. Lett.*, **95**, 232502 (2005). doi:10.1103/PhysRevLett.95.232502. → pages 29

[104] A. P. Zuker. Three-Body Monopole Corrections to Realistic Interactions. *Phys. Rev. Lett.*, **90**, 042502 (2003). doi:10.1103/PhysRevLett.90.042502. → pages 29

[105] T. T. S. Kuo and G. E. Brown. Reaction matrix elements for the 0f-1p shell nuclei. *Nuclear Physics A*, **114**, 241–279 (1968). doi:10.1016/0375-9474(68)90353-9. → pages 29

[106] A. Poves and A. Zuker. Theoretical spectroscopy and the fp shell. *Physics Reports*, **70**, 235–314 (1981). doi:10.1016/0370-1573(81)90153-8. → pages 29

[107] M. Honma, T. Otsuka, B. A. Brown, and T. Mizusaki. Effective interaction for pf-shell nuclei. *Phys. Rev. C*, **65**, 061301 (2002). doi:10.1103/PhysRevC.65.061301. → pages 29

[108] R. Roth, S. Binder, K. Vobig, A. Calci, J. Langhammer, *et al.*. Medium-Mass Nuclei with Normal-Ordered Chiral $NN + 3N$ Interactions. *Phys. Rev. Lett.*, **109**, 052501 (2012). doi:10.1103/PhysRevLett.109.052501. → pages 30

[109] G. Hagen, M. Hjorth-Jensen, G. R. Jansen, R. Machleidt, and T. Papenbrock. Continuum Effects and Three-Nucleon Forces in Neutron-Rich Oxygen Isotopes. *Phys.*

*Rev. Lett.*, **108**, 242501 (2012). doi:10.1103/PhysRevLett.108.242501. → pages 30, 31, 32

[110] G. Hagen, T. Papenbrock, D. J. Dean, A. Schwenk, A. Nogga, *et al.*. Coupled-cluster theory for three-body Hamiltonians. *Phys. Rev. C*, **76**, 034302 (2007). doi:10.1103/PhysRevC.76.034302. → pages 30

[111] J. D. Holt, J. Menéndez, J. Simonis, and A. Schwenk. Three-nucleon forces and spectroscopy of neutron-rich calcium isotopes. *Phys. Rev. C*, **90**, 024312 (2014). doi:10.1103/PhysRevC.90.024312. → pages 30, 31

[112] T. R. Rodríguez and J. L. Egido. New Beyond-Mean-Field Theories: Examination of the Potential Shell Closures at $N = 32$ or 34. *Phys. Rev. Lett.*, **99**, 062501 (2007). doi:10.1103/PhysRevLett.99.062501. → pages 33, 35

[113] A. Bürger, T. R. Saito, H. Grawe, H. Hübel, P. Reiter, *et al.*. Relativistic Coulomb excitation of neutron-rich 54,56,58Cr: On the pathway of magicity from to. *Physics Letters B*, **622**, 29–34 (2005). doi:10.1016/j.physletb.2005.07.004. → pages 33

[114] Evaluated Nuclear Structure Data File. http://www.nndc.bnl.gov/ensdf/. → pages 33, 35, 87, 93, 97

[115] D. C. Dinca, R. Janssens, A. Gade, D. Bazin, R. Broda, *et al.*. Reduced transition probabilities to the first 2+ state in Ti52,54,56 and development of shell closures at N=32,34. *Phys. Rev. C*, **71** (2005). doi:10.1103/PhysRevC.71.041302. → pages 33

[116] H. Grawe. Shell Model from a Practitioner's Point of View. *Lect. Notes Phys*, **651**, 33–75 (2004). doi:10.1007/978-3-540-44490-9_2. → pages 33

[117] E. Caurier. Shell model code ANTOINE (IRES, STRASBOURG 1989-2002). → pages 34

[118] D. Steppenbeck, S. Takeuchi, N. Aoi, P. Doornenbal, M. Matsushita, *et al.*. Evidence for a new nuclear 'magic number' from the level structure of $^{54}$Ca. *Nature*, **502**, 207–210 (2013). doi:10.1038/nature12522. → pages 34, 35, 88, 100

[119] J. D. Holt, J. Menéndez, and A. Schwenk. The role of three-nucleon forces and many-body processes in nuclear pairing. *J. Phys. G: Nucl. Part. Phys.*, **40**, 075105 (2013). doi:10.1088/0954-3899/40/7/075105. → pages 34, 35, 36, 91

[120] G. Hagen, M. Hjorth-Jensen, G. R. Jansen, R. Machleidt, and T. Papenbrock. Evolution of Shell Structure in Neutron-Rich Calcium Isotopes. *Phys. Rev. Lett.*, **109**, 032502 (2012). doi:10.1103/PhysRevLett.109.032502. → pages 34, 35, 36, 91

[121] G. Audi and M. Wang. Private Communication (2011). → pages 35, 36

[122] W. Heisenberg. Über den Bau der Atomkerne. I. *Zeitschrift für Physik*, **77**, 1–11 (1932). doi:10.1007/BF01342433. → pages 36

[123] D. R. Tilley, J. H. Kelley, J. L. Godwin, D. J. Millener, J. E. Purcell, *et al.*. Energy levels of light nuclei $A = 8, 9, 10$. *Nuclear Physics A*, **745**, 155–362 (2004). doi:10.1016/j.nuclphysa.2004.09.059. → pages 37

[124] S. Lenzi, N. Marginean, D. Napoli, C. Ur, A. Zuker, *et al.*. Coulomb Energy Differences in $T = 1$ Mirror Rotational Bands in $^{50}$Fe and $^{50}$Cr. *Phys. Rev. Lett.*, **87**, 122501 (2001). doi:10.1103/PhysRevLett.87.122501. → pages 36, 38

[125] P. J. Davies, M. A. Bentley, T. W. Henry, E. C. Simpson, A. Gade, *et al.*. Mirror Energy Differences at Large Isospin Studied through Direct Two-Nucleon Knockout. *Phys. Rev. Lett.*, **111**, 072501 (2013). doi:10.1103/PhysRevLett.111.072501. → pages 36

[126] J. Ekman, D. Rudolph, C. Fahlander, A. Zuker, M. Bentley, *et al.*. Unusual Isospin-Breaking and Isospin-Mixing Effects in the $A = 35$ Mirror Nuclei. *Phys. Rev. Lett.*, **92**, 132502 (2004). doi:10.1103/PhysRevLett.92.132502. → pages 36

[127] J. J. Sakurai. *Modern Quantum Mechanics (Revised Edition)*. Addison Wesley, first edition (1993). → pages 38

[128] S. Weinberg and S. Treiman. Electromagnetic Corrections to Isotopic Spin Conservation. *Phys. Rev.*, **116**, 465–468 (1959). doi:10.1103/PhysRev.116.465. → pages 39

[129] Y. H. Lam, B. Blank, N. A. Smirnova, J. B. Bueb, and M. S. Antony. The isobaric multiplet mass equation for $A \leq 71$ revisited. *Atomic Data and Nuclear Data Tables*, **99**, 680–703 (2013). doi:10.1016/j.adt.2012.11.002. → pages 40, 41, 93, 94

[130] M. Brodeur, T. Brunner, S. Ettenauer, A. Lapierre, R. Ringle, *et al.*. Elucidation of the Anomalous $A = 9$ Isospin Quartet Behavior. *Phys. Rev. Lett.*, **108**, 212501 (2012). doi:10.1103/PhysRevLett.108.212501. → pages 41, 43

[131] C. Yazidjian, G. Audi, D. Beck, K. Blaum, S. George, *et al.*. Evidence for a breakdown of the isobaric multiplet mass equation: A study of the $A = 35$, $T = 3/2$ isospin quartet. *Phys. Rev. C*, **76**, 024308 (2007). doi:10.1103/PhysRevC.76.024308. → pages 41

[132] R. J. Charity, J. M. Elson, J. Manfredi, R. Shane, L. G. Sobotka, *et al.*. Isobaric multiplet mass equation for $A = 7$ and 8. *Phys. Rev. C*, **84**, 051308 (2011). doi:10.1103/PhysRevC.84.051308. → pages 41

[133] A. A. Kwiatkowski, B. R. Barquest, G. Bollen, C. M. Campbell, D. L. Lincoln, *et al.*. Precision test of the isobaric multiplet mass equation for the $A = 32$, $T = 2$ quintet. *Phys. Rev. C*, **80**, 051302 (2009). doi:10.1103/PhysRevC.80.051302. → pages 41

[134] A. Kankainen, T. Eronen, D. Gorelov, J. Hakala, A. Jokinen, *et al.*. High-precision mass measurement of $^{31}$S with the double Penning trap JYFLTRAP improves the mass value for $^{32}$Cl. *Phys. Rev. C*, **82**, 052501 (2010). doi:10.1103/PhysRevC.82.052501. → pages 41

[135] R. F. Casten. *Nuclear Physics from a Simple Perspective*. Oxford University Press (1990). → pages 42

[136] Y. H. Lam, N. A. Smirnova, and E. Caurier. Isospin nonconservation in sd-shell nuclei. *Phys. Rev. C*, **87**, 054304 (2013). doi:10.1103/PhysRevC.87.054304. → pages 43

[137] M. Dombsky, D. Bishop, P. Bricault, D. Dale, A. Hurst, *et al.*. Commissioning and initial operation of a radioactive beam ion source at ISAC. *Rev. Sci. Instrum.*, **71**, 978 (2000). doi:10.1063/1.1150364. → pages 44

[138] M. Brodeur, T. Brunner, C. Champagne, S. Ettenauer, M. J. Smith, *et al.*. First Direct Mass Measurement of the Two-Neutron Halo Nucleus $^{6}$He and Improved Mass for the Four-Neutron Halo $^{8}$He. *Phys. Rev. Lett.*, **108**, 052504 (2012). doi:10.1103/PhysRevLett.108.052504. → pages 44

[139] R. Ringle, M. Brodeur, T. Brunner, S. Ettenauer, M. Smith, *et al.*. High-precision Penning trap mass measurements of $^{9,10}$Be and the one-neutron halo nuclide $^{11}$Be. *Physics Letters B*, **675**, 170–174 (2009). doi:10.1016/j.physletb.2009.04.014. → pages 44

[140] S. Ettenauer, M. Brodeur, T. Brunner, A. T. Gallant, A. Lapierre, *et al.*. Precision ground state mass of $^{12}$Be and an isobaric multiplet mass equation (IMME) extrapolation for $2^+$ and $0_2^+$ states in the $T = 2$, $A = 12$ multiplet. *Phys. Rev. C*, **81**, 024314 (2010). doi:10.1103/PhysRevC.81.024314. → pages 44

[141] R. Kanungo, A. T. Gallant, M. Uchida, C. Andreoiu, R. A. E. Austin, *et al.*. Structure of states in $^{12}$Be via the $^{11}$Be$(d,p)$ reaction. *Physics Letters B*, **682**, 391–395 (2010). doi:10.1016/j.physletb.2009.11.025. → pages 44

[142] A. Chaudhuri, C. Andreoiu, T. Brunner, U. Chowdhury, S. Ettenauer, *et al.*. Evidence for the extinction of the $N = 20$ neutron-shell closure for $^{32}$Mg from direct mass measurements. *Phys. Rev. C*, **88**, 054317 (2013). doi:10.1103/PhysRevC.88.054317. → pages 44

[143] A. A. Kwiatkowski, C. Andreoiu, J. C. Bale, A. Chaudhuri, U. Chowdhury, *et al.*. Anastrophe in the island-of-inversion $S_{2n}$ from precision mass cartography. *Physics Letters B* (submitted). → pages 44

[144] V. Simon, T. Brunner, U. Chowdhury, B. Eberhardt, S. Ettenauer, *et al.*. Penning-trap mass spectrometry of highly charged, neutron-rich Rb and Sr isotopes in the vicinity of $A \approx 100$. *Phys. Rev. C*, **85**, 064308 (2012). doi:10.1103/PhysRevC.85.064308. → pages 44, 57, 124

[145] R. Klawitter (in preparation). → pages 44, 57

[146] D. Frekers, M. C. Simon, C. Andreoiu, J. C. Bale, M. Brodeur, *et al.*. Penning-trap $Q$-value determination of the $^{71}$Ga$(\nu, e^-)^{71}$Ge reaction using threshold charge breeding

of on-line produced isotopes. *Physics Letters B*, **722**, 233–237 (2013). doi:10.1016/j.physletb.2013.04.019. → pages 44, 56

[147] S. Ettenauer, M. Simon, A. Gallant, T. Brunner, U. Chowdhury, *et al.*. First Use of High Charge States for Mass Measurements of Short-Lived Nuclides in a Penning Trap. *Phys. Rev. Lett.*, **107**, 272501 (2011). doi:10.1103/PhysRevLett.107.272501. → pages 44, 45, 56, 124

[148] G. Bollen. Mass measurements of short-lived nuclides with ion traps. *Nuclear Physics A*, **693**, 3–18 (2001). doi:10.1016/j.physletb.2013.04.019. → pages 45, 57

[149] G. Bollen, S. Becker, H. J. Kluge, M. König, R. B. Moore, *et al.*. ISOLTRAP: a tandem Penning trap system for accurate on-line mass determination of short-lived isotopes. *Nuclear Inst. and Methods in Physics Research, A*, **368**, 675–697 (1996). doi:10.1016/j.physletb.2013.04.019. → pages 45, 73

[150] A. Kellerbauer, G. Audi, D. Beck, K. Blaum, G. Bollen, *et al.*. High-precision masses of neutron-deficient rubidium isotopes using a Penning trap mass spectrometer. *Phys. Rev. C*, **76**, 045504 (2007). doi:10.1103/PhysRevC.76.045504. → pages 46

[151] D. J. Morrissey and B. M. Sherrill. In-flight separation of projectile fragments. *Lect. Notes Phys*, **651**, 113–135 (2004). doi:10.1007/b98790. → pages 46

[152] Y. Blumenfeld, T. Nilsson, and P. Van Duppen. Facilities and methods for radioactive ion beam production. *Phys. Scr.*, **T152**, 014023 (2013). doi:10.1088/0031-8949/2013/T152/014023. → pages 46

[153] G. Savard, R. C. Pardo, S. Baker, C. N. Davids, A. Levand, *et al.*. CARIBU: a new facility for the study of neutron-rich isotopes. *Hyperfine Interact*, **199**, 301–309 (2011). doi:10.1007/s10751-011-0325-5. → pages 46

[154] J. Ärje, J. Äystö, H. Hyvönen, P. Taskinen, V. Koponen, *et al.*. The ion guide isotope separator on-line, IGISOL. *Nuclear Inst. and Methods in Physics Research, A*, **247**, 431–437 (1986). doi:10.1016/0168-9002(86)90404-3. → pages 46

[155] M. Brodeur. *First direct mass measurement of the two and four neutron halos $^{6}$He and $^{8}$He using the TITAN Penning trap mass spectrometer*. Ph.D. thesis, University of British Columbia (2010). → pages 47, 51, 73, 75, 79, 124

[156] F. Ames, P. Bricault, H. Heggen, P. Kunz, J. Lassen, *et al.*. Ion source developments for the production of radioactive isotope beams at TRIUMF. *Rev. Sci. Instrum.*, **85**, 02B912 (2014). doi:10.1063/1.4833926. → pages 47, 49

[157] R. Kirchner and E. Roeckl. Investigation of gaseous discharge ion sources for isotope separation on-line. *Nuclear Instruments and Methods*, **133**, 187–204 (1976). doi:10.1016/0029-554X(76)90607-8. → pages 47

[158] J. Lassen, P. Bricault, M. Dombsky, J. P. Lavoie, M. Gillner, *et al.*. Laser Ion Source Operation at the TRIUMF Radioactive Ion Beam Facility. In *4TH International Conference on Laser Probing-LAP 2008. AIP Conference Proceedings*, pages 9–15 (2009). doi:10.1063/1.3115616. → pages 48, 49

[159] S. Raeder, H. Heggen, J. Lassen, F. Ames, D. Bishop, *et al.*. An ion guide laser ion source for isobar-suppressed rare isotope beams. *Rev. Sci. Instrum.*, **85**, 033309 (2014). doi:10.1063/1.4868496. → pages 49, 50

[160] V. N. Fedosseev, L. E. Berg, D. V. Fedorov, D. Fink, O. J. Launila, *et al.*. Upgrade of the resonance ionization laser ion source at ISOLDE on-line isotope separation facility: New lasers and new ion beams. *Rev. Sci. Instrum.*, **83**, 02A903 (2012). doi:10.1063/1.3662206. → pages 49

[161] J. Äystö. Development and applications of the IGISOL technique. *Nuclear Physics A*, **693**, 477 (2001). doi:10.1016/S0375-9474(01)00923-X. → pages 49

[162] A. T. Gallant, M. Brodeur, C. Andreoiu, A. Bader, A. Chaudhuri, *et al.*. Breakdown of the Isobaric Multiplet Mass Equation for the $A = 20$ and 21 Multiplets. *Phys. Rev. Lett.*, **113**, 082501 (2014). doi:10.1103/PhysRevLett.113.082501. → pages 49, 98

[163] K. Blaum, C. Geppert, H. J. Kluge, M. Mukherjee, S. Schwarz, *et al.*. A novel scheme for a highly selective laser ion source. *Nuclear Instruments and Methods in Physics Research Section B: Beam Interactions with Materials and Atoms*, **204**, 331–335 (2003). doi:10.1016/S0168-583X(02)01942-0. → pages 49

[164] D. A. Fink, S. D. Richter, B. Bastin, K. Blaum, R. Catherall, *et al.*. First application of the Laser Ion Source and Trap (LIST) for on-line experiments at ISOLDE. *Nuclear Instruments and Methods in Physics Research Section B: Beam Interactions with Materials and Atoms*, **317**, 417–421 (2013). doi:10.1016/j.nimb.2013.06.039. → pages 49

[165] T. Brunner, M. J. Smith, M. Brodeur, S. Ettenauer, A. T. Gallant, *et al.*. TITAN's digital RFQ ion beam cooler and buncher, operation and performance. *Nuclear Inst. and Methods in Physics Research, A*, **676**, 32–43 (2012). doi:10.1016/j.nima.2012.02.004. → pages 51, 52

[166] F. G. Major and H. G. Dehmelt. Exchange-Collision Technique for the rf Spectroscopy of Stored Ions. *Phys. Rev.*, **170**, 91–107 (1968). doi:10.1103/PhysRev.170.91. → pages 52

[167] F. Herfurth and K. Blaum, editors. *Trapped Charged Particles and Fundamental Interactions*, volume 749 of *Lecture Notes in Physics* (2008). doi:10.1007/978-3-540-77817-2. → pages 52

[168] J. D. Prestage, G. J. Dick, and L. Maleki. New ion trap for frequency standard applications. *J. Appl. Phys.*, **66**, 1013–1017 (1989). doi:10.1063/1.343486. → pages 53

[169] M. G. Raizen, J. M. Gilligan, J. C. Bergquist, W. M. Itano, and D. J. Wineland. Ionic crystals in a linear Paul trap. *Phys. Rev. A*, **45**, 6493–6501 (1992). doi:10.1103/PhysRevA.45.6493. → pages 53

[170] M. Drewsen and A. Brøner. Harmonic linear Paul trap: Stability diagram and effective potentials. *Phys. Rev. A*, **62**, 045401 (2000). doi:10.1103/PhysRevA.62.045401. → pages 53

[171] N. Konenkov, M. Sudakov, and D. Douglas. Matrix methods for the calculation of stability diagrams in quadrupole mass spectrometry. *J Am Soc Mass Spectrom*, **13**, 597–613 (2002). doi:10.1016/S1044-0305(02)00365-3. → pages 55

[172] A. Lapierre, M. Brodeur, T. Brunner, S. Ettenauer, A. T. Gallant, *et al.*. The TITAN EBIT charge breeder for mass measurements on highly charged short-lived isotopes—First online operation. *Nuclear Instruments and Methods in Physics Research Section A: Accelerators, Spectrometers, Detectors and Associated Equipment*, **624**, 54–64 (2010). doi:10.1016/j.nima.2010.09.030. → pages 56

[173] T. D. Macdonald, B. E. Schultz, J. C. Bale, A. Chaudhuri, U. Chowdhury, *et al.*. Precision Penning-trap measurement to investigate the role of the $^{51}\mathrm{Cr}(e^-, \nu_e)^{51}\mathrm{V}$ $Q$ value in the gallium anomaly. *Phys. Rev. C*, **89**, 044318 (2014). doi:10.1103/PhysRevC.89.044318. → pages 56, 123

[174] A. Gallant, M. Brodeur, T. Brunner, U. Chowdhury, S. Ettenauer, *et al.*. Highly charged ions in Penning traps: A new tool for resolving low-lying isomeric states. *Phys. Rev. C*, **85**, 044311 (2012). doi:10.1103/PhysRevC.85.044311. → pages 57, 124, 126

[175] V. V. Simon, P. Delheij, J. Dilling, Z. Ke, W. Shi, *et al.*. Cooling of short-lived, radioactive, highly charged ions with the TITAN cooler Penning trap. *Hyperfine Interact*, **199**, 151–159 (2011). doi:10.1007/s10751-011-0309-5. → pages 57

[176] Z. Ke, W. Shi, G. Gwinner, K. Sharma, S. Toews, *et al.*. A cooler ion trap for the TITAN on-line trapping facility at TRIUMF. *Hyperfine Interact*, **173**, 103–111 (2007). doi:10.1007/s10751-007-9548-x. → pages 58

[177] L. Brown and G. Gabrielse. Geonium theory: Physics of a single electron or ion in a Penning trap. *Rev. Mod. Phys.*, **58**, 233 (1986). doi:10.1103/RevModPhys.58.233. → pages 59, 60

[178] A. G. Marshall, C. L. Hendrickson, and G. S. Jackson. Fourier transform ion cyclotron resonance mass spectrometry: A primer. *Mass Spectrom. Rev.*, **17**, 1–35 (1998). doi:10.1002/(SICI)1098-2787(1998)17:1⟨1::AID-MAS1⟩3.0.CO;2-K. → pages 61

[179] S. Eliseev, K. Blaum, M. Block, A. Dörr, C. Droese, *et al.*. A phase-imaging technique for cyclotron-frequency measurements. *Appl. Phys. B*, **114**, 107–128 (2014). doi:10.1007/s00340-013-5621-0. → pages 61, 122

[180] D. A. Nesterenko, S. Eliseev, K. Blaum, M. Block, S. Chenmarev, *et al.*. Direct determination of the atomic mass difference of $^{187}$Re and $^{187}$Os for neutrino physics and cosmochronology. *Phys. Rev. C*, **90**, 042501 (2014). doi:10.1103/PhysRevC.90.042501. → pages 61

[181] M. Kretzschmar. Theoretical investigations of different excitation modes for Penning trap mass spectrometry. *International Journal of Mass Spectrometry*, **349-350**, 227–239 (2013). doi:10.1016/j.ijms.2013.03.023. → pages 61, 69

[182] M. König, G. Bollen, H. J. Kluge, T. Otto, and J. Szerypo. Quadrupole excitation of stored ion motion at the true cyclotron frequency. *International journal of mass spectrometry and ion processes*, **142**, 95–116 (1995). doi:10.1016/0168-1176(95)04146-C. → pages 62, 66, 70, 71, 89, 93

[183] M. Kretzschmar. The Ramsey method in high-precision mass spectrometry with Penning traps: Theoretical foundations. *International Journal of Mass Spectrometry*, **264**, 122–145 (2007). doi:10.1016/j.ijms.2007.04.002. → pages 62, 63, 66, 68

[184] M. Kretzschmar. Single particle motion in a Penning trap: description in the classical canonical formalism. *Phys. Scr.*, **46**, 544–554 (1992). doi:10.1088/0031-8949/46/6/011. → pages 62

[185] L. D. Landau and E. M. Lifshitz. *Quantum Mechanics: Non-relativistic theory*, volume 3 of *Course of Theoretical Physics*. Pergamon Press, Oxford; New York, third edition (1991, c1977). → pages 64

[186] L. I. Schiff. *Quantum mechanics*. McGraw-Hill New York, third edition (1949). → pages 64

[187] N. F. Ramsey. Experiments with separated oscillatory fields and hydrogen masers. *Rev. Mod. Phys.*, **62**, 541–552 (1990). doi:10.1103/RevModPhys.62.541. → pages 68

[188] S. George, K. Blaum, F. Herfurth, A. Herlert, M. Kretzschmar, *et al.*. The Ramsey method in high-precision mass spectrometry with Penning traps: Experimental results. *International Journal of Mass Spectrometry*, **264**, 110–121 (2007). doi:10.1016/j.ijms.2007.04.003. → pages 68

[189] M. Eibach, T. Beyer, K. Blaum, M. Block, K. Eberhardt, *et al.*. First investigation of phase-shifted Ramsey excitation in Penning trap mass spectrometry. *International Journal of Mass Spectrometry*, **303**, 27–30 (2011). doi:10.1016/j.ijms.2010.12.006. → pages 68

[190] R. S. Van Dyck Jr, F. L. Moore, D. L. Farnham, and P. B. Schwinberg. Number dependency in the compensated Penning trap. *Phys. Rev. A*, **40**, 6308 (1989). doi:10.1103/PhysRevA.40.6308. → pages 69, 80

[191] G. Bollen, H. J. Kluge, M. König, T. Otto, G. Savard, *et al.*. Resolution of nuclear ground and isomeric states by a Penning trap mass spectrometer. *Phys. Rev. C*, **46**, R2140 (1992). doi:10.1103/PhysRevC.46.R2140. → pages 69, 80

[192] M. Kretzschmar. Calculating damping effects for the ion motion in a Penning trap. *The European Physical Journal D - Atomic, Molecular and Optical Physics*, **48**, 313–319 (2008). doi:10.1140/epjd/e2008-00125-0. → pages 69

[193] M. Block, D. Ackermann, D. Beck, K. Blaum, M. Breitenfeldt, *et al.*. The ion-trap facility SHIPTRAP. *Eur. Phys. J. A*, **25**, 49–50 (2005). doi:10.1140/epjad/i2005-06-013-5. → pages 73

[194] R. Ringle, G. Bollen, A. Prinke, J. Savory, P. Schury, *et al.*. The LEBIT 9.4T Penning trap mass spectrometer. *Nuclear Instruments and Methods in Physics Research Section A: Accelerators, Spectrometers, Detectors and Associated Equipment*, **604**, 536–547 (2009). doi:10.1016/j.nima.2009.03.207. → pages 73

[195] R. Ringle, G. Bollen, A. Prinke, J. Savory, P. Schury, *et al.*. A "Lorentz" steerer for ion injection into a Penning trap. *International Journal of Mass Spectrometry*, **263**, 38–44 (2007). doi:10.1016/j.ijms.2006.12.008. → pages 73, 74

[196] K. Blaum, G. Bollen, F. Herfurth, A. G. Kellerbauer, H. J. Kluge, *et al.*. Recent developments at ISOLTRAP: towards a relative mass accuracy of exotic nuclei below $10^{-8}$. *J. Phys. B*, **36**, 921–930 (2003). doi:10.1088/0953-4075/36/5/311. → pages 73

[197] S. Ettenauer. *First mass measurements of highly charged, short-lived nuclides in a Penning trap and the mass of Rb-74*. Ph.D. thesis, University of British Columbia (2012). → pages 76, 124

[198] M. Brodeur, V. L. Ryjkov, T. Brunner, S. Ettenauer, A. T. Gallant, *et al.*. Verifying the accuracy of the TITAN Penning-trap mass spectrometer. *International Journal of Mass Spectrometry*, **310**, 20–31 (2012). doi:10.1016/j.ijms.2011.11.002. → pages 75, 79, 80

[199] N. R. Daly. Scintillation Type Mass Spectrometer Ion Detector. *Rev. Sci. Instrum.*, **31**, 264 (1960). doi:10.1063/1.1716953. → pages 76

[200] J. Savory. *High-precision mass measurement of $N \approx Z \approx 34$ nuclides for rp-process simulations and developments for the LEBIT facility*. Ph.D. thesis, Michigan State University (2009). → pages 76

[201] M. Brodeur, T. Brunner, C. Champagne, S. Ettenauer, M. Smith, *et al.*. New mass measurement of $^6$Li and ppb-level systematic studies of the Penning trap mass spectrometer TITAN. *Phys. Rev. C*, **80**, 044318 (2009). doi:10.1103/PhysRevC.80.044318. → pages 78, 82

[202] G. Bollen, R. B. Moore, G. Savard, and H. Stolzenberg. The accuracy of heavy-ion mass measurements using time of flight-ion cyclotron resonance in a Penning trap. *J. Appl. Phys.*, **68**, 4355 (1990). doi:10.1063/1.346185. → pages 79

[203] G. Gabrielse. The true cyclotron frequency for particles and ions in a Penning trap. *International Journal of Mass Spectrometry*, **279**, 107–112 (2009). doi:10.1016/j.ijms.2008.10.015. → pages 79, 80

[204] A. Kellerbauer, K. Blaum, G. Bollen, F. Herfurth, H. J. Kluge, *et al.*. From direct to absolute mass measurements: A study of the accuracy of ISOLTRAP. *The European Physical Journal D - Atomic, Molecular and Optical Physics*, **22**, 53–64 (2003). doi:10.1140/epjd/e2002-00222-0. → pages 80, 87

[205] ISAC yields database. http://mis.triumf.ca/science/planning/yield/beam. → pages 83

[206] A. H. Wapstra, G. Audi, and C. Thibault. The AME2003 atomic mass evaluation . (I). Evaluation of input data, adjustment procedures. *Nuclear Physics*, **729**, 129–336 (2003). doi:10.1016/j.nuclphysa.2003.11.002. → pages 84, 85, 86

[207] W. Mayer, K. E. Rehm, H. J. Körner, W. Mayer, E. Müller, *et al.*. Spectroscopy of neutron-rich nuclei produced in $^{14}$C induced reactions on $^{48}$Ca. *Phys. Rev. C*, **22**, 2449–2453 (1980). doi:10.1103/PhysRevC.22.2449. → pages 84

[208] W. Benenson, K. Beard, C. Bloch, B. Sherrill, B. A. Brown, *et al.*. The masses of $^{51}$Ca and $^{47}$Ar. *Physics Letters B*, **162**, 87–91 (1985). doi:10.1016/0370-2693(85)91066-4. → pages 84

[209] M. Brauner, D. Rychel, R. Gyufko, C. A. Wiedler, and S. T. Thornton. Mass excess of $^{51}$Ca. *Physics Letters B*, **150**, 75–78 (1985). doi:10.1016/0370-2693(85)90141-8. → pages 84

[210] W. N. Catford, L. K. Fifield, T. R. Ophel, N. A. Orr, D. C. Weisser, *et al.*. Study of $^{51}$Ca via three-neutron transfer. *Nuclear Physics A*, **489**, 347–367 (1988). doi:10.1016/0375-9474(88)90157-1. → pages 84

[211] X. L. Tu, X. G. Zhou, D. J. Vieira, J. M. Wouters, Z. Y. Zhou, *et al.*. Direct mass measurements of the neutron-rich isotopes of chlorine through iron. *Zeitschrift für Physik A Hadrons and Nuclei*, **337**, 361–366 (1990). doi:10.1007/BF01294971. → pages 84, 85

[212] H. L. Seifert, J. M. Wouters, D. J. Vieira, H. Wollnik, X. G. Zhou, *et al.*. Mass measurement of neutron-rich isotopes from $^{51}$Ca to $^{72}$Ni. *Zeitschrift für Physik A Hadrons and Nuclei*, **349**, 25–32 (1994). doi:10.1007/BF01296329. → pages 84

[213] M. Matoš. *Isochronous Mass Measurements of Short-Lived Neutron Rich Nuclides at the FRS-ESR Facilities*. Ph.D. thesis, Justus-Liebig-Universität Giessen (2004). → pages 84

[214] M. Rejmund, S. Bhattacharyya, A. Navin, W. Mittig, L. Gaudefroy, *et al.*. Shell evolution and the $N = 34$ "magic number". *Phys. Rev. C*, **76**, 021304 (2007). doi:10.1103/PhysRevC.76.021304. → pages 84

[215] F. Perrot, F. Maréchal, C. Jollet, P. Dessagne, J. C. Angélique, *et al.*. $\beta$-decay studies of neutron-rich K isotopes. *Phys. Rev. C*, **74**, 014313 (2006). doi:10.1103/PhysRevC.74.014313. → pages 84

[216] A. Huck, G. Klotz, A. Knipper, C. Miehé, C. Richard-Serre, *et al.*. Beta decay of the new isotopes$^{52}$K, $^{52}$Ca, and $^{52}$Sc; a test of the shell model far from stability. *Phys. Rev. C*, **31**, 2226 (1985). doi:10.1103/PhysRevC.31.2226. → pages 85

[217] R. Mendelson, G. J. Wozniak, A. D. Bacher, J. M. Loiseaux, and J. Cerny. Mass of $^{13}$O and the Isobaric Multiplet Mass Equation. *Phys. Rev. Lett.*, **25**, 533 (1970). doi:10.1103/PhysRevLett.25.533. → pages 87

[218] G. Trentelman, B. Preedom, and E. Kashy. Precision Mass Measurement of $^{9}$C, $^{13}$O, and $^{21}$Mg and the Isobaric-Multiplet Mass Equation. *Phys. Rev. C*, **3**, 2205–2213 (1971). doi:10.1103/PhysRevC.3.2205. → pages 87

[219] R. Robertson, S. Martin, W. R. Falk, D. Ingham, and A. Djaloeis. Highly Proton-Rich $T_z = -2$ Nuclides: $^{8}$C and $^{20}$Mg. *Phys. Rev. Lett.*, **32**, 1207 (1974). doi:10.1103/PhysRevLett.32.1207. → pages 87

[220] R. E. Tribble, J. D. Cossairt, and R. A. Kenefick. The mass of $^{20}$Mg: A test of the isobaric multiplet mass equation in $A = 20$. *Physics Letters B*, **61**, 353–355 (1976). doi:10.1016/0370-2693(76)90586-4. → pages 87

[221] C. Wrede, J. A. Clark, C. M. Deibel, T. Faestermann, R. Hertenberger, *et al.*. Toward precise $Q_{\mathrm{EC}}$ values for the superallowed $0^+ \to 0^+$ $\beta$ decays of $T = 2$ nuclides: The masses of $^{20}$Na, $^{24}$Al, $^{28}$P, and $^{32}$Cl. *Phys. Rev. C*, **81**, 055503 (2010). doi:10.1103/PhysRevC.81.055503. → pages 87, 94

[222] C. Diget, P. Adrich, D. Bazin, M. Bowen, B. Brown, *et al.*. Structure of excited states in $^{21}$Mg studied in one-neutron knockout. *Phys. Rev. C*, **77**, 064309 (2008). doi:10.1103/PhysRevC.77.064309. → pages 87, 94

[223] A. Lapierre, M. Brodeur, T. Brunner, S. Ettenauer, P. Finlay, *et al.*. Penning-trap mass measurements of the neutron-rich K and Ca isotopes: Resurgence of the $N = 28$ shell strength. *Phys. Rev. C*, **85**, 024317 (2012). doi:10.1103/PhysRevC.85.024317. → pages 87, 88, 90

[224] A. T. Gallant, J. C. Bale, T. Brunner, U. Chowdhury, S. Ettenauer, *et al.*. New precision mass measurements of neutron-rich calcium and potassium isotopes and three-nucleon forces. *Phys. Rev. Lett.*, **109**, 032506 (2012). doi:10.1103/PhysRevLett.109.032506. → pages 91

[225] A. G. Taube and R. J. Bartlett. Improving upon CCSD(T): ΛCCSD(T). I. Potential energy surfaces. *J. Chem. Phys.*, **128**, 044110 (2008). doi:10.1063/1.2830236. → pages 91

[226] R. B. Firestone. Nuclear Data Sheets for A = 21. *Nuclear Data Sheets*, **103**, 269–324 (2004). doi:10.1016/j.nds.2004.11.003. → pages 93, 94

[227] J. P. Wallace, P. J. Woods, G. Lotay, A. Alharbi, A. Banu, *et al.*. $\beta$-Delayed proton-decay study of $^{20}$Mg and its implications for the $^{19}$Ne$(p,\gamma)^{20}$Na breakout reaction in X-ray bursts. *Physics Letters B*, **712**, 59–62 (2012). doi:10.1016/j.physletb.2012.04.046. → pages 94

[228] W. E. Ormand and B. A. Brown. Empirical isospin-nonconserving hamiltonians for shell-model calculations. *Nuclear Physics A*, **491**, 1–23 (1989). doi:10.1016/0375-9474(89)90203-0. → pages 95

[229] J. M. K. Hebeler, J. D. Holt and A. Schwenk. Nuclear forces and their impact on neutron-rich nuclei and neutron-rich matter. To be published (2015). → pages 98

[230] L. Chen, T. C. L. Wang, T. L. Ricca, and A. G. Marshall. Phase-modulated stored waveform inverse Fourier transform excitation for trapped ion mass spectrometry. *Analytical chemistry*, **59**, 449–454 (1987). → pages 123

# Appendix A

# Contributions to TITAN

## A.1 Axial Frequency Measurements

Penning trap experiments that use the TOF-ICR or PI-ICR detection methods do not rely on detecting the pick-up signals of an ion's motion on the trap electrodes. Instead, the radial frequencies are determined either by extracting the ion through the magnetic field gradient of the superconducting solenoid magnet, and measuring the change in time-of-flight (section 3.3.4), or by projecting the motion of the ion on to a position sensitive detector and measuring the phase accumulation of the ion [179]. Both of these methods only allow for the detection of the radial motion of an ion.

In section 3.3.4.6 I describe a new method to measure the axial frequency of an ion in a Penning trap using destructive detection methods.

## A.2 Arbitrary function generator programming

To perform a cyclotron frequency measurement a list of desired frequencies must be given to an Arbitrary/Function Generator (AFG). Previously at TITAN this was accomplished through the use of two AFGs, the first called the "frequency generator", which supplied the radio-frequency for the ion excitation, and the second called the "ladder". The "ladder" generator was programmed with a staircase waveform, with the number of steps corresponding to the number of frequencies to be applied when generating a resonance. The "frequency" generator was programmed to be frequency modulated about a user supplied centre frequency $\nu_{\text{cent}}$ and a modulation depth of $\pm\nu_{\text{mod}}$. The output of the "ladder" was sent to the modulation input of the "frequency" generator, thus generating a series of frequencies from $\nu_{\text{cent}} - \nu_{\text{mod}}$ to $\nu_{\text{cent}} + \nu_{\text{mod}}$.

Several drawbacks of this technique are:

- Output voltage noise from the "ladder" generator will cause jitter of the "frequency" generator's output frequency
- To ease the understanding the total system cycle, each step in the "ladder" waveform was generally set to a convenient length (20 ms, 50 ms, 100 ms, etc.), limiting the range of dipole and quadrupole excitation times
- Drifts in the calibration constants of the "ladder" output digital-to-analog converter could cause systematic shifts in the absolute output frequency of the "frequency" generator

To overcome these problems, a model 33521A AFG from Agilent (now Keysight) was purchased to apply the quadrupole field, while a model 33500B AFG with expanded memory from Agilent was purchased for dipole cleaning and stored waveform inverse Fourier transform (SWIFT) cleaning [230]. Both AFG models have a "list" mode, where a list of frequencies can be programmed to the AFG. The AFG can then be externally triggered to step through the list, not only eliminating the need for the "ladder" generator, but also eliminating potential jitter and offset issues arising from the digital-to-analog converter of the "ladder" generator. A potential systematic from the use of the "ladder" generator was discovered during a measurement of the $^{51}$Cr $Q$-value [173] (affected data was not included in [173]), where it was found that the output of the "ladder" generator caused the frequency modulation range to be smaller than desired. This did not affect resonance data where the central portion of the resonance lineshape was near the centre of the scan range, instead, only affecting data near the edges of the scan range. By using the "list" mode of the 33521A AFG, systematics from the frequency modulation range are eliminated. The 33521A AFG also expands the capabilities of the TITAN system, as there is no need for a "ladder" generator, meaning that an arbitrary series of frequencies can be programmed into the AFG, and can be applied for any length of time, eliminating the cycle-length dependence on the "ladder" waveform.

One potential application of the new frequency generation system is the measurement of co-trapped ions. As an example, suppose that two ion species are delivered to MPET simultaneously, each with cyclotron frequencies of $\nu_{1,2}$. The dipole AFG can be programmed such that for the first half of the measurement ion2 is dipole cleaned, while the quadrupole AFG steps through the frequencies required to generate a resonance of ion1. During the second half of the measurement, the dipole AFG will then dipole clean ion1, while the quadrupole AFG steps through the frequencies required to generate a resonance of ion2. In this way, the resonance of each ion are generated at the same time. This is useful if one of the ions has a well known mass and can serve as a reference to calibrate the magnetic field. Any systematics arising from magnetic field drifts are removed since measurements are built in such a way that

each ion will see the same drifts, assuming the magnetic field drifts are slow (i.e. if magnetic field fluctuations occur on time scales longer than several minutes or longer).

The code to program the AFGs is hosted at http://github.com/aarongallant/Afgcontrol.

## A.3 SortEVA

SortEVA is a program written to streamline the analysis of large numbers of resonance files, particularly when optimizing the trapping voltages in MPET. The general method used at TITAN to optimize the trapping electrodes can be found in [155]. The optimizing procedure generates a large quantity of data, all of which must be fit individually in order to ensure the quality of the data, and due to limitations of the existing fitting program. To overcome these limitations, SortEVA (figure A.1) was written to organize the files generated from the data acquisition system, and to perform fits to each of the files. The resulting fits are then stored in memory, allowing the user to examine the quality of each fit, ensuring both that the data in the file is "good", and that the fit is correct.

An earlier version of this program played a key role in determining the systematic errors during the first uses of on-line, highly-charged ions in the following publications [147, 174, 144].

## A.4 Correlations between adjacent frequency ratios

To eliminate systematics effects, as described in section 3.3.7, the ratio of frequencies is taken between the ion of interest and a well known calibrant, or reference, ion (section 3.3.6). Generally, the sequence of measurements is as follows: reference, ion of interest, reference, ion of interest, reference, etc. This pattern of measurements can be seen in figure A.2. The reference frequency is interpolated to the time of the measurement of the ion of interest, thus leading to correlations between the frequency ratios $R_i$ and $R_{i+1}$, as both ratios depend on a shared reference measurement. It may also be the case that two or more measurements of the ion of interest are between the same set of reference measurements. Here we will derive the covariance between frequency measurements that share reference measurements. This work was derived independently by Stephan Ettenauer [197], and was published in [174].

The frequency between any two references can be interpolated as

$$\nu(T) = \frac{\nu_{j+1} - \nu_j}{t_{j+1} - t_j}\left(T - t_j\right) + \nu_j \tag{A.1}$$

where $T$ is a time between the reference measurements at times $t_i$ and $t_{i+1}$. The covariance

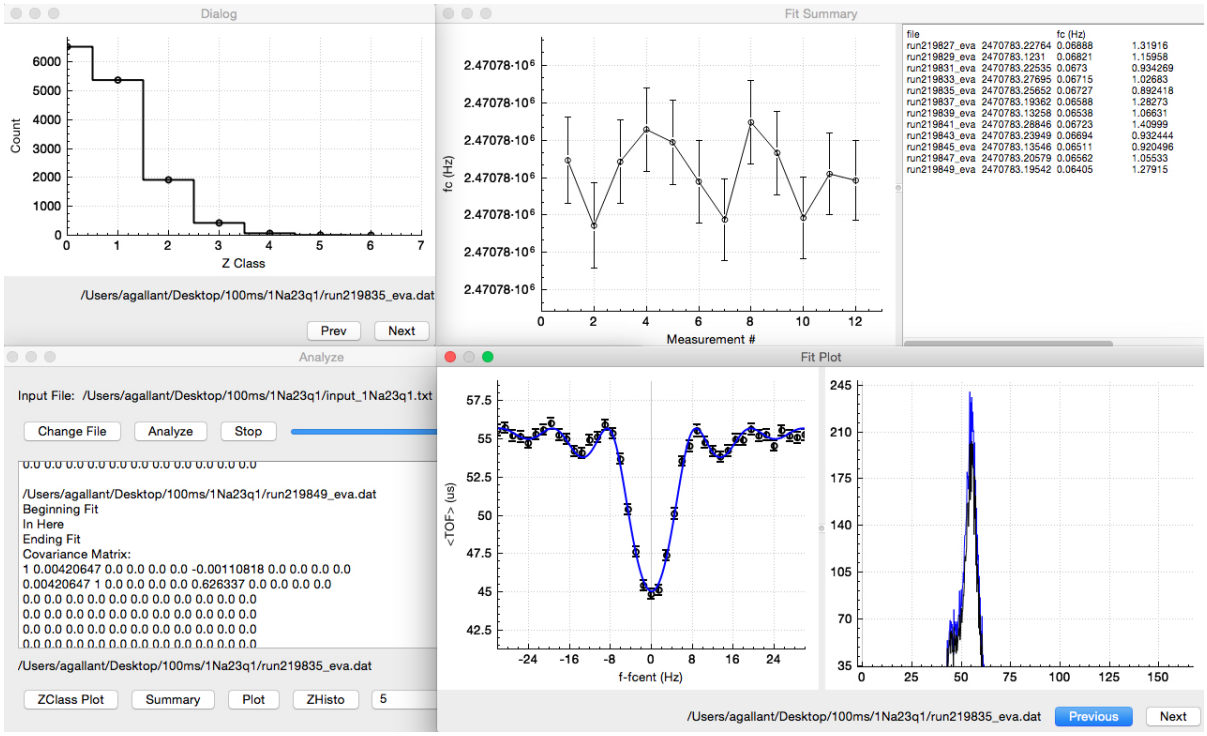


**Figure A.1:** Screen capture of SortEVA analysing a data set. Clockwise from upper left: Z-class histogram (number of detected ions after extracting from the trap), plot of fitted frequencies against the measurement number along with a running list of the fit results (filename, frequency, frequency uncertainty, reduced $\chi^2$), resonance and fit along with TOF histogram, and the main fit dialog for monitoring the program's progress.

between two frequency measurements that share one reference measurement (for example, the correlation between the frequency $\nu(T_{i+2})$ and $\nu(T_{i+3})$ in figure A.2) is

$$\begin{aligned}\operatorname{cov}\left(\nu(T_i),\nu(T_{i+1})\right) &= \left(\frac{\partial\nu(T_i)}{\partial\nu_{i+1}}\right)\left(\frac{\partial\nu(T_i)}{\partial\nu_{i+1}}\right)\operatorname{cov}\left(\nu_{i+1},\nu_{i+1}\right)\\ &= \left(\frac{T_i-t_j}{t_{j+1}-t_j}\right)\left(\frac{t_{j+2}-T_{i+1}}{t_{j+2}-t_{j+1}}\right)\sigma^2_{j+1}\end{aligned} \tag{A.2}$$

where $\sigma_{j+1}$ is the uncertainty of the $(j+1)$th reference measurement. If we define the frequency ratio to be $R=\nu_{ref}/\nu$, the covariance between the frequency ratios is then

$$\operatorname{cov}\left(R_i,R_{i+1}\right) = \frac{1}{\nu_i\nu_{i+1}}\operatorname{cov}\left(\nu(T_i),\nu(T_{i+1})\right). \tag{A.3}$$

where $\nu_i$ is the $i$th frequency measurement of the ion of interest.

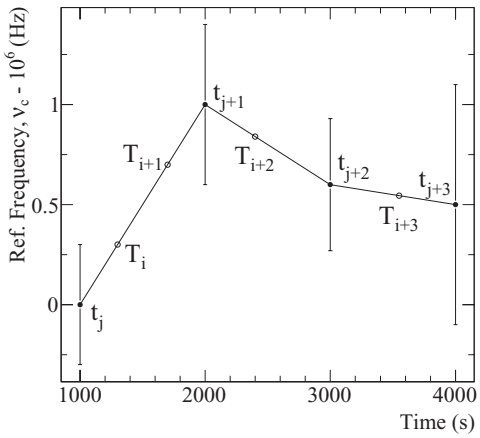


**Figure A.2:** Illustration of the correlation introduced between adjacent frequency ratio measurements from shared references. The solid circles ($t_j$'s) represent reference measurements of $\nu_{c,ref}$ and the open circles ($T_i$'s) show the interpolation of $\nu_{c,ref}$ to the centre time of a measurement of an ion of interest. From the figure it is clear that $T_i$ is correlated with $T_{i+1}$, $T_i$ and $T_{i+1}$ with $T_{i+2}$, and $T_{i+2}$ with $T_{i+3}$. Figure reproduced from [174].

The covariance between measurements that share both reference measurements (for example points $T_i$ and $T_{i+1}$ in figure A.2) can be found in a similar manner. The covariance is

$$\mathrm{cov}\left(R_i, R_{i+1}\right) = \frac{1}{\nu_i \nu_{i+1}} \left[ \left( \frac{t_{j+1} - T_i}{t_{j+1} - t_j} \right) \left( \frac{t_{j+1} - T_{i+1}}{t_{j+1} - t_j} \right) \sigma_j^2 + \left( \frac{T_i - t_j}{t_{j+1} - t_j} \right) \left( \frac{T_{i+1} - t_j}{t_{j+1} - t_j} \right) \sigma_{j+1}^2 \right]. \tag{A.4}$$

The weighted average and uncertainty can then be calculated from

$$\bar{R} = \frac{\sum_{i,j} \left(V^{-1}\right)_{ij} R_j}{\sum_{i,j} \left(V^{-1}\right)_{ij}} \tag{A.5}$$

with an accompanying uncertainty of

$$\sigma_{\bar{R}}^2 = \frac{1}{\sum_{i,j} \left(V^{-1}\right)_{ij}}. \tag{A.6}$$